Beyond Equilibrium Assemblies:

Applying Light, Flow, and Confinement

by

Youngri Kim

A dissertation submitted in partial fulfillment
of the requirements for the degree of
Doctor of Philosophy
(Chemical Engineering)
in The University of Michigan
2016

Doctoral Committee:

Professor Michael J. Solomon, Chair
Professor Ronald G. Larson
Associate Professor Kevin P. Pipe
Assistant Professor Timothy F. Scott

Dedication

To my mother, an incredibly strong woman, who has done so much for me.

Acknowledgements

I am grateful for the opportunity to express my appreciation to the people, who have been such a big part of my life.

First, I would like to thank my advisor, Professor Mike Solomon. I don't think I could have found a better advisor for my doctorate. Even through the low points of my time in graduate school, his encouragement, motivation, and kindness kept me going. I also want to thank my committee, Professors Ron Larson, Tim Scott, and Kevin Pipe, for their thoughtful guidance and advice on my research.

I feel so fortunate that I was able to share my time at Michigan with great friends. I especially want to thank Allison Franck, Brittany Farrell, and Laura Chang. I am also grateful to my Michigan family, the Solomon Group, for teaching me so much and being so supportive and close throughout my time here. Thank you Elizabeth Stewart, Aayush Shah, Mahesh Ganesan, Laura Colón-Meléndez, Megan Szakasits, Onajite Shemi, and Joseph Ferrar for being awesome lab mates, as well as friends.

I am also so lucky to have met Jimmy Tran, during the hardest times for me in graduate school. Even from miles away, he has been loving, supportive, and patient with me. I am so thankful for you and excited to be with you now.

Lastly, I want to try to put into words how grateful I am of my family. I have been apart from them for so many years but I always knew that they were there for me.

My mom is such an incredible person, who have selflessly provided for my sister and I by herself. I don't know if there's any way to repay all the debt but I will try my best to become someone that she now can depend upon. I also want to thank my sister and my brother-in-law for being so supportive. I feel so lucky to have both of you in my life. Also, thank you for bringing the cutest nephew into this world!

Table of Contents

List of Figures

List of Appendices

Abstract

In this dissertation, we report the flow and microstructural behavior of colloidal dispersions and surfactant assemblies (wormlike micelles) away from bulk equilibrium conditions. Bulk, equilibrium methods for self-assembly of soft matter are limited by slow times scales and large material requirements, and are not applicable to the dynamic conditions under which these complex fluids are processed in industry. By introducing light, flow, and confinement, we find a novel, fast mechanism for directed assembly of colloidal crystals, a regime of near-wall velocity fluctuations of wormlike micelle (WLM) solutions relevant to certain unsteady industry flows, such as bottle filling, and an efficient method for generating droplets with intrinsic mechanical properties from their internal colloidal gel structures.

A directed assembly method is reported that uses light to generate three-dimensional colloidal crystals. The crystalline structures produced are simultaneously reconfigurable in space and time. Simple illumination of a glass substrate coated with indium tin oxide (ITO) generates accumulation and assembly of colloids. The three-dimensional structures obtained by the method are ~ 5 layers thick and extends ~ 10 μm from the ITO coated substrate. The kinetics of the assembly depends on the initial volume fraction of colloids and the light intensity. The mechanism for assembly is electrophoretic in origin; light catalyzes reactions at the ITO coated surface that drives

ion flows within the solvent. This ionic flow sets up a current that establishes an electric field, which induces electrophoretic motion of the colloids. We apply this light-induced electrophoretic method to generate complex shapes of colloidal crystalline assemblies through simple optical manipulation.

In the second part of the dissertation, we measure the transient flow behavior of WLM solutions in channel flow. Channel flow serves as a good model of industrial conduit flows and is simple to generate. Using confocal microscopy and particle image velocimetry techniques, we observe steady-state deviations from a parabolic flow profile that leads to the development of a thin, near-wall band with high shear rates and velocities. The applied shear rates at which these deviations occur correspond well with the measured rheology, which is characteristic of shear banding fluids. The near-wall bands display dynamics along the vorticity (neutral) axis; dynamics are observed at gradient distances up to 10 μm from the wall. By means of space-time plots generated for the flow at the smallest near-wall position (2 μm), we observe four distinct stages of velocity variations in the vorticity direction over time. We compare the results of this work in context with steady-state vorticity structuring that has been reported in planar Poiseuille flows.

Lastly, colloidal gel assemblies are produced within micron-scale droplets as an efficient method to introduce intrinsic mechanical properties to droplet-based materials. Within the oil-in-water droplets studied, colloidal crystalline phases are first observed. Crystalline assemblies are formed by ion migration from the dispersed oil phase to the aqueous phase, which triggers crystallization by increasing the Debye screening length of the particles in solution. A transition to a colloidal gel is found at longer times (~ 2

weeks) for these charged PMMA colloids. The gelation kinetics is dependent upon the droplet size and the accessibility of the droplet interface to the outer aqueous phase. From the observations, we hypothesize that colloidal gel formation is promoted within droplets through, confinement-induced particle attractions.

Chapter 1 Introduction

Self-assembled systems are prevalent in both nature and technology, ranging from small-scale structures, such as proteins or colloidal crystals, to large-scale swarms of ants or schools of fish[1]. Self-assembly is a spontaneous organization of the constituents, such as atoms, molecules, or colloids, into complex structures without any external influences[1]. Interests in these structures stem from the desire to understand nature, as well as, to mimic their design for technological applications. For example, bright colors found in nature in butterfly wings or opals has inspired a large body of work focused on engineering photonic crystals of colloids[2–4]. In addition, diverse self-assembled structures are utilized in consumer products, microelectronics, sensors, and micro robotics, etc[5]. This dissertation is focused on the assemblies of two different kinds of soft matter: colloids and surfactant molecules. For these systems, we probe their assembly behaviors away from bulk equilibrium conditions, by introducing directed optical fields, flow, and confinement.

1.1 Colloidal suspensions and equilibrium assemblies

Colloids, particles of the size ranging from a few nanometers to micrometers[6], are primarily known for their applications in food, paints, consumer products industries and their prevalence in natural systems. However, they also serve as larger scale counterparts

to atoms. They are constituents and building blocks of suspensions, gels, glasses, crystals and many more intricate structures[7]. Due to their micrometer size, colloidal interactions can be visualized with a microscope. Thus, colloids are studied extensively as a model system for understanding atomic interactions[8]. In addition to analogously investigating the governing forces of particle interactions, they are essential in the study of phase transitions of liquids. Colloidal phase transitions—encompassing fluid, crystalline, and glass phases—are comparable to molecular liquid transitions.

Pusey et al. first demonstrated the phase behavior of colloidal fluids in equilibrium[9]. They studied the model colloidal system with short-ranged repulsive interactions: sterically-stabilized poly(methylmethacrylate) (PMMA) particle dispersion in a refractive index matched solvent. The steric stabilization layer and the refractive index matching led to almost hard-sphere-like behaviors due to the repulsive potentials at the particles surface and the minimization of the van der Waals attractions of the particles, respectively[8]. For the assembly of these colloids, free particle suspensions were formed at varying concentrations of colloids and monitored for changes in their iridescence or light-scattering patterns[10]. A progression of phases from fluid to fluid and crystal coexistence to crystal, and amorphous glass was observed with increase in initial particle concentrations. Particle volume fraction of 0.494 was found to be the freezing concentration, where it shifts from equilibrium fluid phase into the fluid-crystal coexistence phase. Above the volume fraction of 0.545, which denotes its melting concentration, the equilibrium state was found to be crystalline. When prepared above its 0.58 volume fraction, the suspension became trapped in an amorphous glass phase[9]. While this method provides beautifully colored products, the equilibrium self-assembly

process is slow, taking up to few days to weeks, and has a large material requirement (volume fraction of 0.545 for crystals).

1.2 Directed assemblies

The traditional approach for investigating phase transitions through equilibrium self-assemblies is highly restrictive. Recently, growing emphasis is put on utilizing colloidal systems as building blocks to create dynamic assemblies. In addition, highly reconfigurable assemblies are created by designing complex colloidal materials, such as shape-changing colloids[11], Janus particles[12], and lock and key particles[13], or by employing unique external fields[14].

1.2.1 Colloidal crystals from directed assemblies

In Chapters 2 and 4, we demonstrate assemblies of colloidal crystals. Colloidal crystals are long-range ordered arrays of particles that can be used to create photonic crystals[15]. Colloidal crystals prepared from sub-micrometer scale particles are good candidates for the production of photonic crystals because they diffract light of wavelengths in the visible or near-IR range[15]. Also, they are developed for use in chemical sensors by prompting the change in color of the material in the presence of a specific chemical[16]. When the material is in contact with the chemical, Holtz's colloidal crystal undergoes structural changes that increase the separation between spheres, which shifts its Bragg peak into longer wavelengths[16]. This capability to tune the structural color of the material is characteristic of colloidal crystals that diffract light at wavelengths determined by their lattice spacing.

To this date, most colloidal crystals have been commonly prepared in bulk through the following methods: sedimentation[17,18], concentrated of equilibrium suspensions[9,10], lithography[19], and convective assembly[20,21]. However, most of these methods for colloidal crystal production are static: they lead to crystallization, but the crystal structure is then permanent[11]. More reversible crystalline assemblies can be achieved in solution by applying electric fields (electrophoresis and dielectrophoresis)[22–25], light [25,26] or gradients in temperature (thermophoresis)[27–29].

1.3 Light-induced assemblies

In Chapter 2, we are specifically interested in light as our assembly control variable because it can provide us with applications in camouflage materials. The response of a structural color changing material to light can be used to develop a mimic of nature's camouflaging species, such as cephalopods [30]. In addition to technological applications, light-controlled assemblies are attractive because they are non-invasive and can be delivered rapidly to a precise region of interest[31]. Light-induced crystallinity has been achieved by utilizing several different mechanisms: photoisomerization of molecules[31], photo-induced conformational changes in molecular structures[32], and photon-directed colloidal crystallization under applied electric fields[26]. Photo-induced conformational changes of naphthopyran molecules led to a liquid-crystal phase transitions on a molecular level[31]. Nanoparticles covered with photoactive ligands were found to self-assemble into suprastructures as molecules toggled between cis and trans conformations under UV light[32].

On a colloidal scale, Gong et al. and Hayward et al. have discovered that crystalline assembly was driven by UV radiation[25,26]. However, this required the system to be under applied electric fields[25,26]. Therefore, we report a purely optical process for colloidal crystallization in Chapter 2.

1.4 Confinement-induced assemblies

Bulk equilibrium assemblies, along with long time scales, are restricted by prevalent defects, low yields and low reproducibility[5]. In Chapter 4, we use a small-scale assembly method in the form of droplet confinement to induce assemblies of colloidal crystals and gels. Confinement in droplets provides compartmentalization of the contained species and, therefore, serves as a perfect vessel for studying isolated self-assembly behavior[33]. Microfluidic devices can be used to manufacture highly stable droplets at high production rates[34]. Typical sizes of droplets range from 1 to 200 μm in diameter and the desired length scales can be attained through the manipulation of the microfluidic flow properties, such as fluid viscosities and flow rates of the fluids[35]. The small scales of these droplets reduce the material requirement for studying self-assembly behaviors of colloids. A droplet of diameter ~ 200 μm would fit ~ 2 million micron sized colloid at close packing, whereas 100 μl bulk assembly at close packing would need ~ 50 billion colloids.

1.4.1 Assemblies in confinement

Currently, colloidal assemblies within droplets have been induced by polymerization[36], interfacial instability[37–40], interfacial adsorption[41,42], evaporation[43], and

boundary dynamics reduction[44]. These methods resulted in assembly structures ranging from colloidal crystals, to crystalline to shells, and to amorphous glasses.

Colloidal crystals, confined to a droplet, form dense packings of colloids in the shape of a sphere. These supraparticles or photonic balls possess diffraction properties based on the colloidal volume fraction and size[40]. Interfacial permeability[38,40,45] and evaporation[46] methods have been used to produce these crystalline assemblies of colloids. Recently, increased control over the photonic structures was provided by the work by Kim et al. The dynamic control of the osmotic pressure gradients resulted in the control of the diffracted color of the photonic droplets[39].

Other crystalline structures, including clusters with icosahedral and rhombicosidodecahedral order, were formed through spherical confinement and subsequent evaporation of the dispersed solvent[43]. Structures with similar symmetries have not been obtained in bulk due to incompatibility with long-range order and are unique to confinement of about 25,000 to 90,000 colloids.

In addition to crystalline structures, disordered, glassy structures of colloids were also reported for colloidal suspensions confined in emulsion droplets. With increased boundary contact of the colloidal suspensions in droplets, colloidal mobility was sensitively influenced by the viscosities of the external fluid[44]. Increase in external fluid viscosity resulted in lowered particle mobility at both the interface and the bulk, leading to the formation of a glassy state.

To date, assemblies confined in droplets have been focused on crystalline and glassy structures. However, colloidal gels are also an important class of colloidal matter that is widely applicable to food, consumer products, membranes, ceramics, and

biomaterials, such as tissue scaffolds[47]. Colloidal gel assemblies are excellent candidates for generating solid-like mechanical properties, such as a yield stress[48]. Therefore, for practical applications of the droplets, an efficient method to introduce colloidal gel assemblies to the droplet is important. In Chapter 4, we therefore demonstrate the assembly of colloidal gels in a single droplet emulsion system. We further extend the process to assemblies of anisotropic colloids.

1.4.2 Anisotropic colloids

Ellipsoidal particles appear in pharmaceutical, biomedical and chemical processing industries and have been attractive in product formulations because they are able to mimic material properties of sphere systems at lower volume fractions[49]. These lower volume fraction requirements for ellipsoidal assemblies make these systems more economically advantageous for commercial applications[50].

Within confinement, rod-like colloids showed positional and orientational order based on the slit width of the micro-wedge[51]. Plastic crystal-to-crystal transition occurred for the confinement induced structures due to electrostatic repulsion of the rod-like colloids with the slit walls and the neighboring colloids. In droplet confinement environments, similar polymeric rod-like particles migrated to the droplet interface and adsorbed to form particle-stabilized, Pickering emulsions[52,53]. In Chapter 4, we study the assembly behavior of polymeric ellipsoids confined in oil-in-water droplets within the confined droplets.

1.5 Wormlike micelles: assemblies of surfactants

Wormlike micelles are long, entangled self-assemblies of surfactant molecules[54]. The surfactant molecules assemble into long, wormlike structures, instead of spherical micelles, with the addition of salt; salt acts to screen out the charges on the surfactant head group, reducing the head/tail size ratio of the surfactants[55]. The shift in this geometrical quantity leads to a higher stability of cylindrical local packing. With an increase in surfactant concentrations, the length of these cylindrical micelles increases to form elongated wormlike micelles. Further increase in salt concentrations result in a transition from entangled to branched networks of wormlike micelle solutions[56].

Wormlike micelles are referred to as "living" polymers due to their similarity to the entangled, flexible structures and reptation behavior of polymers, but with the exception of their ability to break and reform[57]. The stress relaxation mechanism through the combination of reptation and reversible scission results in linear viscoelasticity described by a single-mode Maxwell mode[55].

1.6 Wormlike micelles in flow

Under large deformations, the equilibrium assembly structures of wormlike micelles undergo shear banding, a separation of the flow into bands of distinct internal microstructures and viscosities[58]. The shear banding phenomenon originates from the non-monotonicity of the flow curve, which quantifies the dependence of steady stress on shear rate[58]. Within the zero or negative slope region of the flow curve, homogeneous flow becomes unstable, breaking into coexisting bands of differing shear rates along the gradient axis[59]. In addition to gradient shear banding, the nonlinear viscoelastic response

of wormlike micelles generates other flow instabilities, such as vorticity banding[60,61], apparent wall slip[62–64], interfacial instability between shear bands at steady state[65–67] and oscillating, chaotic bands[68,69].

Gradient shear banding has been attributed to the separation of two regions of distinct mesoscopic structures[70], based on micellar alignment[71] or concentration differences between the bands[55]. These shear bands also have shown to accompany fluctuations along the vorticity at the shear band interfaces[65,66,72,73] or within the high shear rate band[74]. The vorticity fluctuations have been correlated to normal stress differences across the bands[60,61], fluctuating slip that causes instability in the high shear rate band[74], or viscoelastic instability in the high shear rate band[75].

In the past decade, both transient and steady-state studies of shear banding and vorticity fluctuations have been carried out for wormlike micelle solutions in Taylor-Couette geometries. However, the transient measurements are lacking in rectangular channel flows. In Chapter 3, we show transient near-wall dynamics of wormlike micelle flows in planar channel geometry under shear banding conditions.

1.7 Organization of the dissertation

In this thesis, we study two distinct scales of assemblies, colloids and surfactant molecules, and their behavior under exposure to light, flow, or confinement.

In Chapter 2, we demonstrate a novel light-induced method to form reconfigurable colloidal crystals. The kinetics and the 3D structures of the assembly are characterized and the underlying mechanism is found to be light-induced current driven electrophoretic assembly.

In Chapter 3, we report the behavior of self-assembled wormlike micelles under planar channel flows. Confocal microscopy and particle image velocimetry tools are used to analyze the steady state velocity profiles of the flow and to characterize the spatiotemporal fluctuations at near-wall regions for shear-banded flows.

In Chapter 4, we induce colloidal gelation within oil-in-water droplet confinement. Transition from colloidal crystals to gels is observed over time. The kinetics of gelation is found to depend on droplet size, droplet interfacial accessibility to the outer solution, and the stability of the particles. We further extend the method to anisotropic colloidal systems. The elastic moduli of the droplets are measured using atomic force microscopy.

Finally, we conclude with a summary of the work and future directions that can be taken based on the results of this thesis.

1.8 References

1. Whitesides, G. M. & Grzybowski, B. Self-assembly at all scales. *Science* **295,** 2418–21 (2002).

2. Dziomkina, N. V. & Vancso, G. J. Colloidal crystal assembly on topologically patterned templates. *Soft Matter* **1,** 265 (2005).

3. Kim, H. *et al.* Structural colour printing using a magnetically tunable and lithographically fixable photonic crystal. *Nat. Photonics* **3,** 534–540 (2009).

4. Fudouzi, H. & Xia, Y. Colloidal Crystals with Tunable Colors and Their Use as Photonic Papers. *Langmuir* **19,** 9653–9660 (2003).

5. Velev, O. D. & Gupta, S. Materials Fabricated by Micro- and Nanoparticle Assembly - The Challenging Path from Science to Engineering. *Adv. Mater.* **21,** 1897–1905 (2009).

6. Russel, W. B., Saville, D. A. & Schowalter, W. R. *Colloidal Dispersions*. (Cambridge University Press, 1992).

7. Glotzer, S. C. & Solomon, M. J. Anisotropy of building blocks and their assembly into complex structures. *Nat. Mater.* **6,** 557–62 (2007).

8. Yethiraj, A. & van Blaaderen, A. A colloidal model system with an interaction tunable from hard sphere to soft and dipolar. *Nature* **421,** 513–7 (2003).

9. Pusey, P. N. & van Megen, W. Phase behaviour of concentrated suspensions of nearly hard colloidal spheres. *Nature* **320,** 340–342 (1986).

10. Pusey, P. N. *et al.* Structure of crystals of hard colloidal spheres. *Phys. Rev. Lett.* **63,** 2753–2756 (1989).

11. Nguyen, T. D., Jankowski, E. & Glotzer, S. C. Self-assembly and reconfigurability of shape-shifting particles. *ACS Nano* **5,** 8892–903 (2011).

12. Hong, L., Jiang, S. & Granick, S. Simple method to produce Janus colloidal particles in large quantity. *Langmuir* **22,** 9495–9 (2006).

13. Sacanna, S., Irvine, W. T. M., Chaikin, P. M. & Pine, D. J. Lock and key colloids. *Nature* **464,** 575–8 (2010).

14. Solomon, M. J. Materials science: Reconfigurable colloids. *Nature* **464,** 496–8 (2010).

15. Colvin, V. L. From Opals to Optics: Colloidal Photonic Crystals. *MRS Bull.* **26,** 637–641 (2001).

16. Holtz, J. H. & Asher, S. A. Polymerized colloidal crystal hydrogel films as intelligent chemical sensing materials. *Nature* **389,** 829–32 (1997).

17. Murai, M., Okuzono, T., Yamamoto, M., Toyotama, A. & Yamanaka, J. Gravitational compression dynamics of charged colloidal crystals. *J. Colloid Interface Sci.* **370,** 39–45 (2012).

18. Hoogenboom, J. P., Derks, D., Vergeer, P. & van Blaaderen, A. Stacking faults in colloidal crystals grown by sedimentation. *J. Chem. Phys.* **117,** 11320 (2002).

19. Campbell, M., Sharp, D., Harrison, M., Denning, R. & Turberfield, A. Fabrication of photonic crystals for the visible spectrum by holographic lithography. *Nature* **404,** 53–6 (2000).

20. Jiang, P., Bertone, J. F., Hwang, K. S. & Colvin, V. L. Single-Crystal Colloidal Multilayers of Controlled Thickness. *Chem. Mater.* **11,** 2132–2140 (1999).

21. Dimitrov, A. S. & Nagayama, K. Continuous Convective Assembling of Fine Particles into Two-Dimensional Arrays on Solid Surfaces. *Langmuir* **12,** 1303–1311 (1996).

22. Trau, M., Saville, D. A. & Aksay, I. A. Field-Induced Layering of Colloidal Crystals. *Science (80-.).* **272,** 706–709 (1996).

23. Giersig, M. & Mulvaney, P. Preparation of ordered colloid monolayers by electrophoretic deposition. *Langmuir* **9,** 3408–3413 (1993).

24. Richetti, P., Prost, J. & Barois, P. Two-dimensional aggregation and crystallization of a colloidal suspension of latex spheres. *J. Phys. Lettres* **45,** 1137–1143 (1984).

25. Hayward, R., Saville, D. & Aksay, I. Electrophoretic assembly of colloidal crystals with optically tunable micropatterns. *Nature* **404,** 56–9 (2000).

26. Gong, T. & Marr, D. W. M. Photon-directed colloidal crystallization. *Appl. Phys. Lett.* **85,** 3760 (2004).

27. Deng, H.-D. *et al.* Assembling of three-dimensional crystals by optical depletion force induced by a single focused laser beam. *Opt. Express* **20,** 9616–23 (2012).

28. Di Leonardo, R., Ianni, F. & Ruocco, G. Colloidal attraction induced by a temperature gradient. *Langmuir* **25,** 4247–50 (2009).

29. Duhr, S. & Braun, D. Two-dimensional colloidal crystals formed by thermophoresis and convection. *Appl. Phys. Lett.* **86,** 131921 (2005).

30. Mäthger, L. M., Denton, E. J., Marshall, N. J. & Hanlon, R. T. Mechanisms and behavioural functions of structural coloration in cephalopods. *J. R. Soc. Interface* **6 Suppl 2,** S149–63 (2009).

31. Klajn, R., Bishop, K. J. M. & Grzybowski, B. A. Light-controlled self-assembly of reversible and irreversible nanoparticle suprastructures. *Proc. Natl. Acad. Sci. U. S. A.* **104,** 10305–9 (2007).

32. Kosa, T. *et al.* Light-induced liquid crystallinity. *Nature* **485,** 347–9 (2012).

33. Theberge, A. B. *et al.* Microdroplets in microfluidics: an evolving platform for discoveries in chemistry and biology. *Angew. Chem. Int. Ed. Engl.* **49,** 5846–68 (2010).

34. Wang, W. *et al.* Controllable microfluidic production of multicomponent multiple emulsions. *Lab Chip* **11,** 1587–92 (2011).

35. Utada, A. S. *et al.* Dripping, Jetting, Drops, and Wetting: The Magic of Microfluidics. *MRS Bull.* **32,** 702–708 (2011).

36. Kim, S.-H. *et al.* Optofluidic Assembly of Colloidal Photonic Crystals with Controlled Sizes, Shapes, and Structures. *Adv. Mater.* **20,** 1649–1655 (2008).

37. Leunissen, M. E., van Blaaderen, A., Hollingsworth, A. D., Sullivan, M. T. & Chaikin, P. M. Electrostatics at the oil-water interface, stability, and order in emulsions and colloids. *Proc. Natl. Acad. Sci. U. S. A.* **104,** 2585–90 (2007).

38. Leunissen, M. E., Zwanikken, J., van Roij, R., Chaikin, P. M. & van Blaaderen, A. Ion partitioning at the oil-water interface as a source of tunable electrostatic effects in emulsions with colloids. *Phys. Chem. Chem. Phys.* **9,** 6405–14 (2007).

39. Kim, S.-H., Park, J.-G., Choi, T. M., Manoharan, V. N. & Weitz, D. A. Osmotic-pressure-controlled concentration of colloidal particles in thin-shelled capsules. *Nat. Commun.* **5,** 3068 (2014).

40. Shirk, K., Steiner, C., Kim, J. W., Marquez, M. & Martinez, C. J. Assembly of colloidal silica crystals inside double emulsion drops. *Langmuir* **29,** 11849–57 (2013).

41. Dinsmore, A. D. *et al.* Colloidosomes: selectively permeable capsules composed of colloidal particles. *Science* **298,** 1006–9 (2002).

42. Hsu, M. F. *et al.* Self-assembled shells composed of colloidal particles: fabrication and characterization. *Langmuir* **21,** 2963–70 (2005).

43. De Nijs, B. *et al.* Entropy-driven formation of large icosahedral colloidal clusters by spherical confinement. *Nat. Mater.* **14,** 56–60 (2015).

44. Hunter, G. L., Edmond, K. V. & Weeks, E. R. Boundary Mobility Controls Glassiness in Confined Colloidal Liquids. *Phys. Rev. Lett.* **112,** 218302 (2014).

45. Leunissen, M. E., van Blaaderen, A., Hollingsworth, A. D., Sullivan, M. T. & Chaikin, P. M. Electrostatics at the oil-water interface, stability, and order in emulsions and colloids. *Proc. Natl. Acad. Sci. U. S. A.* **104,** 2585–90 (2007).

46. Brugarolas, T., Tu, F. & Lee, D. Directed assembly of particles using microfluidic droplets and bubbles. *Soft Matter* **9,** 9046 (2013).

47. Hsiao, L. C., Newman, R. S., Glotzer, S. C. & Solomon, M. J. Role of isostaticity and load-bearing microstructure in the elasticity of yielded colloidal gels. *Proc. Natl. Acad. Sci. U. S. A.* **109,** 16029–34 (2012).

48. Shih, W.-H. *et al.* Mechanical Properties of Colloidal Gels. *MRS Proc.* **155,** 83 (2011).

49. Wilkins, G. M. H., Spicer, P. T. & Solomon, M. J. Colloidal system to explore structural and dynamical transitions in rod networks, gels, and glasses. *Langmuir* **25,** 8951–9 (2009).

50. Solomon, M. J. & Spicer, P. T. Microstructural regimes of colloidal rod suspensions, gels, and glasses. *Soft Matter* **6,** 1391 (2010).

51. Liu, B., Besseling, T. H., van Blaaderen, A. & Imhof, A. Confinement Induced Plastic Crystal-to-Crystal Transitions in Rodlike Particles with Long-Ranged Repulsion. *Phys. Rev. Lett.* **115,** 078301 (2015).

52. Noble, P. F., Cayre, O. J., Alargova, R. G., Velev, O. D. & Paunov, V. N. Fabrication of 'hairy' colloidosomes with shells of polymeric microrods. *J. Am. Chem. Soc.* **126,** 8092–3 (2004).

53. Madivala, B., Fransaer, J. & Vermant, J. Self-assembly and rheology of ellipsoidal particles at interfaces. *Langmuir* **25,** 2718–28 (2009).

54. Cates, M. E. & Candau, S. J. Statics and dynamics of worm-like surfactant micelles. *J. Phys. Condens. Matter* **2,** 6869–6892 (1990).

55. Cates, M. E. & Fielding, S. M. Rheology of giant micelles. *Adv. Phys.* **55,** 799–879 (2006).

56. Rogers, S. A., Calabrese, M. A. & Wagner, N. J. Rheology of branched wormlike micelles. *Curr. Opin. Colloid Interface Sci.* **19,** 530–535 (2014).

57. Dreiss, C. Wormlike micelles: where do we stand? Recent developments, linear rheology and scattering techniques. *Soft Matter* **3,** 956 (2007).

58. Fielding, S. M. Complex dynamics of shear banded flows. *Soft Matter* **3,** 1262 (2007).

59. Divoux, T., Fardin, M. A., Manneville, S. & Lerouge, S. Shear Banding of Complex Fluids. 16 (2015).

60. Dhont, J. K. G. & Briels, W. J. Gradient and vorticity banding. *Rheol. Acta* **47,** 257–281 (2008).

61. Fielding, S. M. Vorticity structuring and velocity rolls triggered by gradient shear bands. *Phys. Rev. E* **76,** 016311 (2007).

62. Méndez-Sánchez, A. F. *et al.* Particle image velocimetry of the unstable capillary flow of a micellar solution. *J. Rheol. (N. Y. N. Y).* **47,** 1455 (2003).

63. Nghe, P., Degré, G., Tabeling, P. & Ajdari, A. High shear rheology of shear banding fluids in microchannels. *Appl. Phys. Lett.* **93,** 204102 (2008).

64. Masselon, C., Colin, A. & Olmsted, P. D. Influence of boundary conditions and confinement on nonlocal effects in flows of wormlike micellar systems. *Phys. Rev. E* **81,** 021502 (2010).

65. Nghe, P., Fielding, S. M., Tabeling, P. & Ajdari, A. Interfacially Driven Instability in the Microchannel Flow of a Shear-Banding Fluid. *Phys. Rev. Lett.* **104,** 248303 (2010).

66. Lerouge, S., Argentina, M. & Decruppe, J. P. Interface Instability in Shear-Banding Flow. *Phys. Rev. Lett.* **96,** 088301 (2006).

67. Fielding, S. M. & Wilson, H. J. Shear banding and interfacial instability in planar Poiseuille flow. *J. Nonnewton. Fluid Mech.* **165,** 196–202 (2010).

68. Holmes, W. M., López-González, M. R. & Callaghan, P. T. Fluctuations in shear-banded flow seen by NMR velocimetry. *Europhys. Lett.* **64,** 274–280 (2003).

69. López-González, M. R., Holmes, W. M., Callaghan, P. T. & Photinos, P. J. Shear Banding Fluctuations and Nematic Order in Wormlike Micelles. *Phys. Rev. Lett.* **93,** 268302 (2004).

70. Ovarlez, G., Rodts, S., Chateau, X. & Coussot, P. Phenomenology and physical origin of shear localization and shear banding in complex fluids. *Rheol. Acta* **48,** 831–844 (2009).

71. Zhao, Y., Cheung, P. & Shen, A. Q. Microfluidic flows of wormlike micellar solutions. *Adv. Colloid Interface Sci.* **211,** 34–46 (2014).

72. Bécu, L., Manneville, S. & Colin, A. Spatiotemporal Dynamics of Wormlike Micelles under Shear. *Phys. Rev. Lett.* **93,** 018301 (2004).

73. Fardin, M.-A. & Lerouge, S. Instabilities in wormlike micelle systems. From shear-banding to elastic turbulence. *Eur. Phys. J. E. Soft Matter* **35,** 91 (2012).

74. Feindel, K. W. & Callaghan, P. T. Anomalous shear banding: multidimensional dynamics under fluctuating slip conditions. *Rheol. Acta* **49,** 1003–1013 (2010).

75. Fardin, M. A. *et al.* Shear-banding in surfactant wormlike micelles: elastic instabilities and wall slip. *Soft Matter* **8,** 2535 (2012).

Chapter 2 Spatially and temporally reconfigurable assembly of colloidal crystals[1]

2.1 Abstract

Directed, reversible and localized assembly of colloidal particles into three-dimensional ordered arrays is accomplished by the action of visible light. We find that poly(methyl methacrylate) colloids dispersed in a low-dielectric constant solvent in the vicinity of an indium tin oxide (ITO) coated surface concentrate and self-assemble under the action of a visible or UV light source. We use confocal microscopy to image the dynamics of the directed assembly process. The structure of the final photoinduced self-assembly is a function of the initial volume fraction of colloids, the power of the illumination, and the zeta-potential of the colloids. Over a broad range of conditions, the final self-assembly is a hexagonal ordered array of particles with a near-wall volume fraction as large as 0.49. We also observe a change from particle assembly (due to particle motion into the illuminated region) to particle disassembly (due to particle motion out of the illuminated region) as the concentration of the electrolyte, tetrabutylammonium bromide, is varied, consistent with a change in sign of the measured

[1] The text in this chapter was originally published in Y. Kim, A.A. Shah, & M.J. Solomon, *Nature communications* **5** (2014).

zeta-potential of the colloids. The photoinduced single-particle velocity in the z-direction is extracted from measurements of the assembly kinetics and found to be 0.28 ± 0.02 μm/s. Measurements of the effect in an electrochemical cell show that the directed assembly mechanism is consistent with electrophoretic motion of colloids induced by a transient current due to ion flow. We hypothesize that the electric field is generated by the mechanism of light-induced reaction of residual reactants, such as water and oxygen, at the ITO surface. This reaction drives an ion flow, which establishes a local, transient current. The method is used to create a complex shape structure in colloidal solutions by either concentrating or depleting particles from illuminated regions of interest. This method for spatially selective, reconfigurable colloidal assembly can be applied for photoinduced assembly of photonic crystals, low-power directed assembly of colloids, and photoresponsive materials.

2.2 Introduction

Colloidal assembly is a bottom up method to produce materials with new functional optical and mechanical properties[1]. Ordered assemblies of colloids are useful for applications in optics, such as optical filters and switches, and in displays, as in electronic ink. Although self-assembly is spontaneous and thermodynamically driven, the method suffers from slow kinetics and a lack of spatial control of the assembly process[2]. Directed self-assembly, in which organization is driven by the application of external fields, offers greater possibility for control over the assembly process. For example, directed self-assembly methods include controlled sedimentation in a gravitational field[3], DC electric field assisted migrations of particles to an electrode[4], induced interactions of polarizable particles in AC electric or magnetic fields[2], and microfluidic vortex flows in thermal fields[5]. While these directed assembly methods impart directionality and control over the assembly, their limitations include the need for instrumentation (e.g. AC or DC generators), the lack of rapid reversibility or spatial control (e.g. sedimentation), or the requirement of high power/high fields (e.g. on the order of 100V/cm for dielectrophoretic assembly[2]).

Photoinduced colloidal motion have been harnessed for directed assembly of colloids[5–8]. Advantages of photoinduced assembly are that it is non-invasive, requires simple experimental designs, and is easily reversible. Prior approaches include using the radiation pressure of light to propel objects[6]. Alternatively, optical triggers have been coupled to other external drivers to deliver additional control over the assembly process. For example, a blue laser has been used to induce diffusiophoretic assembly by activating a catalytic reaction at the exposed hematite surface of a particle, thereby generating a

chemical gradient of H_2O_2 and O_2[8]. The photochemical sensitivity of semiconductors has been used in conjunction with electric fields to drive electrophoretic[9] or dielectrophoretic[7] crystallization of colloids at illuminated regions. Alternatively, optically induced thermal gradients can be used in the presence of an electric field to generate electrothermal flows[5] to produce colloidal assemblies, including those with spatial patterning.

Here, we induce colloidal crystallization in spatially selective regions by using light to generate a local electric field. The local electric field directs colloidal motion by coupling to charge on the particle, thereby inducing electrophoresis that leads to colloidal assembly. The local electric field is generated by illuminating an indium tin-oxide (ITO) coated glass substrate at the base of a colloidal suspension with a 488 nm laser or an ultraviolet (UV) source. Localized illumination of the ITO coating results in motion of the particles either toward or away from the illuminated region. The assembly kinetics and structures are characterized in situ by direct visualization with a confocal laser scanning microscope. Because the method performs well in suspensions in which the particles are refractive index matched with the solvent, it complements methods for localized assembly based on radiation pressure, such as holographic particle trapping[10,11]. Furthermore, the method is fully reconfigurable, non-invasive, operates at low powers, generates structures with sharp features, and requires no instrumentation or complex optics to implement.

2.3 Method

200 μl of colloidal suspension were dispensed into a specimen vial with a cylindrical geometry of D = 10 mm and H = 1.25 mm. ITO coated microscope cover slips

(d = 0.170 mm) were used as the bottom surface of the vial. The ITO layer was in contact with the solution. The ITO coating was ~ 65 nm thick with a ~ 500 Ω/sq. sheet resistance (ZC & R Coatings for Optics, Inc.). In one set of experiments, to test what surface treatment was sufficient to yield the photoinduced assembly, a gold coating was used instead of the ITO coating. The gold in this case was a 15 nm layer deposited onto a 7.5 nm chrome layer (Denton Vacuum).

Two different electromagnetic radiation sources were used for the photoinduced assembly. First, 488 nm laser light was focused at the ITO coated cover slip using a 100× oil immersion objective lens (NA = 1.40). The light was projected onto a region of variable area, but typically was 25 × 25 μm^2. The laser power was delivered by the built in mechanism of a confocal laser scanning microscope (CLSM, Leica TCS SP2 or Nikon A1R), in which a pointwise scan of the region was performed with a duty cycle of 66%. The laser power used varied from 25 to 125 μW (Optical power meter Model 1916-C, Detector Model 818-ST, Newport). When scaled to the region-of-interest and the duty cycle, these values correspond to a mean power flux varying from 2.7 to 12 W/cm^2. Second, a UV light source (Leica EL6000, Mercury metal halide bulb, Filter A Cube) was used for illumination in some cases. This radiation was typically projected onto a circular region (D = 150 μm) and was delivered with a mean flux of 0.62 W/cm^2 (UV meter Model 306, 365 nm calibrated, OAI).

The colloidal particles used for photoinduced assembly were poly(12-hydroxy-stearic acid) (PHSA) stabilized poly(methyl methacrylate) (PMMA), with a mean diameter of 1.40-μm and 5.6% polydispersity (σ/D_{avg}, where σ is the standard deviation of particle diameter and D_{avg} is the average particle diameter[12]). Particles were dispersed

in a refractive index and density matched solvent mixture of 66 vol.% bromocyclohexane (CHB) and 34 vol.% decahydronaphthalene (decalin). These colloids have been broadly used in studies of colloidal assembly[13] for a number of reasons. First, the solvent mixture is nearly refractive index matched with the colloids. Therefore, van der Waals interactions are minimized, and the pair potential of the colloids is well approximated by a screened electrostatic potential. The refractive index matching also facilitates direct visualization by confocal microscopy. Second, the solvent mixture is nearly density matched with the colloids, so gravitational sedimentation is minimized. Previous studies of self-assembly with these colloids include the work of Pusey et al., Gasser et al., Yethiraj et al. and Leunissen et al[3,14–16].

Experiments were carried out in suspensions of initial volume fraction, ϕ_0, varying from 0.0125 to 0.20. 0 to 1000 μM of tetrabutylammonium bromide (TBAB) was added to the CHB/decalin solutions to investigate the effects of variable electrolyte concentration. These electrolyte concentrations resulted in a Debye layer thickness from 1.2 μm to 95 nm, respectively. Although the Debye layer thickness does change with TBAB concentration, TBAB concentration is also known to change the zeta-potential of the colloids[17], and it is this effect that will be of primary interest in this work.

CLSM was used to characterize the kinetics and structure of the photoinduced assembly (100× objective, NA=1.40). Typical imaging conditions were as follows: For assembly kinetics, time series of 100-150 frames (512 × 512 pixels) with spatial resolution of 49 nm/pixel were collected at a frame rate of 1.6 s. For the assembly structure, 3D image volumes of 150 slices were acquired at 512 × 512 resolution. The image volume was 25 ×25 × 7.5 μm^3 and the voxel size was 49 × 49 × 46 nm^3. To

determine the crystallization kinetics, structure, and density of the photoinduced assemblies, centroidal coordinates of all particles in 2D time series and the 3D image volumes were determined by image analysis methods discussed in Crocker et al. and characterized in Dibble et al [18,19]. The image analysis yielded centroidal coordinates resolved at the scale of ± 35 nm in the object plane and ± 45 nm in the axial direction. By means of the centroidal coordinates extracted from the image volumes, we characterized the crystallization kinetics in 2D by determining the time dependence of the number of particles identified in each image frame. The structure of the ordered array was visualized by rendering the centroidal coordinates from the image volumes. Local particle volume fractions as a function of height above the ITO coated coverslips were determined by evaluating particle number densities in slices of size 21 × 21 × 0.4 μm^3. The particle volume fractions of the crystals were calculated from the three layers closest to the coverslip. For the analysis of Figures 2.3 and 2.4, the near-wall volume fraction was that of the close-packed layer at the cover slip.

The laser induced colloidal velocity in the z-direction was calculated by adapting an analysis available for sedimentation kinetics, as discussed in Russel et al.[20] Here, only the particle velocity in the z-direction was considered because photoinduced motion was predominantly observed along the z-axis. The analysis is based on the fact that, given mass conservation, the time rate of change of volume fraction requires a flux in particle density that is consistent with a particular value of the colloidal velocity. In the present case, the driving force for colloidal motion is the force on the colloid due to the photoinduced effect, rather than the force of gravity as in the original theory. This theory

is one dimensional, assumes a uniform driving force, and accounts for the retardation of colloidal mobility as volume fraction increases, as per:

$$\frac{h_a}{t_a} = U_0 \frac{\phi_0 \mathrm{K}(\phi_0)}{\phi_a - \phi_0} \qquad \text{(Equation 1)}$$

Here, h_a is the height of the first crystalline assembly layer (h_a = 1.4 μm), t_a is the time to achieve an assembly of that height, ϕ_0 is the initial volume fraction of colloids, ϕ_a is the volume fraction of the crystalline assembly, $K(\phi) = (1- \phi)^{6.55}$ is the sedimentation coefficient and U_0 is the particle velocity in the z-direction[20].

Inspection of Equation 1 indicates that a plot of t_{sed} versus $\frac{h_{sed}}{U_0 \mathrm{K}(\phi_0)}\left(\frac{\phi_m}{\phi_0} - 1\right)$ yields the inverse of the photoinduced velocity (U_0). This characterization was carried out for experiments of photoinduced colloidal motion in a solvent with 1000 μM TBAB added and at a laser power density (at 488 nm) of 12 W/cm^2. Initial volume fractions were varied from 0.0125 to 0.20. As shown by Figure 2.6, the data follow a linear trend with a slope of 3.53 ± 0.29. The photoinduced particle velocity in the z-direction is therefore 0.28 ± 0.02 μm/s.

For UV induced assembly, the colloidal velocity was measured using a particle tracking method. Here, the distance that the particle traveled within two consecutive images were measured and divided by the frame rate (0.815 s) to calculate the particle velocity. From a series of ~200 images, several sequential images were extracted and analyzed to determine the average velocity. For this experiment, a dilute solution of 1.25% volume fraction was prepared to easily locate individual particles at 1 mM TBAB

concentration in CHB/decalin. The power of the UV light was measured as 0.62 W/cm^2 and the area of illumination was 1.8×10^{-8} m^2.

Particle zeta potential and photoinduced current measurements were made in the DC electric field device described by Shah et al[4]. Zeta-potential measurements were carried out in 1.25 vol.% particle suspensions prepared at four different electrolyte concentrations: 0, 5, 100, and 1000 μM TBAB in CHB/decalin. Particle mobility was tracked in planes perpendicular to the cover slip as a constant current was applied with the potentiostat (Autolab PGSTAT 128N) across the solution. Images were collected at 0.815 s per frame. Given the measured mobility, the electric field set up by the applied current, solvent properties (ε = 5.962, μ = 0.0025 Pa s) and the electrolyte properties (Λ^0_{TBA+} = 6.5 cm^2 S/mol and Λ^0_{Br-} = 14.5 cm^2 S/mol), zeta-potentials were computed by the method of O'Brien and White[21].

Similarly, current measurements were conducted by measuring the current density within the suspension as light illumination was turned on and off. UV illumination of 360 nm peak wavelength at 0.62 W cm^{-2} was applied. The potentiostat was used to measure the current density variations under a constant zero potential. The minimum current sensitivity of the potentiostat is about 100 pA with the ECD module.

The Region-of-Interest (ROI) stimulation method was used on a Nikon A1R confocal laser microscope system (100× oil objective, NA = 1.49) to create assembly and disassembly structures of complex shapes. Simultaneous imaging and stimulation scanning were done with a resonant scanner at a frame rate of 0.067 s. Imaging was conducted with a 561.6 nm laser, while stimulation was carried out with a 405 nm laser. Stimulation area was defined by the ROI designed as a specific shape on the confocal

software. Images of 512 × 512 pixels were collected at a spatial resolution of 0.249 μm/pixel.

2.4 Results & Discussion

For a solution of colloidal particles dispersed in CHB/decalin at a salt concentration of 50 μM, when a 25 μm × 25 μm region of the ITO coated substrate was illuminated with a laser power flux of 12 W/cm^2, accumulation of particles was observed in the vicinity of the illuminated region (Figure 2.1 a-c). The time required for accumulation of a solution of 5 vol.% particles was about 60 s. These images were acquired in the particle layer immediately above the ITO coated substrate. At this condition, as in many others, the accumulation of particles was sufficient that colloidal crystal ordering was observed (Figure 2.1e). The greatest concentration of particles was found within the illuminated region. However, we observed some particle accumulation outside the illuminated region as well. That is, the particle accumulation extends slightly beyond the laser exposure area, as shown in Fig 2.1e. The slightly reduced fluorescence emission of the central portion in Figure 2.1e is caused by photo bleaching of the zoomed in region of interest.

The particle accumulation effect only occurred for the case of a conductive or semi-conductive substrate. For example, replacing the ITO coating with gold still yielded particle accumulation under the same laser power and solvent conditions (Figure 2.1 f,g). The corresponding control experiment, with illumination of an (uncoated) silica cover slip, yielded no particle accumulation (Figure 2.1 h,i). The assembly was also a sensitive function of TBAB concentration in the solvent. For example, Figure 2.1 j,k shows that these colloids were expelled from the illumination region when the solvent was pure CHB/decalin with no added TBAB. (This effect is discussed further in Figure 2.4.)

Particle accumulation was also observed at other illumination wavelengths. For example, illumination with a mercury metal halide lamp (peak wavelength = 360 nm) yielded accumulation of particles as indicated by Figure 2.1 l,m.

Thus, Figure 2.1 summarizes a directed assembly phenomena that was found to occur under a variety of conditions, all connected by the common feature that electromagnetic illumination is coupled to an absorptive, conductive substrate such as ITO. The following additional characterization of the generality of the photoinduced effect is available:

First, there is a strong effect of solvent conditions on whether or not any photoinduced effect is observed. While organic, low dielectric constants systems, such as CHB and decalin, demonstrated significant photoinduced assembly response to electromagnetic illumination, systems of higher dielectric constants, such as dimethyl sulfoxide (DMSO) and water, showed little to no photoinduced effect. The role of solvent dielectric constant on self-assembly of the colloids studied here has been previously established[15], and the present effect is consistent with those prior discoveries.

Second, in solvents in which particles do display the photoinduced effect, whether or not assembly or disassembly is observed is a strong function of the kind of colloids used. The photoinduced effect was studied for PMMA colloids with various surface stabilizers and polystyrene (PS) colloids. Assembly was observed under a variety of conditions for PMMA colloids. For example, assembly occurred for different substrates illuminated (gold and ITO coating), varying wavelengths of the laser (458 nm, 476 nm, and 488 nm), laser powers ranging from 2.7 to 12 W/cm^2, initial volume fraction of particles from 0.0125 to 0.20, and particle sizes from 0.6 to 1.4 μm. All of these

experiments were carried out with PHSA stabilized PMMA colloids in CHB/decalin with 1 mM TBAB electrolyte. Other surface functionalized PMMA particles, such as polydimethylsiloxane (PDMS) and diphenyldimethylsiloxane (DPDMS), showed disassembly at the illuminated region, similar to that observed in PHSA-PMMA system with no TBAB. PS particles demonstrated no signs of assembly in both water and dimethylsulfoxide (DMSO) solvents of 0.1 mM TBAB with visible light, whereas, under UV illumination, PS particles were found to generate a better assembly in DMSO than in water.

Third, for particles and solvents that show the photoinduced effect, the magnitude of the effect, as indicated by the speed of the assembly and the extent of the ordered structures formed, is a function of whether visible or UV light is used. With the UV illumination (360 nm), a more enhanced assembly phenomenon was observed (Figure 2.1 l,m) compared to visible light induced assemblies. The larger area of particle accumulation is a result of the UV light delivered to the entire field of view of the objective. Such effective assembly process was observed for both PHSA-PMMA and PS particle suspensions (in water and DMSO, independently). For these cases, PMMA particle suspensions were prepared in 1 mM TBAB solution of CHB/decalin.

The photoinduced assembly phenomenon extends a significant distance into the solution from the ITO coated coverslip. The penetration depth of the accumulation effect was found to be about 20 μm into the suspension at steady-state (Figure 2.2a). 3D crystalline structures were formed out to this distance in regions subjected to illumination. For this experiment, particle suspension was prepared in a 50 μM TBAB solution in CHB/decalin. Images were acquired in a plane perpendicular to the ITO

coated surface. The dimensions of the crystalline region in Figure 2.2a are about 25 × 25 μm^2 with a depth of about 15 particle layers.

The 3D structure of the colloidal crystal was characterized through image analysis. A rendering of particle coordinates identified from the confocal microscopy image volumes is shown in Figure 2.2c. Hexagonal ordering with some defects was observed, as indicated in the confocal microscopy image and the corresponding rendered image (Figures 2.2 b, d). The ordering induced by the light was further quantified by measuring the dependence of local particle volume fraction on distance above the ITO coated coverslip, as plotted in Figure 2.2e. In Figure 2.2e, the local colloid volume fraction, as derived from the centroidal data, was plotted against z/D, the distance from the cover slip scaled on the particle diameter (Figure 2.2d). Volume fraction profiles are plotted for experiments at two different power densities (2.7 and 12 W cm^{-2}).

The structural characterization of the assembly in Figure 2.2e shows interesting features of the directed assemblies produced by the light. First, as indicated by the alternation between maximum and minimum number density in the assembly, the structure is layered, consistent with the structure of a colloidal crystal. Second, there is an effect of intensity of the light excitation on the layered structure and spatial variation in density. Particle volume fractions at each layer of the assembly decrease as depth into the sample increases, as evidenced by the decrease in peak height with z/D. Differences between the crystals formed from two different laser powers are also apparent. The highest volume fraction peak for the 12 W/cm^2 sample reached 0.49 at the first layer closest to the cover slip, whereas for the 2.7 W/cm^2 sample, it was found to be 0.32. Note however, that both of these self-assemblies have crystalline structure. The

crystalline volume fraction is roughly consistent with that of phase transition boundary expected for charged colloids, given the measured screening length and zeta potential ($\phi_{theory} = 0.36$)[20].

Figure 2.3 shows the kinetics of the photoinduced assembly process. First, the characteristic time scale for assembly is about 60 s. This time scale is apparent in Figure 2.3 a-f, where the accumulation effect is shown as a function of time in a series of CLSM images. Particle suspensions for these experiments were prepared in 50 μM TBAB solution of CHB/decalin. Upon laser exposure, particles rapidly deposited from the suspension onto the region of illumination. Particles begin to concentrate a few seconds after the ITO coated surface is exposed to the intensified laser (Figure 2.3b), until a crystalline structure is formed. Deposited particles display hexagonal crystal ordering in about 65 s (Figure 2.3e).

Second, the photoinduced assembly volume fraction monotonically increases with time upon illumination, as plotted in Figure 2.3g. Five samples, with initial volume fractions varying from 0.0125 to 0.20, were tested. The number of particles accumulated in the layer above the ITO coated cover slip monotonically increased until a steady-state volume fraction was reached.

Third, the time it takes for the system to reach its steady-state, crystalline volume fraction is a decreasing function of both the initial volume fraction of particles and the power density of the laser applied. From Figure 2.3g, a characteristic time for crystallization, t_c, was defined as the time for the assembly to reach 99% of its steady-state volume. Figure 2.3h shows that t_c decreases with increasing initial volume fraction and laser power.

Fourth, the sedimentation analysis of Russel et al. was used to infer a particle velocity from the crystallization time measurements. Given this analysis, the photoinduced particle velocity was found to be 0.28 ± 0.02 μm/s in the z-direction for the conditions of the experiments, which are: ϕ_0 varying from 0.0125 to 0.20, at a salt concentration of 1000 μM TBAB, and at a laser power density of 12 W/cm^2. Therefore, the decrease in crystallization time with increasing initial volume fraction is a consequence of the faster filling of the assembly region at higher initial volume fraction due to the greater local availability of colloids. That is, at low initial volume fraction, it takes longer to crystallize the near wall layer because colloids must be drawn from a larger region, and it takes additional time for colloids to convect in from longer distances by virtue of the light induced effect. The finding that the crystallization times imply a particle velocity that is independent of volume fraction places an important constraint on possible assembly mechanisms, as we will discuss shortly.

As previously discussed, for PMMA colloids with PHSA stabilization in the solvent CHB/decalin, the effect of light on assembly was a strong function of added electrolyte concentration. Because this unusual effect could yield information about the mechanism of the assembly, we investigated it further. For this study, TBAB concentration was varied from 0 to 1000 μM in CHB/decalin.

Figure 2.4 shows a transition from disassembly to assembly phenomenon with varying electrolyte conditions in our photoinduced systems. First, the reversal of the photoinduced effect occurs between TBAB concentrations of 7.5 μM and 8.75 μM. Below the threshold condition of 7.5 μM, the depletion of particles was observed from the illuminated region (Figure 2.4 a-c). The depletion effect increased (that is, the

concentration of particles in the void created by the light was lower) for decreasing levels of salt in the system, as demonstrated by the observation of a colloid-free illumination region at steady-state for 0 μM TBAB (Figure 2.4a). Between salt conditions of 8.75 – 10 μM, the system demonstrated weak driving force for assembly, as evidenced by the observation that the light in this region could concentrate colloids, but that the accumulation effect was not strong enough to generate a colloidal crystal. A disordered, liquid structure was instead observed (Figure 2.4d). For TBAB concentration greater than 20 μM, the steady-state assemblies generated by the light were crystalline. Increasing salt concentration led to a small increase in assembly volume fraction in this range of TBAB concentration. This small change is likely due to the crystalline structure having smaller particle separations for higher salt concentrations, due to the small change in Debye length with TBAB concentration.

The effect of TBAB on the photoinduced assembly was quantified by measuring the local, near wall colloid volume fraction as function of time. Consistent with qualitative observations, a decrease in ϕ is shown for salt conditions below 7.5 μM and increase in ϕ is shown for salt conditions above 8.75 μM (Figure 2.4g). Near steady-state volume fractions were reached for all conditions. By plotting the final volume fraction measured at each TBAB condition, the abrupt transition from disassembly (at low TBAB concentration) to assembly (at high TBAB concentration) is apparent, as shown in Figure 2.4h. The abruptness of the change, and the fact that is occurs at a finite TBAB concentration, argues against the effect of TBAB being its role in change the Debye length. Rather, as we will show in Figure 2.5, the abrupt change at ~ 8 μM TBAB is more likely due a TBAB's known effect on the zeta potential.

Taken together, these results constrain possible mechanisms of the photoinduced assembly. To summarize, the mechanism must be consistent with: (1) local colloid motion of ~ 0.3 μm/s induced when a metallic or semiconducting substrate is illuminated with 488 nm visible light at a power of 12 W/cm^2 (for the UV case, the corresponding measured velocity is 1.8 μm/s at a power of 0.62 W/cm^2); (2) near refractive index matching ($\Delta n < \sim 0.003$) of the colloids and solvent; (3) change from disassembly to assembly due to a switch in the direction of particle migration at ~ 8 μM when TBAB concentration is varied between 0 and 1000 μM.

A number of possible mechanisms for the photoinduced assembly appear inconsistent with these three characteristics of the effect. First, the effects of radiation pressure and optical trapping[6,22] are ruled out by the facts that the assembly phenomenon was specific to metallic or semiconducting coatings and that the colloidal system itself was refractive index matched (and radiation pressure and trapping forces are therefore negligible). Second, particle migration due to natural convection driven by possible laser heating of the conductive substrate is ruled out due to the small Rayleigh number of the system, which we find to be below the critical instability to induce convection. The computed Rayleigh number for experiments report here is 80, and the critical number for instability is ~ 1100[23].

In addition, thermophoresis, particle motion induced by a temperature gradient, was investigated as a possible mechanism for the colloidal motion. To evaluate this possibility, we modeled the temperature gradient in the illuminated region by solving the time-dependent heat transfer equations with the commercially available solver COMSOL. The governing equation is:

$$\rho C_p \frac{\partial T}{\partial t} + \rho C_p \mathbf{u} \cdot \nabla T = \nabla \cdot (k \nabla T) + Q \qquad \text{(Equation 2)}$$

where ρ is the fluid density, C_p is the fluid heat capacity at constant pressure, k is the fluid thermal conductivity, **u** is the fluid velocity field and Q is the heat source (units = W/m^2). Simulation dimensions were taken as the values described in the previous experimental section. The simulation duration was 60 s, which matched the experimental duration. Parameter values used, as taken from the literature, were: k = 0.1195 W/m/K, ρ = 1176 kg/m^3, and C_p = 1428 J/kg/K [24]. These values are weighted averages of individual solvent parameters of CHB and decalin. A constant input heat flux boundary condition was imposed at the central 25 × 25 μm^2 region for visible laser simulation, and at the central 150 μm diameter circular region for UV light simulation, located on the bottom boundary of the geometry. Thermal insulating conditions were used for the other boundaries.

The constant heat flux imposed at the bottom boundary was determined in the following way: The thermal power absorbed at the illumination region was calculated using the Beer-Lambert law with ITO absorption coefficient values at 488 and 360 nm (10865 cm^{-1} and 18851 cm^{-1}, SOPRA N&K Database). Heat flux into the system was calculated to range from 2.7 to 12 W/cm^2 The mesh dimension was scaled by adaptive mesh refinement to resolve the region of illumination while still simulating to the specimen boundaries (refined mesh dimension from 3 μm at the center region of illumination to 1 mm at the boundary). The time step of the simulation was 0.001s. The outputs of the simulation were time dependent temperature profiles and temperature gradient profiles in the three-dimensional region simulated.

At the largest heat flux of 12 W/cm^2, the temperature profile after 60 s showed an increase of about 1.5 K at the region closest to the cover slip (Figure 2.7a). This established a maximum temperature gradient of 10^5 K/m in the z-direction, as shown by Figure 2.7b. The spatially variation for the temperature and temperature gradient was along the z-axis is plotted in Figure 2.7c. This information was used to compute thermophoretic velocities by means of[25]:

$$v_T = -D_T \nabla T \qquad \text{(Equation 3)}$$

where v_T is the thermophoretic velocity (in μm/s), D_T is the thermal diffusivity (or thermophoretic mobility), and ∇T is the thermal gradient. From the simulated temperature gradient, and a thermal diffusivity value of 1 μm^2 s^{-1} K^{-1} (typical for micron sized colloidal particles[26]), the thermophoretic particle velocity was computed to be about 0.1 μm/s at the cover slip. This velocity decreased very rapidly above the ITO substrate (Figure 2.7d).

The thermophoretic mechanism is therefore inconsistent with our observations for the following reasons. First, the magnitude of the velocity, under best conditions, is still a factor of three less than the value inferred from the time to crystallization data of Figure 2.4. Second, the computed thermophoretic velocity decreases rapidly above the substrate; however, the volume fraction dependence of the time to crystallization is consistent with a uniform force on the colloids that yields a constant velocity. Third, the thermophoresis mechanism is not consistent with the observed reversal in direction of colloidal motion observed at 8 μM TBAB. As a final check, we attempted to artificially generate thermophoresis in the system of the magnitude predicted for the illuminated powers. We used a heated objective to achieve an increase in temperature at the cover

slip of about 1.5 K (about what the finite element simulations predict) and no observable particle motion was observed.

A potential mechanism for the photoinduced effect is suggested by Figure 2.5a. Measurements of the zeta potential of the PMMA colloids show a remarkable coincidence between the sign of the measured colloid zeta potential (which reverses at ~ 20 μM TBAB) and the switch of the effect from disassembly to assembly (which occurs at ~ 8 uM TBAB). This sensitivity of PMMA colloid zeta potential to TBAB concentration, including a change in sign of the zeta potential, is consistent with prior literature for these colloids[17,27]. The coincidence of the TBAB concentrations for the switch from disassembly to assembly and for the change in sign of the PMMA colloid zeta potential suggests that the photoinduced assembly effect is induced by light-induced electrophoresis of the colloids. We now critically examine this possibility.

A photoinduced electrophoretic mechanism for the colloidal assembly would imply the existence of an electric field in the system. While no electrode geometry has been designed into the system, the metallic surface itself is potentially reactive[9,28]. The surface could therefore be a substrate for chemical reactions. The subsequent depletion in chemical specties at the substrate would result in an ion flow. This ion flow is a current that yields an electric field as per:

$$E = \frac{j}{\lambda_0} \qquad \text{(Equation 4)}$$

where j is the measured current density (per illuminated area) and λ_0 is the conductivity of the solution[29]. Thus, if photoinduced electrophoresis is the mechanism for the observed directed assembly, then, a current ought to be set up in the system when light illuminates the ITO substrate. The current itself may be quite small, because the

illuminated area itself is small (~ 1.8×10^{-8} m^2 in most cases studied.) The magnitude and direction of the current should be consistent with the magnitude and sign of the colloid zeta-potential. Ion flows of the kind hypothesized here have previously been reported for low dielectric constant solvents, including CHB/decalin[4].

To test this hypothesis, we performed the following experiment: For a solution of 5 vol.% particles in CHB/decalin with 1000 μM TBAB, the current density, j, was measured as UV illumination (peak wavelength = 360 nm, 0.62 W cm^{-2}) was turned on and off (Figure 2.5b). We find a significant change in the current density as the UV light is switched on and off. Simultaneously, CLSM images were collected, and are shown in Figure 2.5 c-e. These images demonstrate that the photoinduced assembly indeed occurred as the current density changed due to the illumination. Similar types of photoinduced current modulation have been observed in the past[9], but never in the absence of an externally applied electric field. Here, instead, the electric field is generated internally, by the ion flow resulting from reactions at the ITO substrate mediated the introduction of light.

The results of Figure 2.5 are broadly consistent with an electrophoretic mechanism for the photoinduced assembly because the application of light coincides with both a change in current density and the observation of assembly. We find that additional details of the Figure 2.5 experiments are also consistent with the mechanism. First, the sign of the different quantities are all consistent. Given the electrochemical cell configuration, the measured negative cathodic current indicates that the illuminated electrode has positive polarity. Thus, colloids with a negative zeta-potential (at 1000 μM TBAB) are driven into the illuminated region, as observed. Second, the up and down

motion of the microscope's optical scanner is observable in the current density (Figure 2.4b). Figure 2.4b shows sinusoidal variation in the current density. The frequency of the variation coincides with the scanning frequency of the optical scanner used for the experiment (1.635 s). As the scanner propagates upwards from the coverslip to acquire the assembly images (c.f. Figure 2.3c-e), the light-ITO interaction decreases, and the measured current shifts toward its "off" value. The fact that the laser scanning is observable in the current measurement, in addition to the large change in current induced by the UV light, suggests that the visible laser itself is able to induce change in the system as well, consistent with the method working well with the 488 nm laser. Third, the magnitude of the colloidal velocity predicted from the electric field is consistent with direct measurements of UV induced velocities. Given the electric field (1.5×10^4 V/m) set up by the photoinduced current density, the viscosity of the solvent (0.0025 Pa s), and the colloidal zeta potential at 1000 μM TBAB (-9 mV), the electrophoretic colloid velocity was estimated to be ~ 4 μm/s, roughly consistent with ~ 2 μm/s from direct measurements of colloid motion during the UV induced crystallization.

A light induced electrophoretic mechanism for the photoinduced assembly immediately suggests a means to generate colloidal crystal arrays that reconfigure in space and time. In particular, the understanding that the sign of the colloid zeta-potential determines whether or not the particles accumulate or deplete from the illuminated region means that the light can be used to either regions of assembled or disassembled particles. The fact that the phenomenon requires a light/reactive substrate interaction means that the effect is extremely localized in space. Figure 2.5 f-i shows application of this understanding to create complex shapes of colloids. A 405 nm laser scanned this

intricate design, drawn as a region-of-interest by the microscope's optical scanner. Assembly of the structure (Figure 2.5 f,g) was carried out under the following conditions: 1000 μM TBAB in CHB/decalin in contact with an ITO coated cover slip with a colloidal solution prepared at 5% initial volume fraction. Disassembly (Figure 2.5 h,i) was induced under similar conditions but with a 0 μM TBAB concentration and at a 10% initial volume fraction.

We find that colloids rapidly assemble and disassemble within few seconds of illumination to form these structures with sharp features and well-defined boundaries. The definition of these features and boundaries are as good for the case of disassembly as for assembly. Both of the structures created are fully reversible. The results indicate the method's rapidity, reversibility, spatial specificity, and versatility for producing both assembled and disassembled regions of colloids. With these characteristics, the photoinduced electrophoretic method has broad application in reconfigurable assemblies, especially for the template-free, spatially selective assembly of colloidal crystals.

2.5 Conclusion

We induced localized, reversible colloidal crystallization by using light to generate an electric field that establishes electrophoretic motion of colloidal particles. We discovered that the photoinduced electrophoretic assembly is specific to light coupling with conductive substrates, such as gold or ITO. With that feature in common, a variety of conditions were studied to understand the effect of the solvent, particles, and light illumination wavelength. The 3D structure of the final assembly showed a layered crystalline structure with a spatially varying density that decayed as distance into the sample increased. The highest volume fraction of the assembly was about 0.49; this result

was observed at the region closest to the cover slip. Analysis of the assembly kinetics demonstrated that the photoinduced assembly occurs through a monotonic increase in particle concentration as the particles travel with photoinduced z-directional velocity of about 0.28 μm/s. The phenomenon reversed from disassembly to assembly as the TBAB concentration reversed from 7.5 μM and 8.75 μM; this switch coincided with the change in sign of the measured zeta potentials of the particle. The method developed in this paper is broadly applicable to photoresponsive materials, assemblies of photonic crystals, and represents a new kind of template-free, reconfigurable colloidal photolithography.

2.6 Figures

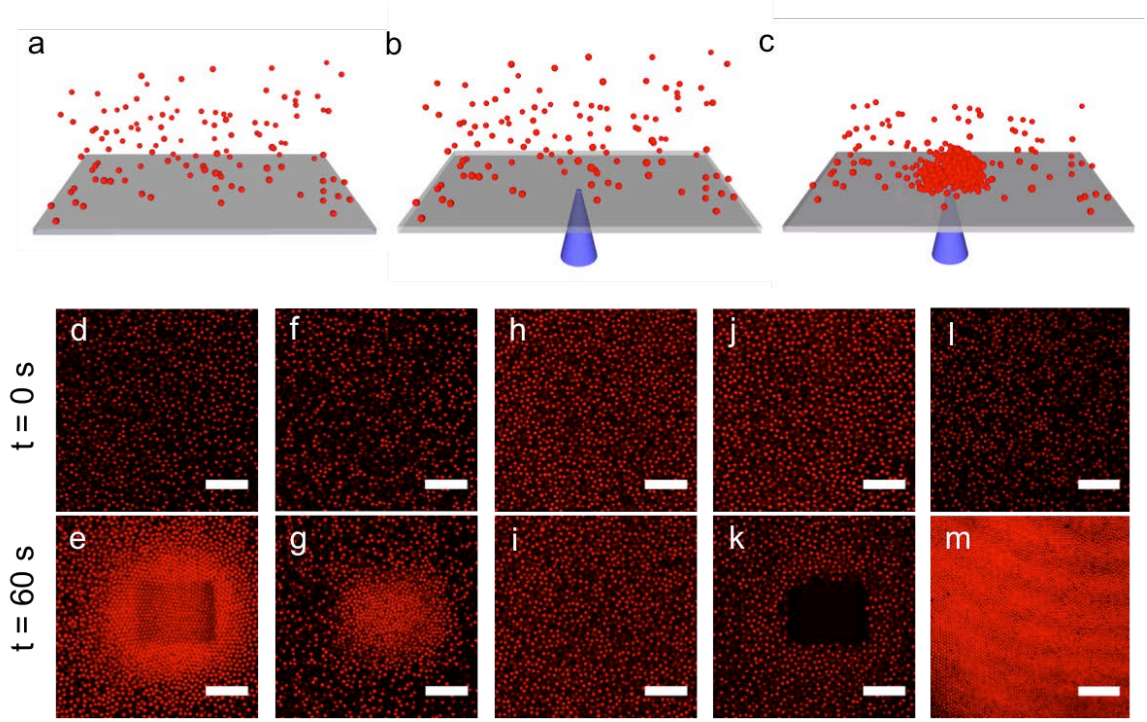

Figure 2-1 Photo-induced colloidal assembly phenomenon.

(a) 1.4 μm PHSA-stabilized PMMA colloids at an initial volume fraction of 0.05 are initially dispersed in solution in contact with the ITO coated glass substrate. (b) A 488 nm laser or UV light source is focused at the objective and scanned across a region of interest. (c) Particle accumulation is observed at the illuminated region. (d-m) Each image pair shows the colloidal structure before and after 60 s of excitation at 488 nm with power density 12 W cm^{-2} (d-k) and excitation at 360 nm with power density 0.62 W cm^{-2} (l-m). The solvent is CHB/decalin with 50 μM TBAB added (d-i, l-m) or no added TBAB (j,k). In images (d-e,j-k,l-m) the solution is in contact with an ITO coated substrate; (f,g) the solution is in contact with a gold coated substrate; (h,i) is a control experiment in which the solution is in contact with a pure silica substrate. Scale bars are 20 μm.

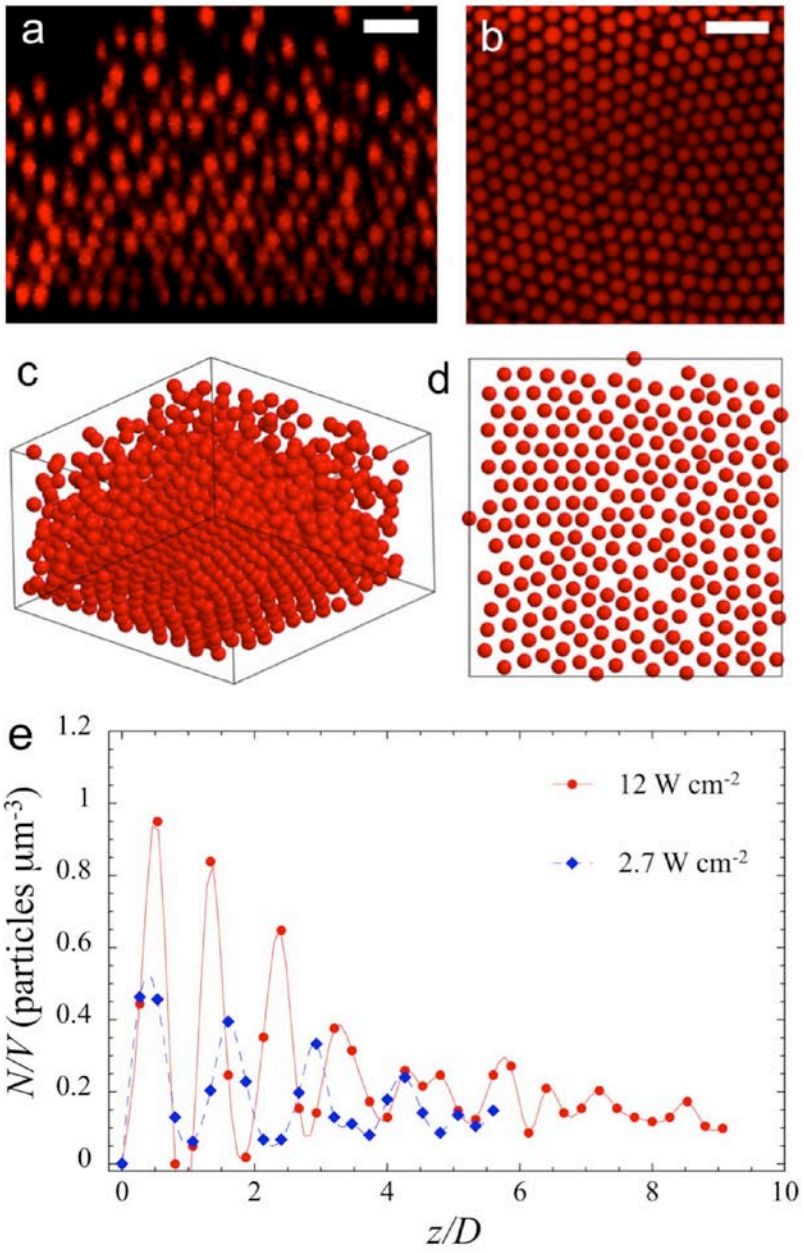

Figure 2-2 Three-dimensional structure of the photo-induced assembly.

The particle and solvent conditions are as in Figure 2.1e and the illumination time is 120 s. (a) Image acquired perpendicular to the ITO coverslip shows accumulation of multiple layers of colloids above the region of illumination. Scale bar is 5 μm. (b) Image of the same structure acquired at the ITO coverslip. Scale bar is 5 μm. (c) 3D rendering of CLSM-derived colloid centroids shows crystalline structure; colloid centroids were identified by image processing; (d) Rendering of the crystalline layer closest to the cover slip, which shows hexagonal ordering, with some defect structure. (e) Particle number density (N/V) of the assembly is a function of distance from the substrate and laser power density.

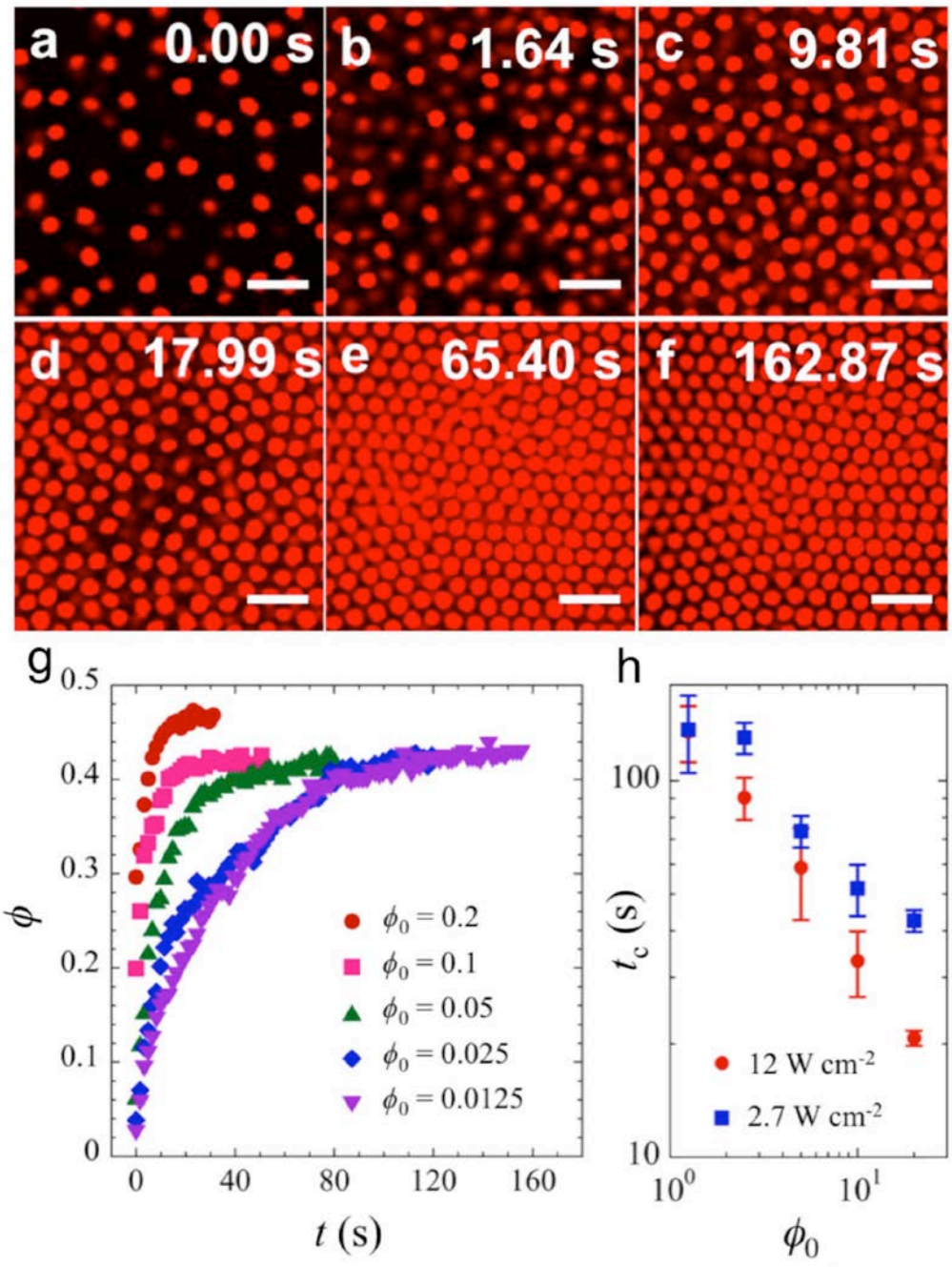

Figure 2-3 Kinetics of assembly under optical field excitation.

(a-f) Time lapse images of PMMA particles (ϕ_0 = 0.05) concentrating in the 25 × 25 μm^2 region that was illuminated. The particle and solvent conditions are as in Figure 2.1e. Scale bar is 5 μm. (g) Particle volume fraction, ϕ, monotonically increases until it reaches steady-state. (h) Quantification of the critical concentration time, t_c, shows that time for accumulation decreases with increasing laser power density and initial volume fraction. The error bars indicate s.d.

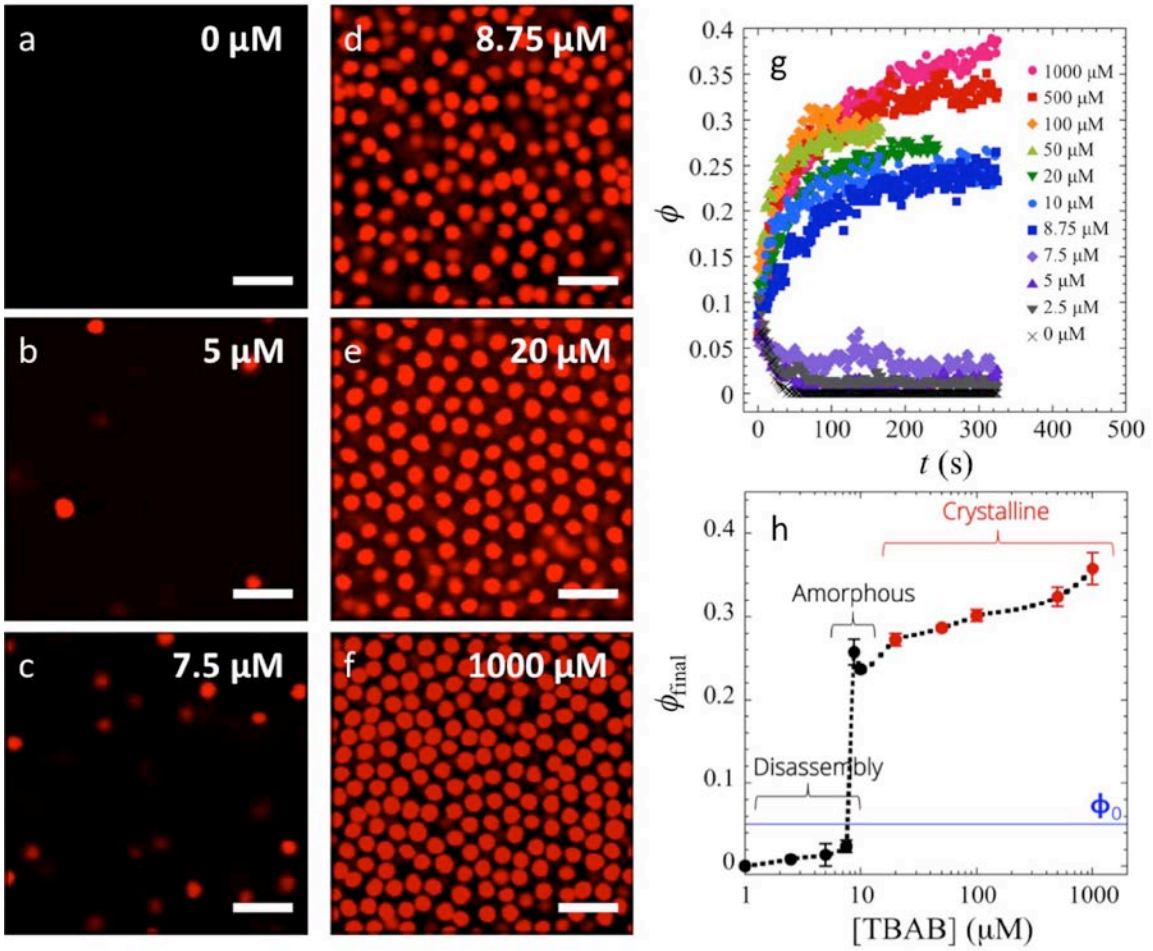

Figure 2-4 Influence of the TBAB concentration on the photoinduced effect.

Images are acquired 150 s after illumination and the initial colloid volume fraction is 0.05. For these colloids, the particle zeta potential is a known function of TBAB concentration. (a-c) Images show PMMA colloid migration away from the illuminated region, thereby generating a void region of low colloid concentration. (d-f) Images show PMMA colloid migration toward the illuminated region, thereby leading to concentration and assembly. Scale bar is 5 µm. (g) For TBAB concentrations under 7.5 µM, ϕ decreases from its initial volume fraction, indicating depletion of particles within the region of interest. Above 7.5 µM TBAB, the volume fraction increases monotonically to a higher final volume fraction. (h) Final volume fraction values are extracted from (g) and plotted against their TBAB concentrations. There is a distinct transition between 7.5 µM and 8.75 µM TBAB; depletion is observed below this transition and assembly is observed above. The error bars indicate s.d.

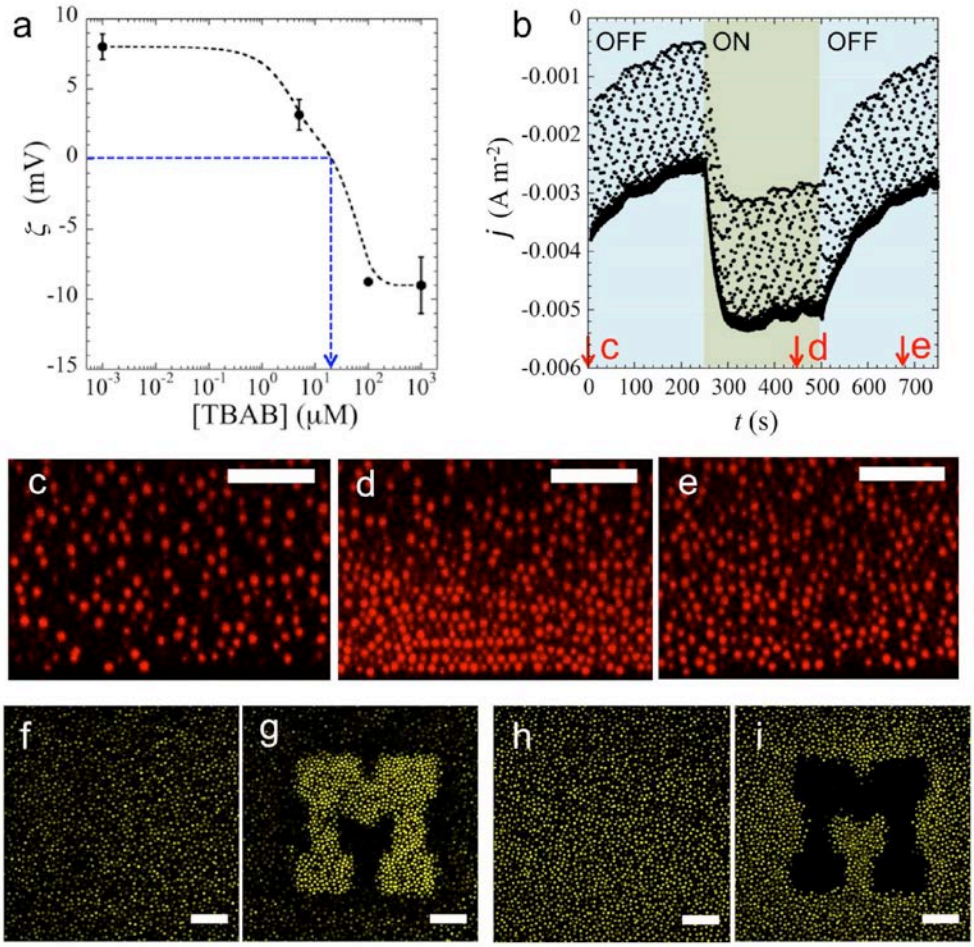

Figure 2-5 Electrophoretic origin of the photo-induced assembly mechanism.

(a) Zeta potential values of PHSA stabilized PMMA colloids undergo a change in sign at about 20 μM added TBAB. The dotted curve is a line to guide the eye. The error bars indicate s.d. (b) When the photoinduced effect is generated in a cell with electrodes, the measured current exhibits a rapid change as a direct response of the UV light being turned on and off. This experiment was carried out with PHSA stabilized PMMA colloids prepared at 5% volume fraction and 1000 μM concentration of TBAB. (c-e) CLSM images corresponding to the times marked in (b). Images taken perpendicular to the cover slip show that the effect of light on the particle assembly is temporally correlated with changes in current density due to the illumination. Scale bar is 15 μm. (f-i) Because the current density is produced only in the illuminated region, the photo-induced assembly and depletion effects can be achieved when complex shapes are illuminated by the light, as is possible by, for example, using the optics of the scanning microscope. (f-g) Before and after images of colloidal assembly show accumulation of particles in the illuminated region of complex shape. The colloidal solution was prepared at 5% initial volume fraction with 1000 μM TBAB in CHB/decalin. (h-i) Before and after images of colloidal depletion show depletion of particles within the illuminated region of complex shape. The initial colloidal volume fraction was 10% and the solvent was pure CHB/decalin. Scale bars are 20 μm.

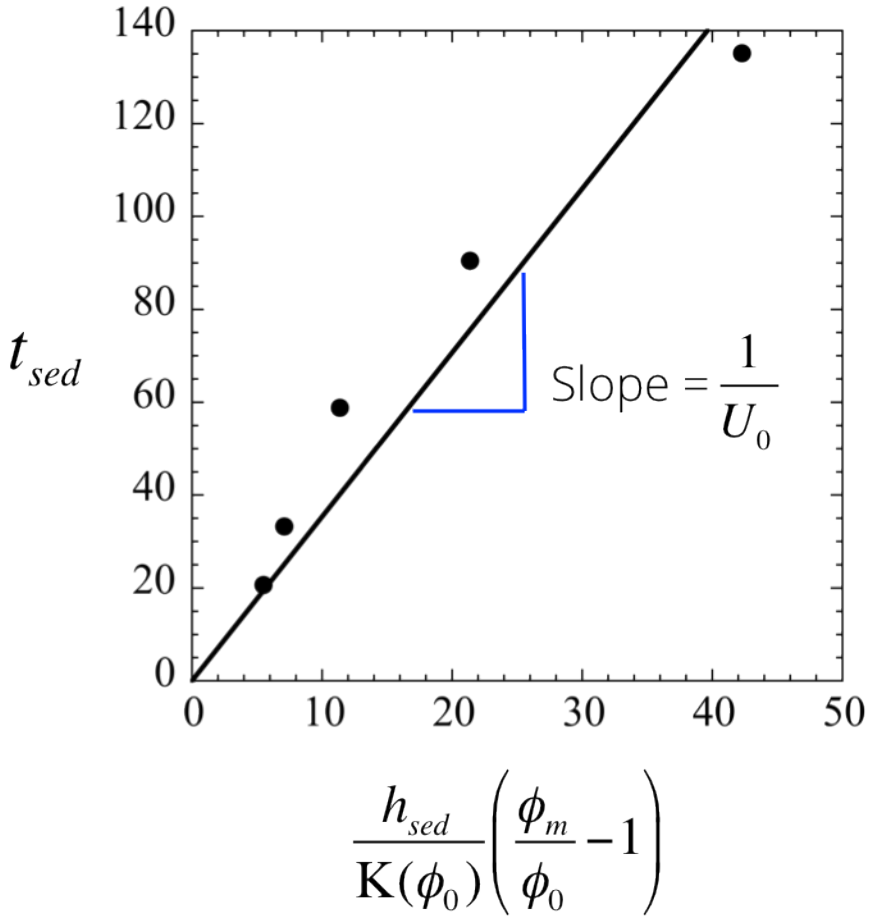

Figure 2-6 Calculation of the photo-induced colloidal velocity.

Analysis of Eqn. 1−1 and data of Figure 2.3 used to infer the velocity of colloids induced by the illumination with visible light. The time for accumulation experiments prepared at five different initial volume fractions (0.0125, 0.025, 0.05, 0.10, 0.20) are plotted against parameters given. Solutions are prepared at 1000 μM TBAB concentration. The slope of 3.51 ± 0.29 is inversely related to the colloidal velocity.

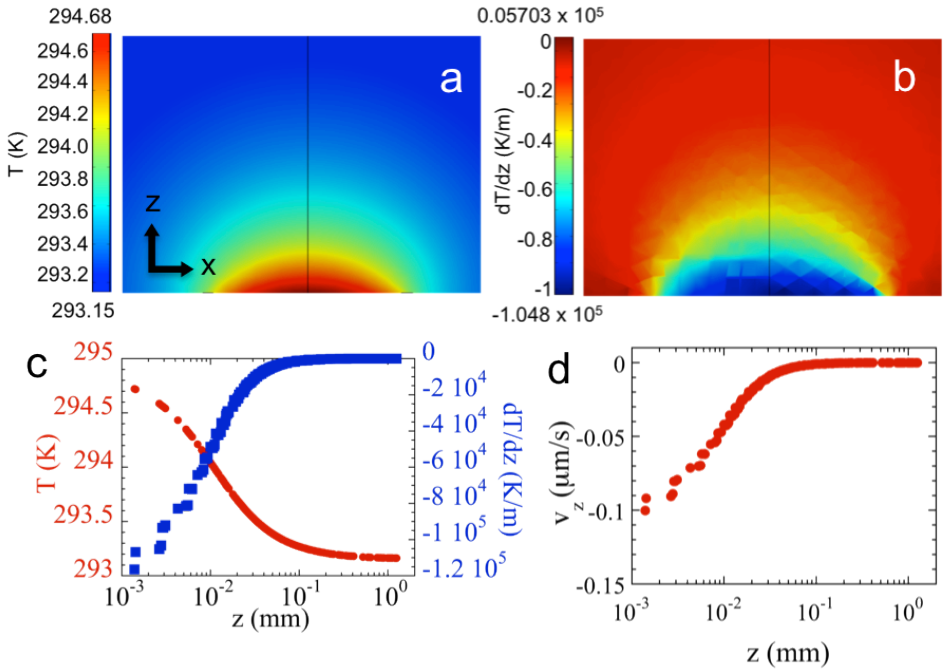

Figure 2-7 Results of the finite element method analysis of thermophoresis.

Results of the heat transfer calculations in the illuminated region using the finite element method to assess the possible role of thermophoresis in generating the photoinduced effect. Input heat flux was set at 12000 W/m^2. (a-b) Temperature and temperature gradient profiles on the xz-plane demonstrate a maximum temperature of 294.68 K and a temperature gradient of 104800 K/m at the lower cover slip, where the heat flux is being applied. (c) Temperature and temperature gradients extracted along the z-axis show a decay further into the solution, away from the cover slip. (d) With a thermal diffusivity value of 1 μm^2 s^{-1} K^{-1}, particle velocities at varying z distances are calculated and plotted. Due to a fast drop in temperature gradients, velocities drop quickly to negligible values by 20 μm way from the ITO coated coverslip.

2.7 References

1. Glotzer, S. C. Materials science. Some Assembly Required. *Science* **306,** 419–20 (2004).

2. Grzelczak, M., Vermant, J., Furst, E. M. & Liz-Marzán, L. M. Directed self-assembly of nanoparticles. *ACS Nano* **4,** 3591–605 (2010).

3. Pusey, P. N. & van Megen, W. Phase behaviour of concentrated suspensions of nearly hard colloidal spheres. *Nature* **320,** 340–342 (1986).

4. Shah, A. A. *et al.* Liquid crystal order in colloidal suspensions of spheroidal particles by direct current electric field assembly. *Small* **8,** 1551–62 (2012).

5. Williams, S. J., Kumar, A., Green, N. G. & Wereley, S. T. A simple, optically induced electrokinetic method to concentrate and pattern nanoparticles. *Nanoscale* **1,** 133–7 (2009).

6. Ashkin, A. Acceleration and Trapping of Particles by Radiation Pressure. *Phys. Rev. Lett.* **24,** 156–159 (1970).

7. Gong, T. & Marr, D. W. M. Photon-directed colloidal crystallization. *Appl. Phys. Lett.* **85,** 3760 (2004).

8. Palacci, J., Sacanna, S., Steinberg, A. P., Pine, D. J. & Chaikin, P. M. Living crystals of light-activated colloidal surfers. *Science* **339,** 936–40 (2013).

9. Hayward, R., Saville, D. & Aksay, I. Electrophoretic assembly of colloidal crystals with optically tunable micropatterns. *Nature* **404,** 56–9 (2000).

10. Grier, D. G. A revolution in optical manipulation. *Nature* **424,** 810–6 (2003).

11. Van Blaaderen, A. Colloids under external control. *MRS Bull.* **29,** 85–90 (2004).

12. Xu, S. *et al.* Generation of Monodisperse Particles by Using Microfluidics: Control over Size, Shape, and Composition. *Angew. Chemie* **117,** 734–738 (2005).

13. Xia, Y., Gates, B., Yin, Y. & Lu, Y. Monodispersed colloidal spheres: Old materials with new applications. *Adv. Mater.* **12,** 693–713 (2000).

14. Gasser, U., Weeks, E. R., Schofield, A., Pusey, P. N. & Weitz, D. A. Real-space imaging of nucleation and growth in colloidal crystallization. *Science* **292,** 258–62 (2001).

15. Yethiraj, A. & van Blaaderen, A. A colloidal model system with an interaction tunable from hard sphere to soft and dipolar. *Nature* **421,** 513–7 (2003).

16. Leunissen, M. E., van Blaaderen, A., Hollingsworth, A. D., Sullivan, M. T. & Chaikin, P. M. Electrostatics at the oil-water interface, stability, and order in emulsions and colloids. *Proc. Natl. Acad. Sci. U. S. A.* **104,** 2585–90 (2007).

17. Royall, C. P., Leunissen, M. E. & Blaaderen, A. van. A new colloidal model system to study long-range interactions quantitatively in real space. *J. Phys. Condens. Matter* **15,** S3581–S3596 (2003).

18. Crocker, J. C. & Grier, D. G. Methods of Digital Video Microscopy for Colloidal Studies. *J. Colloid Interface Sci.* **179,** 298–310 (1996).

19. Dibble, C. J., Kogan, M. & Solomon, M. J. Structure and dynamics of colloidal depletion gels: Coincidence of transitions and heterogeneity. *Phys. Rev. E* **74,** 041403 (2006).

20. Russel, W. B., Saville, D. A. & Schowalter, W. R. *Colloidal Dispersions*. (Cambridge University Press, 1992).

21. O'Brien, R. W. & White, L. R. Electrophoretic mobility of a spherical colloidal particle. *J. Chem. Soc. Faraday Trans. 2* **74,** 1607 (1978).

22. Ashkin, A., Dziedzic, J. M. & Yamane, T. Optical trapping and manipulation of single cells using infrared laser beams. *Nature* **330,** 769–71 (1987).

23. Bird, R. B., Stewart, W. E. & Lightfoot, E. N. *Transport Phenomena*. (John Wiley & Sons, 2007).

24. Yaws, C. L. *Yaws' handbook of thermodynamic and physical properties of chemical compounds physical, thermodynamic and transport properties for 5,000 organic chemical compounds /*. (Knovel, 2003).

25. Piazza, R. & Parola, A. Thermophoresis in colloidal suspensions. *J. Phys. Condens. Matter* **20,** 153102 (2008).

26. Shiundu, P. M., Williams, P. S. & Giddings, J. C. Magnitude and direction of thermal diffusion of colloidal particles measured by thermal field-flow fractionation. *J. Colloid Interface Sci.* **266,** 366–376 (2003).

27. Leunissen, M. E. *et al.* Ionic colloidal crystals of oppositely charged particles. *Nature* **437,** 235–40 (2005).

28. Van den Meerakker, J. E. A. M., Meulenkamp, E. A. & Scholten, M. (Photo)electrochemical characterization of tin-doped indium oxide. *J. Appl. Phys.* **74,** 3282 (1993).

29. Bard, A. J. & Faulkner, L. R. *Electrochemical Methods: Fundamentals and Applications*. **6,** (Wiley, 2000).

Chapter 3 Transient, near-wall shear-band dynamics in channel flow of wormlike micelle solutions[†]

3.1 Abstract

We report the spatiotemporal dynamics of shear bands in wormlike micelle solutions as generated in the near-wall region of rectangular channel flow. In this system, a very thin (< 2 μm) high shear band is generated, stacked along the gradient axis of the channel flow. By means of confocal microscopy and particle image velocimetry, we observe the effect of these thin bands on both steady-state flow profiles and transient variations in the flow that are non-uniform along the vorticity direction. The steady-state velocity profiles deviate from a parabolic shape above an applied wall shear rate of 6 s^{-1}, in good correspondence with the measured rheology. Kinetically, the deviation from parabolic flow presents as the development of a thin, near-wall band flowing at a high shear-rate. The band dynamics along the vorticity (neutral) axis of the flow are observed at distances from 2 to 10 μm from the wall. At the smallest near wall position of 2 μm,

[†] This chapter has been submitted for publication by Y. Kim, A. Adams, W. Hartt, R.G. Larson & M.J. Solomon.

space-time plots reveal four distinct stages of the velocity variation with time along the vorticity axis. First, the flow accelerates at all points along the vorticity axis to about one-half of the final, steady-state velocity at that position in the gap. Second, a deceleration – again at all points in the flow-vorticity plane – abruptly slows down the fluid motion at this near wall region. The total change in velocity resulting from the deceleration is about one-half that of the previous acceleration. Third, the flow partitions into multiple bands along the vorticity direction of variable velocity. The width of these bands is dependent on the shear rate; their width is ~ 100 μm for flow with a wall shear rate of 8.4 s^{-1}. Finally, all the fast bands combine to form a single homogeneous flow with a fast velocity at 2 μm from the wall. This velocity is ~ 50 times that expected for unbanded flow with the same flow rate. We discuss these shear band spatiotemporal dynamics in the context of transient vorticity structuring that occurs at applied shear rates within the stress plateau region.

3.2 Introduction

Wormlike micelles (WLM) are long, flexible, cylindrical aggregates of amphiphilic surfactant molecules[1]. These flexible micelles form and increase in length above a critical surfactant concentration or upon addition of salt that screens the electrostatic interactions of the head groups[2]. With further increase of surfactant or salt concentration, entangled and branched networks[3] form. The linear viscoelastic rheological response of WLM solutions arises from reptation and reversible scission. The latter phenomenon is distinct from what is observed for polymers[4]. Reptation and scission results in linear viscoelasticity described by a single-mode Maxwell model[5].

The constitutive response of WLM solutions in steady shear flow yields a dependence of stress on shear rate that is non-monotonic[6]. In the region of this flow curve with zero or negative slope, homogeneous flow is unstable. The flow instead breaks into shear bands stacked along the gradient axis of the flow, with each band flowing at a different shear rate[7]. More generally, the nonlinear viscoelastic constitutive response of wormlike micelle solutions can generate flow instabilities[6]. In addition to the aforementioned (gradient) shear banding[6,8], vorticity banding[9,10], and apparent wall slip[11–13], interfacial instability between shear bands at steady state[14–16] and oscillating, chaotic bands[17,18] are reported. Each of these phenomena is linked to the rheological response of the wormlike micellar microstructure to the imposed flow.

Gradient shear banding (i.e., with stacking direction of the bands being along the direction of the velocity gradient) is widely observed in WLM solutions. The banding behavior of WLM solutions is attributed to the separation of the two regions into distinct microstructures[19]. These structural differences can arise from micellar alignment[20] or

from concentration differences between the bands[5]. Several recent studies also show flow velocity fluctuations along the vorticity direction in shear-banded flows at band interfaces[14,15,21,22] or within the high shear rate band[23]. This flow heterogeneity along the vorticity direction is referred to as vorticity structuring[6]. These structures may be generated by normal stress differences between the bands[6,9], fluctuating slip that causes instability in the high shear rate band[23], or an elastic instability of the high shear rate band[24].

Gradient banding and vorticity structuring are observed in both channel flow and Taylor-Couette flow geometries at steady state. In Taylor-Couette geometries, Salmon et al. observe a sharp interface between the two shear bands and an increase in the high shear rate band thickness with increasing applied shear rate[25]. Strong wall slip is also observed in these geometries in contact with the high shear rate band [24] or in the low viscosity phase[21]. Channel flow is simple to generate, can be operated in the range of shear rates for which shear banding is observed, and is a good model of industrial conduit flows. In channel flow, Callaghan et al. observe a flow instability above a critical strain rate for wormlike micelles and connect it to the spurt effect as identified by Vinogradov for polymer melts[26]. Above a critical flow rate, the velocity profile changes from parabolic with zero velocity at the wall to a parabolic profile with an apparent finite velocity close to the wall; at even higher flow rates, plug-like flow is observed[11,26–29]. The plug-like flow is accompanied by a high shear rate band near the wall[13,26,28,29] and/or a layer of apparent wall slip[11,13,14,27]. Nghe et al. also observe interfacial instability leading to velocity variation along the vorticity direction of shear-banded flows in

microchannels at steady-state, apparently induced by a normal stress jump across the bands[14].

It is argued by Ober et al. that observations of apparent wall slip is consistent with the hypothesis of gradient shear banding generated by a non-monotonic flow curve[29]. Specifically, if we assume that the viscosity of each band differs by ~ 3 orders of magnitude, then the band thickness can be as small as ~ 100 nm in a flow with a gap ~ 1 mm. In this case, apparent wall slip and gradient shear banding are essentially the same phenomenon. (See also, Ref. 30 for an alternative view.)

The previous literature principally addresses banding at steady-state[14,25–29]. Studies of band transient behavior[15,21,23,24,30] upon start up of flow provide additional understanding of the flow-microstructure interactions that generate the instability. Moreover, certain industrially important flows, such as bottle filling, are unsteady[31]. Studies of transient banding can shed light on behavior in such flows.

Transient band phenomenology includes temporal fluctuations along the vorticity direction at band interfaces or near the wall in shear-banded fluids[15,23,24]. Specifically, Becu et al. report a slow evolution and growth of the banded state (~ 6 hours) and periodic oscillations at the band interface caused by oscillations in apparent wall slip velocities[21]. Similar interfacial instabilities are observed by Lerouge et al. and Fardin et al.[15,22] Other transient measurements focus on understanding the underlying mechanism of shear banding[30]. Lopez-Barron et al. demonstrate that the microstructure of wormlike micelle solution initially undergoes an elastic rheological response, with a large stress overshoot, followed by the formation of a transient, flow-aligned state.

The prior transient studies are all in Taylor-Couette flow. Curved streamlines contribute to elastic instabilities in this case; the flow geometry is therefore a factor in explanations of vorticity structuring. There is consequently value in studying transient banding in rectangular channel flow, as findings in this geometry (without curvature) can be compared to results in Taylor-Couette flow (with curvature). Such a comparison and identification of the near-wall dynamics of transient banding can assist the development of shear banding models[6,32].

Here, we present direct measurements of the spatiotemporal evolution of near-wall vorticity dynamics in rectangular channel flow. Using particle image velocimetry, we obtain both the steady state and transient velocity profiles along the gradient direction of the flow. The transient mean velocity profiles near the wall show fluctuating velocities at intermediate times and an abrupt increase to the steady state value after the onset of shear banding. We also observe that this thin, near-wall region (less than 2 μm) of locally high shear rate displays complex spatiotemporal dynamics along the vorticity direction. These vorticity dynamics accompany the formation of the near-wall gradient shear band and are observed at distances up to 10 μm away from the wall in the gradient direction of flow.

3.3 Methods

Two anionic surfactant wormlike micelle solutions that show gradient shear banding at convenient shear rate ranges are studied. The first system is 42 wt.% sodium lauryl ether 3 sulfate (SLE3S), 24 wt.% sodium lauryl sulfate (SLS) and 3.5 wt.% sodium chloride (NaCl) in deionized water. In addition, at one condition, 1.9 wt.% NaCl is used instead to vary the internal microstructure of the WLM system. The second system is 10

wt.% sodium lauryl ether 1 sulfate (SLE1S) and 2.15 wt.% NaCl in deionized water. The amount of salt in these solutions is adjusted to obtain comparable entangled microstructures to the SLE3S/SLS system with 3.5 wt.% NaCl. Both solutions are found near the maximum point on the "salt curve" (cf. Appendix A, Figure A-1).

The linear viscoelasticity and steady shear rheology of the SLE3S/SLS solution is measured by controlled stress rheometry (AR-G2, TA Instruments) using a 40 mm diameter, 2° steel cone at 21.5°C. The storage (G') and loss (G'') moduli, as reported in Figure 3.1a-b, are measured at frequencies from 0.1 to 100 rad/s. A single-mode Maxwell model fit[33] yields the relaxation time, $\lambda_M = 0.14$ s, and the elastic modulus, $G_0 = 510$ Pa. The steady-state viscosity is measured at shear rates from 0.1 to 100 s^{-1}, as shown in Figure 1c. The near independence of the shear stress for shear rates greater than 4.5 s^{-1} is consistent with the onset of shear banding[5]. Time dependent stress measurements are also made at shear rates of 2.2, 6.1, and 11.7 s^{-1} (Figure 3.1d). The stress overshoot at low times can be explained as the initial elastic response of the WLM solution. For all measurements, a solvent trap is placed over the sample to minimize sample evaporation.

Rectangular channel flow at constant volumetric flow rates is generated in a flow cell (IBI Scientific) of dimension 0.8 mm x 4 mm x 40 mm. Three walls of the rectangular channel are made of polycarbonate. The fourth boundary is a 160 μm thick glass cover slip through which the flow is visualized. The WLM solution is delivered to the flow cell using a syringe pump (10 ml capacity, KDS 100, Fisher Scientific). The syringe is connected to the flow cell using an aluminum pipe (1/8"). The flow apparatus has a slow time constant (~ 500 s) for reaching steady-state flow when pumping high

viscosity fluids at low rates (below 2.2 s^{-1}); the WLM solutions studied here are in this category. At high rates, above 20.1 s^{-1}, the (rise) time constant to reach steady flow is much faster (~ 20 s). The regimes of transient shear banding dynamics reported in this paper do not overlap with the rise times of the flow. To ensure that the results are independent of these mechanical effects, all steady state measurements are taken long after the flow reaches its steady flow rates (15 minutes for the slowest flow case, 2.2 s^{-1}, to 3.5 minutes for the fastest flow case, 20.1 s^{-1}). Moreover, comparison of the flow rate rise times to the transient velocity measurement shows that the transient behavior observed (~ 100 s from flow start-up) is significantly later than the time constant (~ 20 s) of the flow (c.f. Appendix B). The (applied) shear rates of the flows are calculated at the channel wall based on the volumetric flow rates, which are directly measured.

The wormlike micelle solutions are seeded with 500 nm, yellow-green fluorescent dye polystyrene particles (Invitrogen) at a volume fraction of ~ 0.00001. Particles are visualized with Nikon A1R confocal laser scanning microscope with a 488 nm laser. A 20X objective (NA = 0.75) is used under the resonant scanning mode (0.067 s/frame) to generate 512 x 512 pixel images with a pixel resolution of 1.23 μm/pixel. As shown in the left most panel in Figure 3.2a, frames are taken at varying focal planes (xy plane, flow-vorticity plane) within the channel. To illustrate: two consecutive frames (in green and red in the right most panel) with Δt = 0.067s are analyzed to extract particle velocities. For measurements at steady-state conditions, the depth of the focal plane is varied between 2 μm and 798 μm along the gradient direction (z-axis). At each gradient position, the middle 15% of the flow along the vorticity direction is imaged. Images are taken at 2, 10, 50, 100, 250, 400, 550, 700, 750, 790, and 798 μm above the glass cover

slip for steady state velocity profiles at shear rate conditions varying from 2.2 s^{-1} to 20.1 s^{-1}. For transient measurements, images are acquired at 2 μm above the cover slip. The duration of individual experiments varies based on the shear rate studied, ranging from 15 minutes for the slowest flow case (2.2 s^{-1}) to 3.5 minutes for the fastest flow case (20.1 s^{-1}).

We use an open-source PIV software, PIVlab, to analyze the flow behavior within the channel[34]. Prior to image processing, contrast limited adaptive histogram equalization (CLAHE) is applied[35]. Once image contrast modification is completed, each pair of frames is divided into interrogation windows of dimension 64 x 64 pixels, as shown in Figure 3.2a, middle panel. For each of these interrogation windows, a 2D Fast Fourier Transform (FFT) is calculated. Then, the FFT at one time point is multiplied by the conjugate of the interrogation area FFT at the second time point (Figure 3.2b). The cross correlation matrix of the pixels within the interrogation areas of the two frames is obtained by inverse FFT of the product, as per the correlation theorem. From the cross correlation matrix, the particle velocity is determined, as illustrated in Figure 3.2b.

This process is repeated to generate a vector distribution for the entire image. To obtain a high-resolution vector field, multiple passes are taken with decreasing interrogation window size; the initial displacement data from the large interrogation areas are used to spatially offset the interrogation windows in the following passes. Specifically, for our analysis, three passes of 256, 128, and 64 square pixel interrogation areas are used. An example of a final vector map is shown in Figure 3.2b. Some spurious vectors, resulting from poor illumination of local regions or particles traveling out-of-field, are removed and interpolated. (The number of these interpolated vectors is

below 5% in each experiment). We further validate the PIV method by comparing results for several instances to those generated by direct particle tracking. Particle velocity information is extracted along a line (0.63 mm) in the vorticity direction at 6 time points (1.1, 1.7, 2.2, 2.8, 3.4, 3.9 minutes) and compared to the velocities from particle tracking along the same line (Appendix C). The mean deviation between PIV and particle tracking ranges from 0.4% to 16% at the highest case, with a mean deviation across all cases of 3%. More detailed description of the validation process and results can be found in Appendix C.

3.4 Results

Strong deviations from a parabolic profile are observed at shear rates above 6 s^{-1} for the SLE3S/SLS solution (Figure 3.3a). Under these conditions, a thin region of high velocity exists at the wall, because the measurement at the nearest wall position (2 μm) is already at finite speed at these high shear rates. The high velocity region is observed at both the top and bottom boundaries, and for two different boundary materials – borosilicate glass and polycarbonate. The near-wall velocities, taken at 2 μm from the cover slip, increases linearly as the applied shear rate is increased from 6.1 s^{-1} to 20.1 s^{-1} (Figure 3.3b). The flow conditions at which increased velocities are observed coincide with the shear rates of the stress plateau in the steady-shear rheology curve (Figure 3.1b). The appearance of a high velocity region near the wall, initiated at a shear rate corresponding to the plateau region of the shear rheology, is consistent with shear banding.

Velocity profiles similar to that of Figure 3.3a are measured by Ober et al. In that case, slip-like layers are observed for flows of moderate Weissenberg numbers (Wi <

5)[29]. In the present case, the Wi number for all flow conditions studied varies from 0.05 to 0.5, with the onset condition (6.1 s^{-1}) corresponding to Wi = 0.14. The Weissenberg number is defined as $\lambda_M \langle U \rangle / H$, where λ_M is the Maxwell model relaxation time (0.14 s), $\langle U \rangle$ is the average velocity calculated from the volumetric flow rate, and *H* is the channel height (800 μm).

Figure 3.3c reports high-resolution microscopy measurements that resolve the region very close to the wall. A 100X objective (NA = 1.45) is used to generate 512 x 512 pixel images with a pixel resolution of 248 nm/pixel. In a region 4 μm and less from the wall, control measurements with a Newtonian fluid show linear behavior, consistent with the shear rate applied (11.7 s^{-1}) and the no-slip boundary condition (cf. Appendix D). Based on the sizes of the tracer particles (500 nm), the nearest wall measurement is made at 250 nm from the wall. For the WLM solution, a large velocity is measured over the entire 4 μm region and a flat profile persists to the minimum dimension that the PIV method could resolve (Figure 3.3c). The near-flat profile indicates that the high shear rate band next to the wall must be less than 250 nm thick. (A tighter bounding of the depth of this thin shear banded region is beyond the capabilities of our optical microscopy methodology.) The dotted line is an estimate of parabolic flow in an 800 μm channel within the 4 μm region, given the existence of a near wall velocity equal to the magnitude measured at the point nearest the wall. The data agree well with parabolic estimate, suggesting that the near wall-region is consistent with the parabolic velocity measured in the remainder of the low-rate band.

To analyze the shear rate dependence of the banded flow, the measured velocity profiles are fit to a parabolic velocity profile with an added slip velocity. The slip

velocity values are as reported in Figure 3.3b – the measured velocity at a gradient height of 2 μm. The best-fit parabola, less the slip velocity, is compared to the measurements (also shifted by the slip velocity) in Figure 3.4a. The fit parameter is the apparent shear rate of the (low-rate) banded flow. These shear rates are plotted against the applied shear rates of the flow in Figure 3.4b. The two lines in Figure 3.4b represent bounding cases. The curve with slope one is for Newtonian (unbanded) flow; the horizontal line at 4.5 s^{-1} is the onset condition for banded flow, as deduced from Figure 3.1c.

The data, within error, appear to track the two bounds. First, at low applied shear rates (between 2.2 to 6.1 s^{-1}), the measured shear rates agree with the imposed values, as indicated by the red curve. Second, at high nominal shear rates (above shear rates of 6.1 s^{-1}), the shear rates extracted from the parabolic fit scatter in the vicinity of the horizontal line of $\dot{\gamma}_{ss}$ = 4.5 s^{-1}. Recall that the horizontal bound is derived from the rheological measurements (Figure 3.1c). Therefore, the plateau observed above the critical shear rate (4.5 s^{-1}), suggests that the bulk contains a low shear rate band whose steady-state velocity profile is consistent with the measured shear rheology of this fluid.

The kinetics of the development and evolution of the high shear rate band are examined by measuring the time-dependent velocity at a gradient height of 2 μm (Figure 3.5), averaged across the vorticity axis of the flow. Transient velocity profiles for the shear rate range below the critical shear rate for banding (2.2 – 6.1 s^{-1}) are shown in Figure 3.5a. A monotonic increase in <v> is observed for all conditions. Large time constants (e.g. ~ 500 s for 2.2 s^{-1}) result because of the very high viscosity of the WLM solutions at low shear rates (e.g. 41 Pa s at 2.2 s^{-1}), as discussed in the Methods section.

For conditions above shear banding (8.4 – 20.1 s^{-1}), large fluctuations in <v> are observed at intermediate times. These fluctuations are followed by abrupt increases in the <v> to steady-state values (Figure 3.5b). This transition is most pronounced under the fastest flow condition, 20.1 s^{-1}, where the increase in <v> occurred within < 20 s and only a brief intermediate period of fluctuations is measured. Overall, the time to steady banded flow decrease with the imposed shear rate (Figure 3.5c).

Figure 3.6a plots the time-dependence of the average velocity at five distances from the wall (i.e., along the gradient direction) for an imposed shear rate of 11.7 s^{-1}. Two main observations can be made. First, the velocity is non-monotonic at 2 μm distance from the wall. The magnitude and the duration of the intermediate fluctuations vary from trial to trial, as shown by comparable shear rate conditions in Figure 3.5b of 11.7 s^{-1} flow. (Larger fluctuations are observed for the same shear rate condition in Figure 3.5b.) However, the overall qualitative characteristics of the flows are consistent. Second, the time it takes for the system to reach its steady-state (t_{ss}), is the longest at 2 μm from the wall. Figure 3.6b plots t_{ss} as a function of distance from the wall. While the time measured at 2 μm is indeed larger than the others, apart from this t_{ss} is largely independent of distance from the wall. Thus, only near the wall is the mean velocity non-monotonic, and this non-monotonicity may be correlated with an increased time to reach steady state.

Figure 3.7 identifies the origin of these near-wall flow behaviors. The velocity field in the flow/vorticity plane at a gradient height of 2 μm is reported at six different time points varying from t/t_{ss} = 0.40 to 0.93. Measurements are for an imposed shear rate 8.4 s^{-1}. At short times, the velocity increases monotonically at all points in the flow-

vorticity plane (Figures 3.7a,b). At t/t_{ss} = 0.77, the velocity begins to vary along the vorticity direction, breaking into thin, randomly positioned, high velocity bands (Figure 7c), coexisting with slowly-moving regions (Figure 3.7c). Over time, the high velocity bands grow thicker by merging together, until only 1-2 thin slow moving regions persist, as shown in Figures 3.7d,e. By t/t_{ss} = 0.93, a homogeneous flow with a fast velocity is achieved at all points along the vorticity direction (Figure 3.7f). This steady-state velocity near the wall is ~ 50 times greater than expected for an unbanded flow of a Newtonian fluid at the same flow rate. The observation of these transient dynamics indicates that the velocity fluctuations and the long times to steady state (Figure 3.6b) are strongly coupled with the spatially-dependent velocity field near the wall.

Space-time plots of the flow are generated for six different flow conditions (4.4, 8.4, 10.0, 11.7, 14.0, and 20.1 s^{-1}) as shown in Figure 3.8. These plots record spatiotemporal patterns of the flow along the vorticity direction, labeled as "y." They are constructed from the velocities along the vorticity direction (y) taken at each time frame (0.067 s) over the duration of the flow. Below the critical shear rate for banding (4.4 s^{-1}), a gradual increase in velocity is observed (Figure 3.8a) as similarly reported by transient average velocity measurements. There is no strong spatial variation in the flow along the vorticity axis.

Figures 3.8b-f report the vorticity-direction variation in the band velocity for shear banding conditions (8.4, 10.0, 11.7, 14.0, and 20.1 s^{-1}). The space-time plots show the temporal development of high velocity regions at the walls. The process has four distinct steps. Each step is observed for all conditions; here we describe the development for 8.4 s^{-1} (Figure 3.8b). First, flow accelerates uniformly across the vorticity plane. The

acceleration time ranges from ~ 55 to 150 s. The acceleration reaches about one-half of the steady-state, average velocity at this gradient position. Second, the entire observed flow along the vorticity direction decelerates to ~ one-half of the mean velocity observed in the first step. The deceleration is short lived (~ 5-10 s). Third, the flow breaks into multiple bands of different velocity at points along the vorticity direction. The width of the fast moving bands depends on the imposed shear rate condition and is ~100 μm for 8.4 s^{-1}. A single, wide fast band is observed for the 11.7 s^{-1} flow. The vorticity bands grow in width over time during this step by the mechanism of band combination and growth. The duration of this phase is dependent on the shear rate conditions studied. For 8.4 s^{-1} condition, the characteristic time for the vorticity banding phenomenon is ~ 40 s. For faster flow conditions, 11.7, 14.0, and 20.1 s^{-1}, the characteristic time is shorter, ~ 15 s. Finally, all bands combine to produce homogeneous, fast flow along the vorticity axis. This steady-state velocity is now ~ 50 times that expected for an unbanded, Newtonian flow. While detailed observation of this transient vorticity dynamics is described here for the SLE3S/SLS WLM solutions (3.5% salt), the same 4-step process with transient vorticity structuring is observed for SLE3S/SLS (1.9% salt) and SLE1S WLM solutions (cf. Appendix F).

The characteristic time scales of the flow at all shear rate conditions are displayed in Figure 3.9. Three distinct times, t_{decel}, t_{fluc}, and t_{ss}, report the times at which deceleration, fluctuation, and steady-state transition take place, respectively. The deceleration transition time, t_{decel}, is taken as the time at which the local maximum <v> is reached from flow start up. The fluctuation transition, t_{fluc}, is defined as the time at which no consecutive decrease in velocity is measured for Δt of 0.3 s. The steady-state

transition times, t_{ss}, is calculated by taking the time at which 95% of the average steady state velocity is reached. Durations of the fluctuations are the largest for 8.4 and 10.0 s^{-1} shear rate cases. Overall, characteristic times for all three regimes decrease with applied shear rates for shear rate ranges of 8.4 to 14.0 s^{-1}. However, similar time scales are observed for 14.0 and 20.1 s^{-1}; these conditions also exhibit the shortest time scales for all three regimes. Relative to the overall time required to achieve steady-state banding, the duration of the acceleration, deceleration, and fluctuating regimes is small.

3.5 Discussion

Steady-state velocity profiles of wormlike micelle solutions in rectangular channel flow display gradient shear banding at flow conditions consistent with the region of stress plateau as measured by cone-and-plate rheometry. Under these conditions, steady-state profiles exhibit thin, near-wall, regions (< 2 μm) of high shear rate, high velocity flow. In these regions, the maximum velocity is ~ 50 times higher than the value predicted by extrapolating the parabolic flow observed in the bulk to the wall, corresponding to local, near-wall shear rates that are an equivalent factor larger than the nominally applied wall shear rate. Such a thin, near-wall region of high velocity flow coexisting with a parabolic inner flow is consistent with a number of literature studies[13,26,28,29].

At applied shear rates above the shear banding condition, steady-state velocities within the near wall region increase linearly with the applied rate (Figure 3.3b). The linear increase in the near wall velocity – an apparent slip velocity – is consistent with a shear band whose interface is closer to the wall than the 2 μm point of measurement. This bound on the band thickness is further refined to be less than < 250 nm based on the near-flat velocity profiles within 4 μm of wall, as measured by high resolution

microscopy (c.f. Figure 3.3c). The thin width (< 250 nm) of the high shear rate band implies that the high shear rate region of the flow curve appears only at shear rates greater than ~10^4 s^{-1}. The bounds on band dimension also imply that the viscosity within the band is low – no greater than 0.07 Pa s – and a factor of ~ 700 less than the zero-shear viscosity of the WLM as measured by cone and plate rheometry.

Prior to steady state, transient flows with complex spatiotemporal behavior are observed in the near wall region (< 10 μm) for shear banding conditions. At a distance only ~ 1-2 μm from the shear band interface, strong variations in the time dependent velocity are observed along the vorticity direction. We describe the transient dynamics as a four-step process involving: (1) global acceleration of the flow to about half of the steady-state velocity at all points along the vorticity axis, (2) global deceleration to about half of the magnitude of the previously accelerated velocity, (3) banded regions of velocities varying along the vorticity axis, (4) attainment of the final, fast velocity characteristic of steady-state. In the third stage, the bands of varying velocity along the vorticity axis are spatially chaotic; the number of bands is highly variable. The duration of this third, fluctuation regime ranges from 10 to 40 s, with shorter time scales for faster flows.

The spatiotemporal dynamics of gradient shear banding reported in this paper are distinct from vorticity banding, as generated in Taylor-Couette geometries by viscoelastic instability triggered by the curved streamlines of that flow[10,22]. Indeed, the inhomogeneous flows observed here are not vorticity bands, because they do not extend more than 10 μm in the wall normal direction of the flow. Above this dimensions, the flow (in the low rate band) is steady and homogeneous.

However, we argue a connection between the vorticity structuring of gradient bands observed here and recent high rate/stress experimental[14] and theoretical[16] studies of wormlike micelles in plane Poiseuille flow. Nghe et al. and Fielding et al. find – by both theory and experiment – that the interface between high and low shear rate bands is unstable; this interface supports velocity fluctuations along the vorticity axis at steady-state[14,16]. These interfacial instabilities are induced by a jump in the second normal stress difference across the interface. This imbalance generates secondary flows. The theoretical analysis is for the case of a diffusive Johnson-Segalman fluid, a material with a viscoelastic constitutive response that generates a non-monotonic stress vs. shear rate curve and a high shear stress region that is Newtonian[14]. The model also predicts non-zero first and second normal stress differences[36].

There are similarities and differences between the observations of Nghe et al. and this work. First, Nghe et al. report that the wavelength of the interfacial undulations (along the vorticity direction) ranges from 1 to 2 times the height of the channel (in the gradient direction). In our case, the full height of the channel is 800 μm; the corresponding wavelength of the vorticity fluctuation would be 800 – 1600 μm in length if there were full correspondence with Nghe et al. The widths of the transient bands reported in this work range from 100 to 500 μm, with a maximum observable size of ~ 600 μm as set by our observation window along the vorticity axis.

Second, the amplitude of the modulations at the shear band interface found by Nghe et al. ranges from 0.5 - 1% of the channel height. This is ~ 4 to 8 μm for the geometry studied in this work, which is consistent with the gradient height at which we observe the vorticity structuring. This correspondence suggests that the fluctuation

dynamics measured here could be an interfacial instability similar to that described by Nghe et al. and Fielding et al.

Notwithstanding these commonalities, there are a number of interesting differences in the channel flow results of Nghe et al. and this work. First, the fluid studied by Nghe et al. displays a stress plateau ~ 100 Pa that persists from a low-rate transition of 5 s^{-1} to a high-rate transition of ~ 100 s^{-1}. The fluid they studied is a 0.3M CTAB solution in 0.405M sodium nitrate solution. In our fluid (1.2M SLE3S and 1.0M SLS solution in 0.7M NaCl solution), the stress plateau is at ~ 180 Pa. However, the shear rate range of the stress plateau is very different in our fluid, with a low rate critical condition of 4.5 s^{-1} and a high rate transition estimated to be at greater than 10^4 s^{-1}. The vorticity structuring observed in Nghe et al. is for flow at a wall shear stress greater than the stress plateau (30% greater than that plateau), and in regions for which the measured slip length is small – a mean value of 0.5 ± 0.9 μm is reported. On the other hand, the vorticity structuring here is observed within the region for which shear bands coexist, and for which the extracted, average slip length is much larger: 144 ± 14 μm. (The slip length is extracted from the slope of the plot in Figure 3.3b.)

Another key difference between the present report and the work of Ref. 14 is that the vorticity-axis velocity fluctuations here are only observed transiently; the flow is homogeneous along the vorticity direction at steady-state. The velocity modulations reported in Ref. 14 occur at the shear band interface, again for wall shear stresses that are 30% above that of the shear-banding onset. The applied shear rate in their case is estimated to be ~ 25 times the critical shear rate (5 s^{-1}) based on the flow curve reported in Ref. 12. In comparison, the equivalent wall shear rate ranges probed in this work are

at most 4 times the onset rate for shear banding. This comparison suggests two conclusions: (i) that vorticity structuring is not solely a high shear rate phenomena; it can occur at applied shear rates that are only just above the onset condition; (ii) that in such cases of low rate vorticity structuring the fluctuations are only transient. That is, there is a mechanism at these lower shear rates by which vorticity disturbances initiated at the band interface are damped, and do not persist at steady state.

Therefore, the absence of steady-state vorticity structures in the present case could stem from a subcritical instability in the shear rate region studied. That is, fluctuations at the near-critical shear rate could dampen over time, leading to a secondary flow that is unsustainable at steady-state. Transient vorticity dynamics observed in this work could consequently be understood as the early transient effect of the interfacial instability of gradient shear bands.

The above comparison is a purely continuum description of the phenomenon, with a mechanism for transient instability driven by the second normal stress differences at the interface, as described by Fielding[16]. The question arises as to what behavior of the micellar microstructure is generating these changes in continuum rheological properties. Ideas discussed in the literature include the development of a concentration gradient between the bands (demixing) or the generation of an aligned state of the WLM solution (a flow-induced isotropic-nematic transition). The thin bands observed here suggest that the solution in the high shear band has a very low viscosity – no greater than 0.07 Pa s, which corresponds to a high to low shear phase viscosity ratio of 0.001. In comparison, Nghe et al. report a viscosity ratio of ~ 0.05 between the high and low shear phases[14]. One mechanism by which these low viscosities could be produced could be through the

rejection of surfactants from the near wall region. The channel flow geometry establishes a shear stress relation that varies linearly across the cell, with maximum shear stress magnitude at the walls. We speculate that large wall stresses and an inhomogeneous stress fields could cause surfactants to migrate towards the center of the channel, forming a low surfactant concentration region with significantly reduced viscosities. The surfactant migration would take time and be a complex process; therefore, it could contribute to the chaotic spatiotemporal dynamics in the velocity observed in the near-wall region of the flow.

3.6 Conclusion

We have carried out velocity profile measurements of wormlike micelle solutions in rectangular channel geometry. Using confocal microscopy and particle image velocimetry, we have carefully tracked and characterized transient variations in the flow rate that are non-uniform along the vorticity direction for shear-banded flows. The transient process has four steps: flow acceleration, deceleration, fluctuations along the vorticity direction, and steady state. The intermediate structuring of the flow is found at points up to 10 μm in the gradient direction and its characteristic time scale increases for near wall and low shear rate conditions. The observed phenomenon is distinct from vorticity banding generated by viscoelastic instabilities in curved streamlines, but could be explained by the presence of interfacial instabilities at the shear band interface. The vorticity structuring of gradient shear bands observed here occurs at applied wall shear rates that are as low as four times the onset condition for shear banding.

3.7 Figures

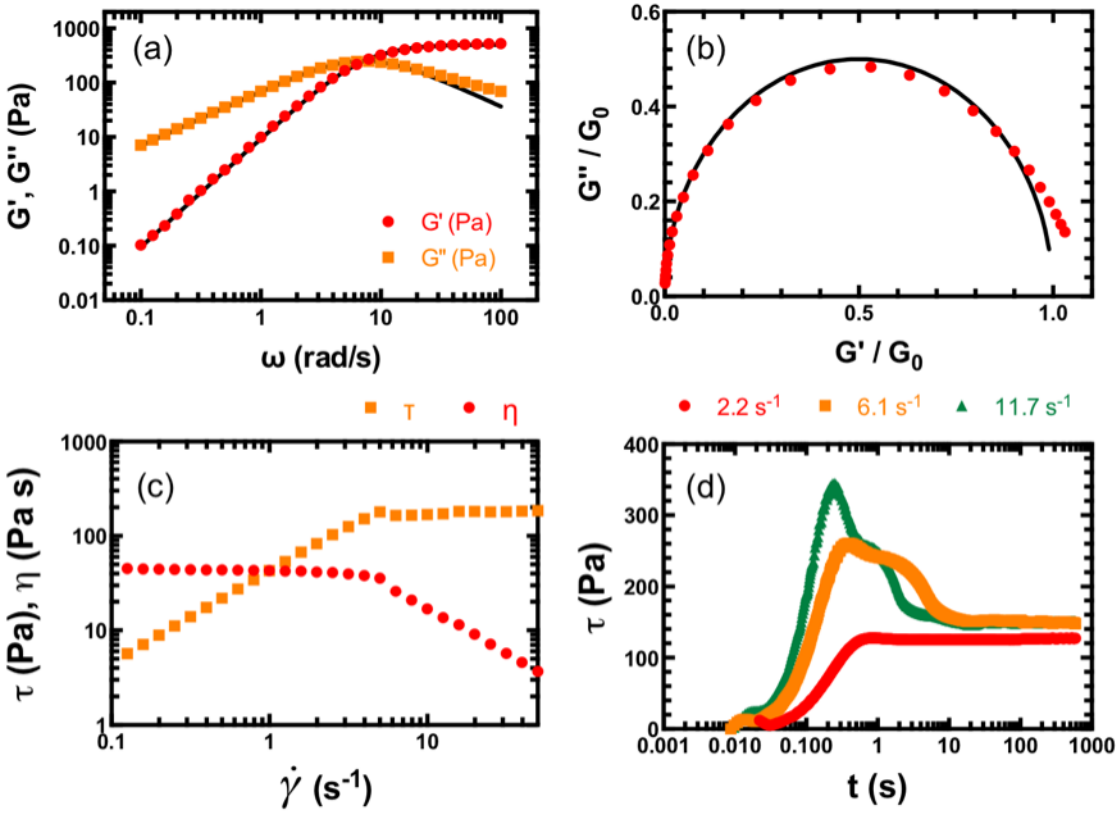

Figure 3-1. Linear viscoelasticity, steady shear rheology, and transient rheology measurements of SLE3S (42 wt.%)/SLS (24 wt.%) WLM solutions with 3.5 wt.% NaCl.

(a) Storage (G') and loss (G'') moduli are plotted as a function of angular frequency, ω, for oscillatory frequency sweep at γ = 1 and T = 21.5°C. The solid black line corresponds to a single-mode Maxwell model fit with G_0 = 510 Pa and λ_M = 0.14 s. (b) Cole-Cole plot of the oscillatory frequency sweep results shows a Maxwellian behavior. The solid line is the single-mode Maxwell model fit. (c) Steady shear stress and steady shear viscosity of WLM solutions at 21.5°C. The plateau in the steady shear stress is observed at a shear rate of 4.5 s^{-1}. (d) Transient shear stress responses to start-up flow experiments at three shear rates (2.2, 6.1, and 11.7 s^{-1}).

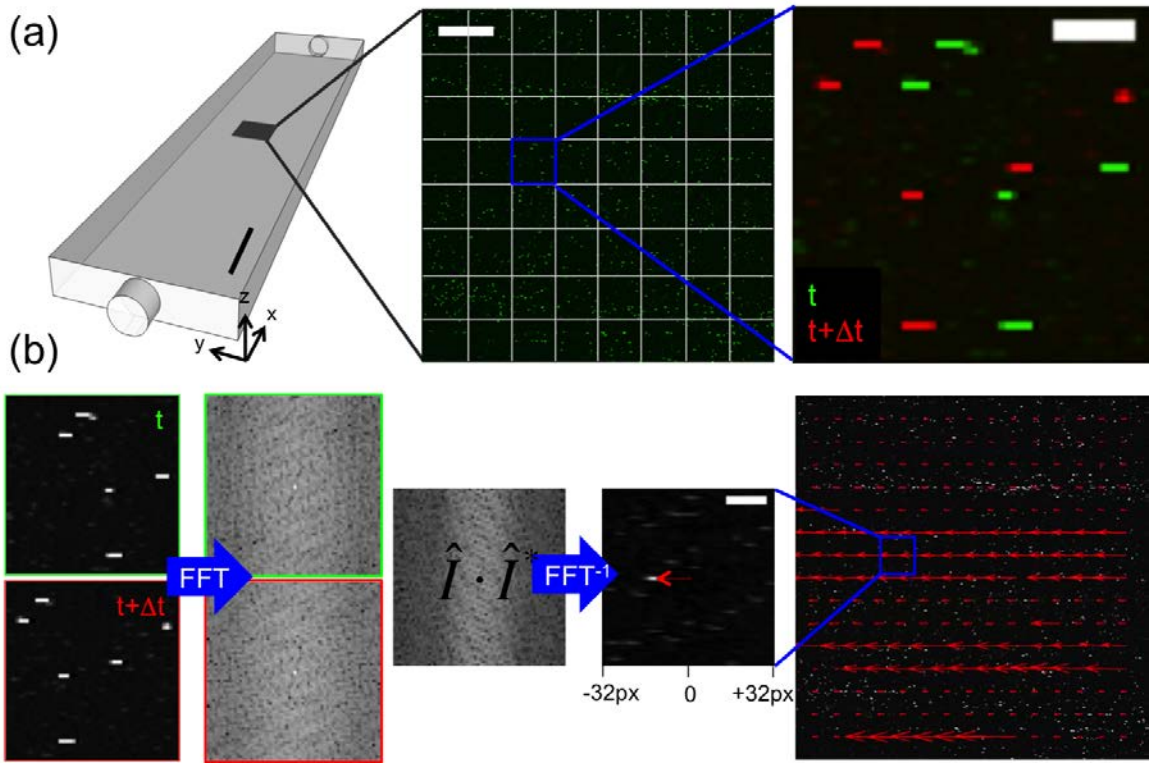

Figure 3-2. Particle image velocimetry (PIV) in the rectilinear channel flow.

(a) The three images depict the flow at different scales: 1 mm, 100 μm and 15 μm scale bars from left to right. All confocal micrographs (a, middle and right panel, b, left and right panels) are of the flow, imaged at the center of the xy (flow-vorticity) plane. (a, middle panel) For PIV analysis, each confocal image frame is divided into interrogation areas. (a, right panel) A particular interrogation area is shown at two time frames (one green and one red), with $\Delta t = 0.067$ s. (b) Steps used for PIV cross-correlation are shown. (b, left panel) Fast Fourier Transforms (FFT) of the images taken at two time frames are calculated. (b, middle panel) The intensity of the first image FFT is multiplied by the conjugate of the second image FFT. Then, the inverse FFT of the result yields the cross-correlation matrix. The location of the maximum intensity reports the direction and magnitude of the vector describing the movement of the particle patterns on the images. The scale bar here is 15 pixels, with a pixel resolution of 1.23 μm/pixel. (b, right panel) From the correlation matrix, the local velocities within the interrogation area can be calculated from the frame rate (0.067 s). The process is repeated until the entire vector field is derived for the image series.

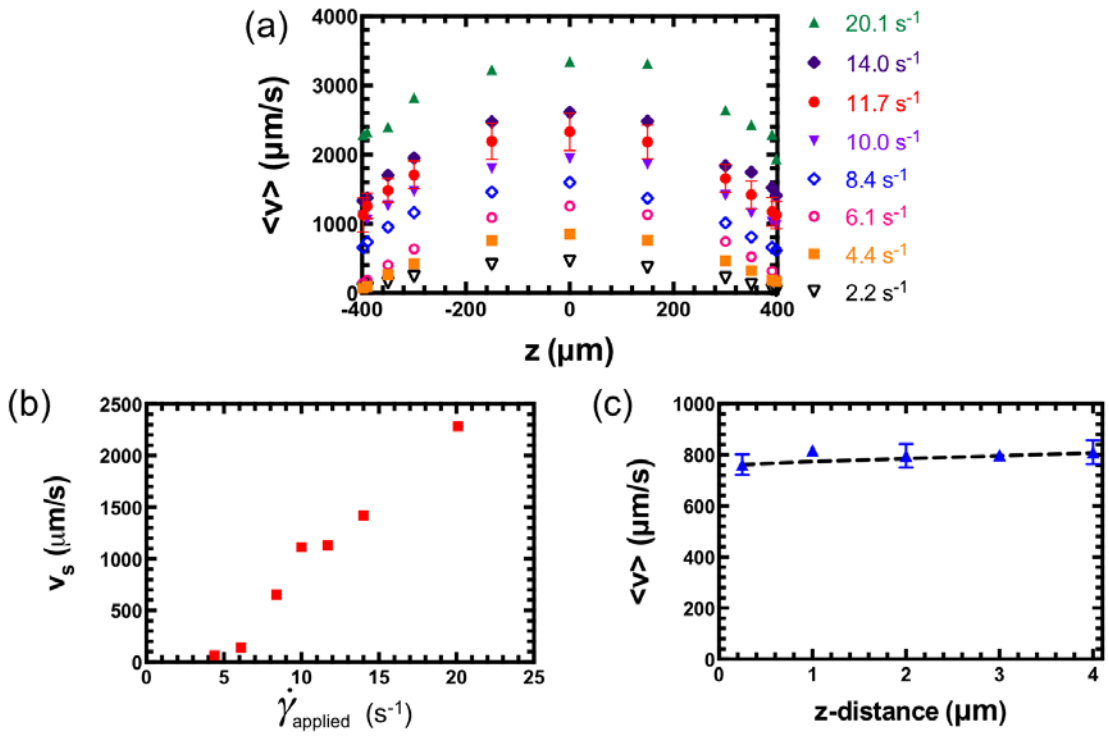

Figure 3-3. Steady-state velocity profiles and near-wall velocities for the WLM solution.

(a) Velocity profiles are parabolic with nearly zero velocities at the wall for shear rates below 6.1 s^{-1}. Above shear rates of 8.4 s^{-1}, deviations from the parabolic behavior are observed at the wall; increasingly high velocities are measured 2 μm from the wall as shear rate is increased. Error bars plotted for the 11.7 s^{-1} data are standard deviations of the mean of 3 data sets. (b) The near-wall velocities at 2 μm from the wall (bottom cover slip) are plotted as a function of applied shear rate. An increase in these velocities is measured above a shear rate of 6.1 s^{-1}. All experiments are carried out for SLE3S (42 wt.%)/SLS (24 wt.%) WLM solutions with 3.5 wt.% NaCl solution at 21.5°C. (c) WLM near-wall measurements are reported at 11.7 s^{-1}. Velocity measurements of WLM solutions within this small region show a near-flat velocity profile. The dotted line is an estimate for parabolic flow at 11.7 s^{-1} shear rate flow in an 800 μm channel, added to a constant near-wall velocity of 750 μm/s. Error bars indicate standard deviations of the mean.

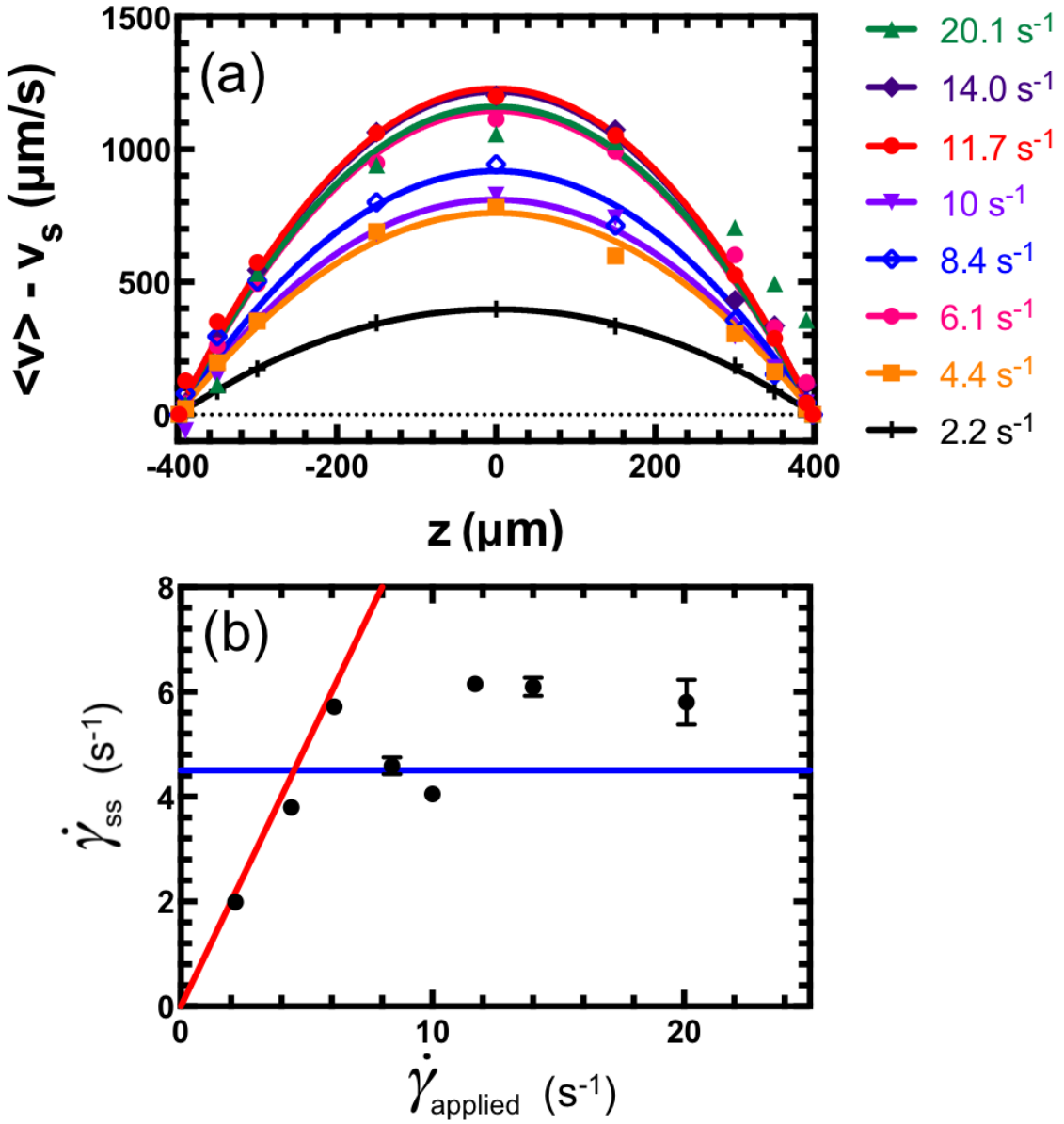

Figure 3-4. Shear rates of the low rate band.

(a) Velocity profiles from Figure 3a are adjusted by subtracting the near-wall velocities across the entire profile. Parabolic fits (solid lines) show good performance at all shear rate conditions. (b) Steady-state shear rates of the flow are extracted from the analysis of (a) and plotted against the nominal shear rate applied to the whole flow. The red line shows $\dot{\gamma}_{ss} = \dot{\gamma}_{nom}$. The blue line shows the critical shear banding condition, $\dot{\gamma}_{ss} = 4.5\ s^{-1}$. At shear rates up to 6.1 s^{-1}, data approximately follow the red line. At shear rates above 6.1 s^{-1}, data fluctuate about the blue line. Error bars are calculated from the standard error of the fit in (a).

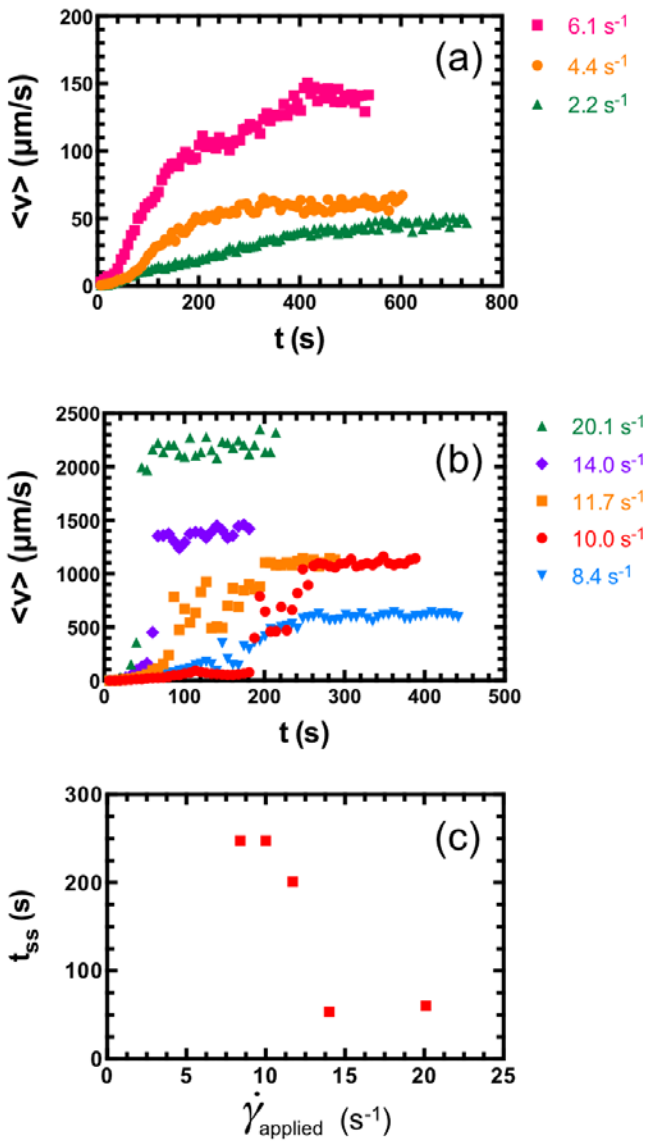

Figure 3-5. The effect of applied shear rate on the vorticity-averaged near-wall velocity in the flow direction.

All measurements are taken at 2 μm from the wall. (a) At shear rates 2.2, 4.4, and 6.1 s^{-1}, transient velocity measurements show a monotonic increase in average velocities at this wall normal position. The large time constant (~ 500 s) for the steady-state flow is observed for the lowest shear rate value (2.2 s^{-1}) and is caused by the high viscosities of the fluid at low shear rates. (b) At shear rates 8.4, 10, and 11.7, large fluctuations in the average velocity are shown at intermediate times; at long times the near-wall <v> is large, consistent with the steady-state measurements of Figure 3. At higher shear rates, 14.0, and 20.1 s^{-1}, flow rapidly transitions to steady-state. (c) Time to reach steady-state (t_{ss}) extracted from (b) by taking the first time point at which <v> is 95% of its steady-state value.

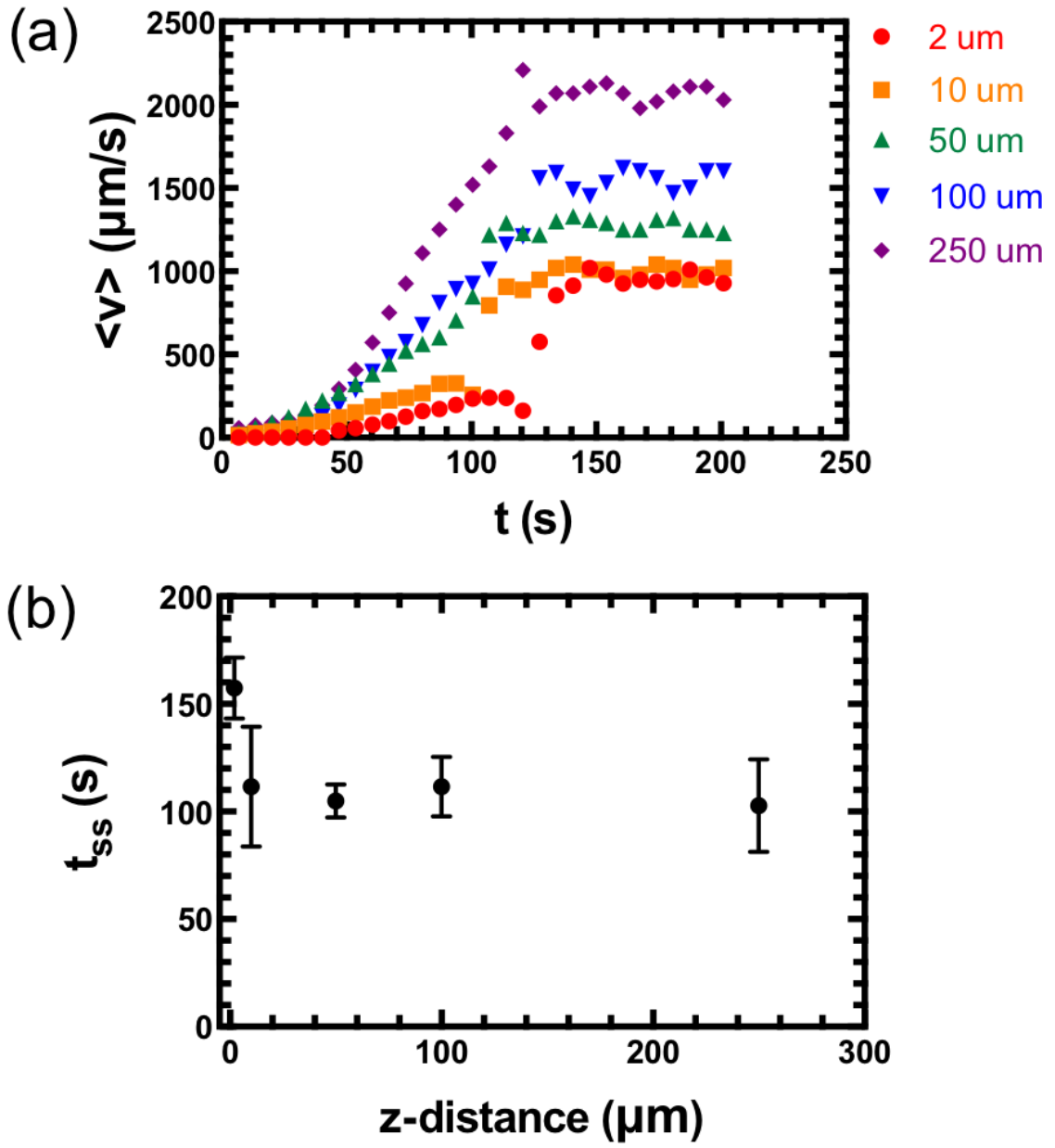

Figure 3-6. The effect of wall-normal distance (z-distance) on the transient velocity measurements.

(a) Transient average velocities are measured at wall normal (gradient) distances of 2, 10, 50, 100, and 250 μm at an applied shear rate of 11.7 s^{-1}. (b) Time to reach steady state (t_{ss}) is obtained from (a) by taking the first time point at which the <v> reaches 95% of its plateau value for all z-distance conditions.

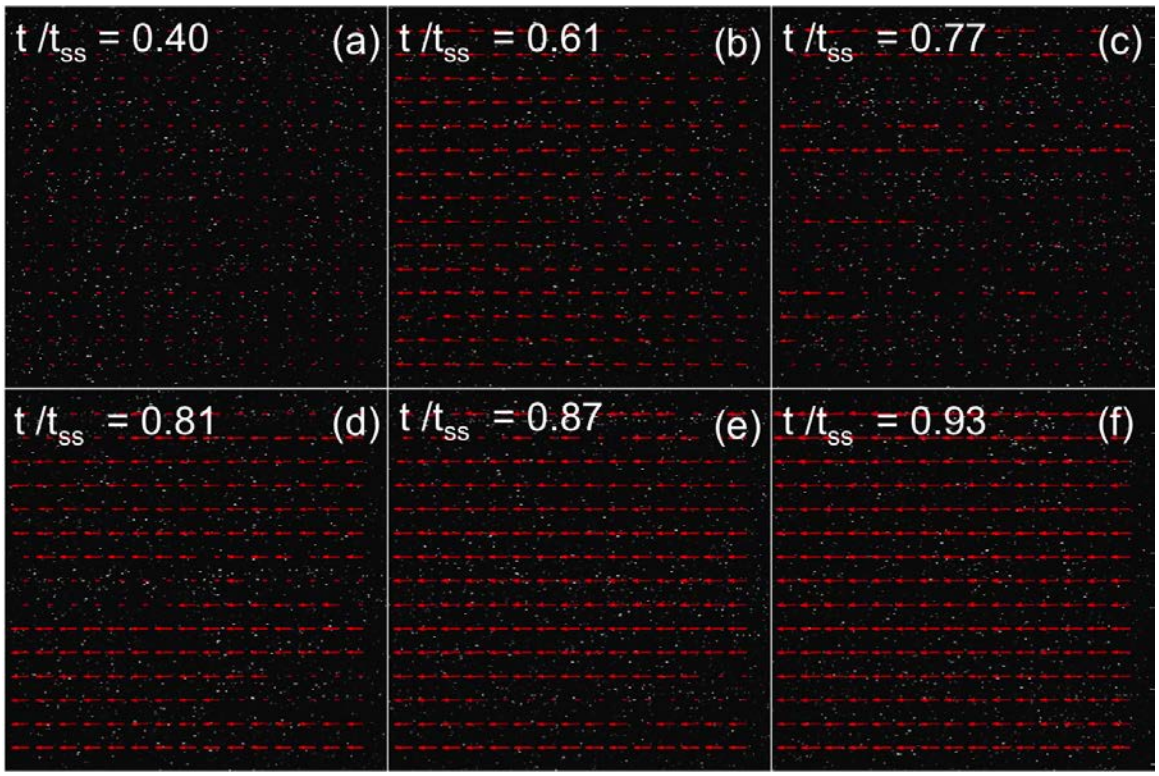

Figure 3-7. Transient fluctuations in the velocity along the vorticity axis at a gradient height of 2 μm.

Velocity fields are shown for a flow (8.4 s^{-1}) observed at the center of the flow-vorticity plane at 2 μm from the bottom wall at 6 distinct time points, t/t_{ss} (0.40, 0.61, 0.77, 0.81, 0.87, and 0.93). (a-b) Flow velocity increases over time as observed by increasing vector lengths. (c) Thin bands flowing at fast velocities are observed along the vorticity direction. (d-e) Fast bands grow and merge until very thin bands of the slow velocity regions remain. (f) Homogeneous velocity vector field is observed at steady-state, where all the particles are traveling at the large velocity observed at 2 μm from the wall.

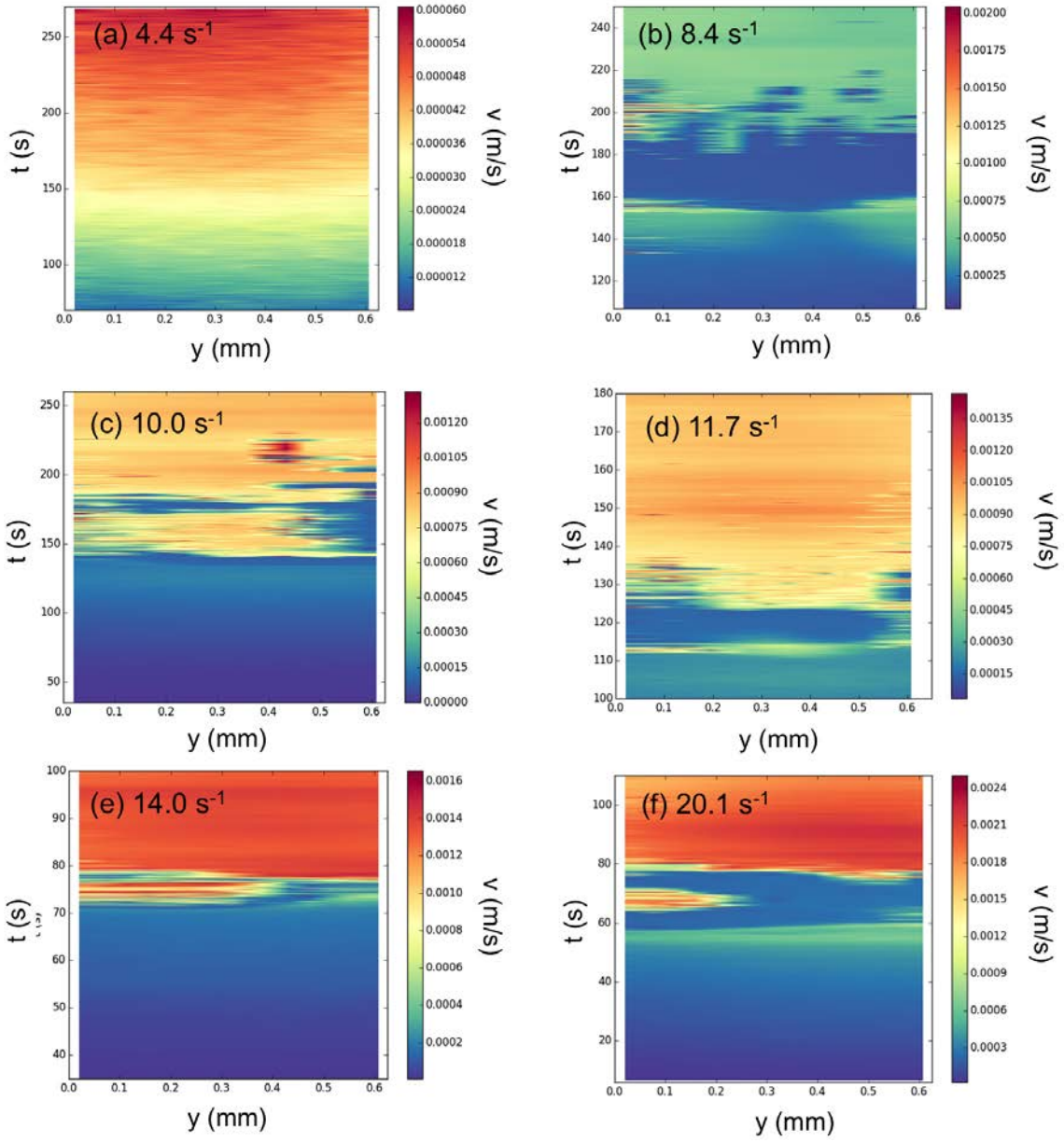

Figure 3-8. Space-time plots of flows below and above shear banding conditions.

(a) Space-time plot of the flow at 4.4 s^{-1}, prior to shear banding, is measured along the vorticity direction over time. (b) Flow profile along the vorticity direction is measured over time for 8.4 s^{-1} shear rate condition. (c-f) Similar 4-step sequence is observed for the flow under 10.0, 11.7, 14.0, and 20.1 s^{-1} conditions. The fluctuating step, however, occurs for a shorter duration (~ 15 s) as compared to the slower shear rate conditions in (b and c) (~ 50 s).

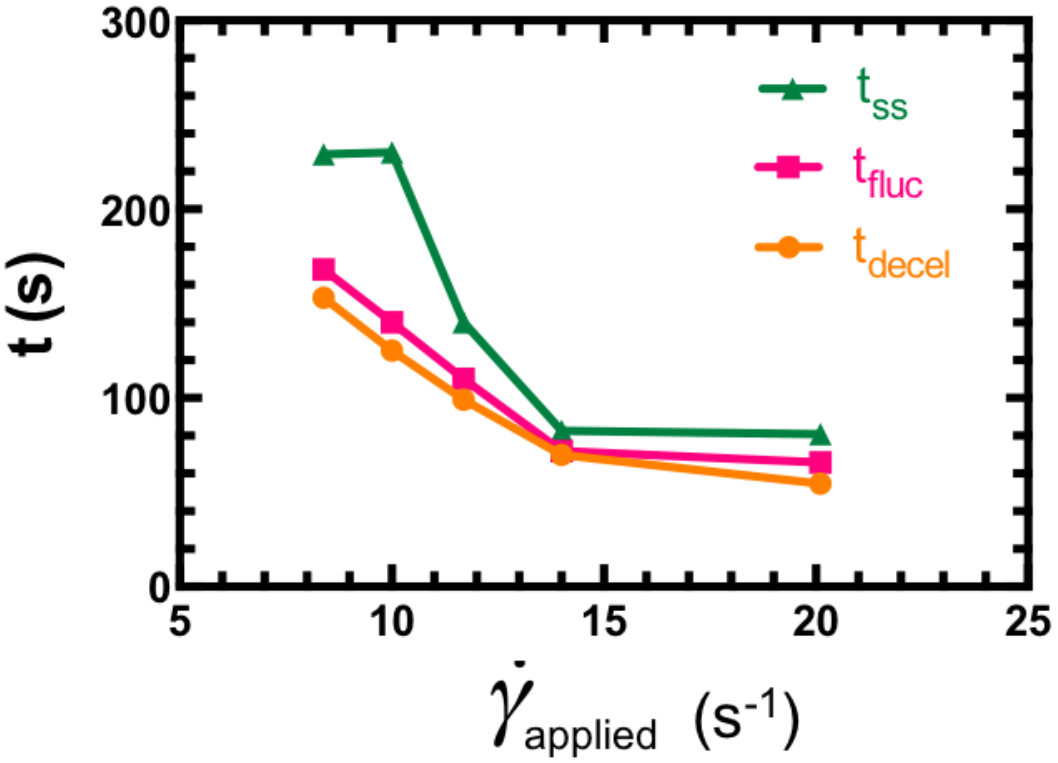

Figure 3-9. Characteristic transition times for deceleration, fluctuation and steady-state.

Transition times for deceleration (t_{decel}), fluctuations (t_{fluc}), and steady-state (t_{ss}) are calculated and plotted for shear rates of 8.4, 10.0, 11.7, 14.0, and 20.1 s^{-1}. All curves lie close together for the range of shear rates reported, with the largest variation from the duration of the fluctuation (t_{fluc}-t_{ss}) for 8.4 and 10.0 s^{-1} conditions.

3.8 References

1. Cates, M. E. & Candau, S. J. Statics and dynamics of worm-like surfactant micelles. *J. Phys. Condens. Matter* **2,** 6869–6892 (1990).

2. Dreiss, C. Wormlike micelles: where do we stand? Recent developments, linear rheology and scattering techniques. *Soft Matter* **3,** 956 (2007).

3. Rogers, S. A., Calabrese, M. A. & Wagner, N. J. Rheology of branched wormlike micelles. *Curr. Opin. Colloid Interface Sci.* **19,** 530–535 (2014).

4. Cates, M. E. Nonlinear viscoelasticity of wormlike micelles (and other reversibly breakable polymers). *J. Phys. Chem.* **94,** 371–375 (1990).

5. Cates, M. E. & Fielding, S. M. Rheology of giant micelles. *Adv. Phys.* **55,** 799–879 (2006).

6. Fielding, S. M. Complex dynamics of shear banded flows. *Soft Matter* **3,** 1262 (2007).

7. Divoux, T., Fardin, M. A., Manneville, S. & Lerouge, S. Shear Banding of Complex Fluids. 16 (2015). at <http://arxiv.org/abs/1503.04130>

8. Spenley, N. A., Cates, M. E. & McLeish, T. C. B. Nonlinear rheology of wormlike micelles. *Phys. Rev. Lett.* **71,** 939–942 (1993).

9. Dhont, J. K. G. & Briels, W. J. Gradient and vorticity banding. *Rheol. Acta* **47,** 257–281 (2008).

10. Fielding, S. M. Vorticity structuring and velocity rolls triggered by gradient shear bands. *Phys. Rev. E* **76,** 016311 (2007).

11. Méndez-Sánchez, A. F. *et al.* Particle image velocimetry of the unstable capillary flow of a micellar solution. *J. Rheol. (N. Y. N. Y).* **47,** 1455 (2003).

12. Nghe, P., Degré, G., Tabeling, P. & Ajdari, A. High shear rheology of shear banding fluids in microchannels. *Appl. Phys. Lett.* **93,** 204102 (2008).

13. Masselon, C., Colin, A. & Olmsted, P. D. Influence of boundary conditions and confinement on nonlocal effects in flows of wormlike micellar systems. *Phys. Rev. E* **81,** 021502 (2010).

14. Nghe, P., Fielding, S. M., Tabeling, P. & Ajdari, A. Interfacially Driven Instability in the Microchannel Flow of a Shear-Banding Fluid. *Phys. Rev. Lett.* **104,** 248303 (2010).

15. Lerouge, S., Argentina, M. & Decruppe, J. P. Interface Instability in Shear-Banding Flow. *Phys. Rev. Lett.* **96,** 088301 (2006).

16. Fielding, S. M. & Wilson, H. J. Shear banding and interfacial instability in planar Poiseuille flow. *J. Nonnewton. Fluid Mech.* **165,** 196–202 (2010).

17. Holmes, W. M., López-González, M. R. & Callaghan, P. T. Fluctuations in shear-banded flow seen by NMR velocimetry. *Europhys. Lett.* **64,** 274–280 (2003).

18. López-González, M. R., Holmes, W. M., Callaghan, P. T. & Photinos, P. J. Shear Banding Fluctuations and Nematic Order in Wormlike Micelles. *Phys. Rev. Lett.* **93,** 268302 (2004).

19. Ovarlez, G., Rodts, S., Chateau, X. & Coussot, P. Phenomenology and physical origin of shear localization and shear banding in complex fluids. *Rheol. Acta* **48,** 831–844 (2009).

20. Zhao, Y., Cheung, P. & Shen, A. Q. Microfluidic flows of wormlike micellar solutions. *Adv. Colloid Interface Sci.* **211,** 34–46 (2014).

21. Bécu, L., Manneville, S. & Colin, A. Spatiotemporal Dynamics of Wormlike Micelles under Shear. *Phys. Rev. Lett.* **93,** 018301 (2004).

22. Fardin, M.-A. & Lerouge, S. Instabilities in wormlike micelle systems. From shear-banding to elastic turbulence. *Eur. Phys. J. E. Soft Matter* **35,** 91 (2012).

23. Feindel, K. W. & Callaghan, P. T. Anomalous shear banding: multidimensional dynamics under fluctuating slip conditions. *Rheol. Acta* **49,** 1003–1013 (2010).

24. Fardin, M. A. *et al.* Shear-banding in surfactant wormlike micelles: elastic instabilities and wall slip. *Soft Matter* **8,** 2535 (2012).

25. Salmon, J.-B., Colin, A., Manneville, S. & Molino, F. Velocity profiles in shear-banding wormlike micelles. *Phys. Rev. Lett.* **90,** 228303 (2003).

26. Callaghan, P. T., Cates, M. E., Rofe, C. J. & Smeulders, J. B. A. F. A Study of the 'Spurt Effect' in Wormlike Micelles Using Nuclear Magnetic Resonance Microscopy. *J. Phys. II* **6,** 375–393 (1996).

27. Mair, R. W. Shear flow of wormlike micelles in pipe and cylindrical Couette geometries as studied by nuclear magnetic resonance microscopy. *J. Rheol. (N. Y. N. Y).* **41,** 901 (1997).

28. Britton, M. M. & Callaghan, P. T. Shear banding instability in wormlike micellar solutions. *Eur. Phys. J. B* **7,** 237–249 (1999).

29. Ober, T. J., Soulages, J. & McKinley, G. H. Spatially resolved quantitative rheo-optics of complex fluids in a microfluidic device. *J. Rheol. (N. Y. N. Y).* **55,** 1127 (2011).

30. López-Barrón, C. R., Gurnon, A. K., Eberle, A. P. R., Porcar, L. & Wagner, N. J. Microstructural evolution of a model, shear-banding micellar solution during shear startup and cessation. *Phys. Rev. E* **89,** 042301 (2014).

31. Singh, O. *Introduction To Mechanical Engineering:Thermodynamics, Mechanics And Strength Of Material*. (New Age International, 2006).

32. Moorcroft, R. L. & Fielding, S. M. Shear banding in time-dependent flows of polymers and wormlike micelles. *J. Rheol. (N. Y. N. Y).* **58,** 103 (2014).

33. Turner, M. S. & Cates, M. E. Linear viscoelasticity of living polymers: a quantitative probe of chemical relaxation times. *Langmuir* **7,** 1590–1594 (1991).

34. Thielicke, W. The flapping flight of birds : Analysis and application. (2014).

35. Pizer, S. M. *et al.* Adaptive histogram equalization and its variations. *Comput. Vision, Graph. Image Process.* **39,** 355–368 (1987).

36. Fielding, S. M. Viscoelastic Taylor-Couette Instability of Shear Banded Flow. *Phys. Rev. Lett.* **104,** 198303 (2010).

Chapter 4 Colloidal gelation in nanoliter droplets[**]

4.1 Abstract

We report a method to produce gels of micron-scale colloids in oil-in-water droplets of submillimeter dimension. Monodisperse droplets containing a dispersed phase of sterically-stabilized poly(methyl methacrylate) (PMMA) colloids in a mixture of cyclohexyl bromide and decalin with added salt are produced using a two-phase coflow liquid microfluidic device. The assemblies are confined in droplets of size ~ 200 μm in diameter (~ 5 nanoliters), and are comprised of approximately 100,000 colloids. Because the surfactant-stabilized oil/water interface is semi-permeable to the added salt – tetrabutylammonium bromide, TBAB – the pair potential between the PMMA colloids changes with time, thereby leading to a range of self-assembled microstructures. The sterically-stabilized colloids first self-assemble into a colloidal crystal as the salt in the droplet oil phase extracts into the continuous aqueous phase. This partitioning increases the Debye length of the oil phase, which in turn increases the range of the repulsion between the colloids. However, surprisingly, we find that a phase transition from crystal

[**] This chapter is in preparation for publication by Y. Kim, M.E. Szakasits, W. Zhang & M.J. Solomon.

to gel also takes place within droplets at longer durations (~ 2 weeks). The transition times are dependent upon the droplet interfacial accessibility of the outer aqueous phase (controlled by the droplet cluster sizes) and the size of the individual droplets. We use confocal microscopy to image the kinetics of the assembly process and the three-dimensional assembly structures. The impetus for gelation is hypothesized to be through confined boundary effects with increased short-range attraction between colloids within the droplets. By demonstrating the scope for producing colloidal gel assemblies from as few as ~100,000 colloids, the method is well adapted for efficient production of droplets with possible elastic mechanical properties.

4.2 Introduction

Particle microstructures produced by colloidal self-assembly have potential applications in photonics, optics, electronics, and sensing[1]. Diverse structures – including colloidal gels, crystals, and dense, amorphous glasses – have been formed from both self-assembly[2,3] and directed-assembly methods[4] in bulk. However, large-scale uniformity of microstructures self-assembled in bulk can be hard to achieve[1]. Recently, small-scale assembly methods have been developed, which potentially address this challenge, as well as allowing interesting unit cells to be produced from a relatively small number of colloids (millions). Examples include colloidal crystal arrays in fluid droplets[5,6], in micro-wedges[7–9], or in small regions affected by electric fields[10–12]. Both experiments and simulations of anisotropic colloidal assembly in confinement have also been of interest[9,13].

Self-assembly in droplets is appealing because it compartmentalizes colloids on the mesoscopic scale ~ 100 μm. On this scale, self-assembly conditions such as solvency and salinity can be controlled by the high surface area and semi-permeability of the droplet interface. Colloidal structure and dynamics can, also, be interrogated at the single-particle level. Individual droplets can potentially be transported and manipulated to produce mesoscale assemblies of droplets, each with a particular colloidal structure contained within it[14]. To date, the droplet-based assemblies have been produced with droplet sizes of 100 nm up to 1.3 mm[15] with the size of colloids confined in them varying from 5 nm to about 2 μm[15,16]. Also, the photonics applications of these droplets have been the main focus[17–20].

Monodisperse oil-in-water and water-in-oil emulsion droplets can be formed microfluidically[21]. The method is potentially inexpensive, scalable, and has high production rates[5]. Upon the addition of emulsifiers or particles, microfluidically produced droplets are highly stable – with lifetime of over a month. Additionally, the size of the droplets can be manipulated by varying the inner capillary tip size, inner and outer fluid flow rates, and the fluid viscosities in the microfluidic device[22]. The typical size of droplets produced by this method is 1 – 200 μm in diameter. A droplet with a 200 μm diameter would fit ~ 2 x 10^6 micron-scale colloids at close packing, as compared to ~ 5 x 10^{10} colloids for 100 μl bulk assembly at close packing.

For practical applications of the droplets, an efficient method to introduce intrinsic (volumetric) mechanical properties to the droplet systems is desirable[5]. Droplets themselves are elastic; they resist deformation from their equilibrium spherical shape. However, if the volume of fluid in the droplet could generate a viscoelastic response, or be comprised of a yield stress fluid, then additional control of mechanical properties would become available. Colloidal particular gels are excellent candidates for generating such rheological control[23]. The fractal, disordered gel structures possess solid-like mechanical properties, such as yield stresses[3]. They are widely applicable in materials ranging from foods, consumer products, ceramics, membranes, and tissue scaffolds[24], and are produced on an industrial scale[25]. While the confinement effects on colloidal gelation has been investigated in a micro-wedge system[7], colloidal gels within droplets have not been produced.

Droplet gels can also be generated by polymerization[26,27]. Polymer gels are formed through chemical bonding[28]. However, the difference between colloidal particulate gels and polymer gels is that the cross-linked polymer gel structures are permanent, with the exception of some biopolymer gels; whereas colloidal gels can be broken and reformed[29]. Therefore, with colloidal gel systems, the mechanical properties of the droplet can be reversibly varied based on their internal arrangements.

Colloidal gel structures are sensitive to shear[24]; therefore, the production method should load a dispersion of colloids into the droplets and gelation should be induced in the droplets post-production. Several different mass transfer mechanisms have been used in droplet systems to generate self-assemblies of crystals, shells, and clusters in droplets; these methods can conceivably be extended to produce colloidal gel assemblies.

Colloidal crystals have been formed from dense packing of colloids in droplets (i.e. supraparticles or photonic balls) through evaporation and osmotic pressure control[5,16,20,30]. Recently, Nijs et al. reported icosahedral cluster assemblies obtained from nanometer and micrometer colloids through spherical confinement of the colloids and further evaporation of the dispersed solvent[16]. The structures found depended on the size of the clusters: clusters with icosahedral symmetry were formed up to 1000 colloids and the structure transitioned from rhombicosidodecahedron to FCC between 25,000 to 90,000 colloids.

In double emulsion droplet systems, the semi-permeability of the membrane allowed for diffusion of water, in the presence of an osmotic pressure gradient, leading to changes in the particle volume fraction within the droplets as they shrink[17,18]. Shirk et al.

generated spherical colloidal crystals with colloidal volume fractions up to 0.68 through diffusion of water out of the inner droplet[18]. Kim et al. dynamically controlled the iridescence of the photonic droplets by subjecting the droplets to varying differentials in osmotic pressure [17].

In addition to solvent flow driven by differences in osmotic pressure, the semi-permeability of the droplet interface also allowed for the transfer of dissolved species between the two phases; this mass transfer was used to control the pair potential between colloids in the droplets. For example, Leunissen et al. produced body-centered-cubic (BCC) crystalline assemblies in low dielectric constant systems ($5 < \varepsilon < 11$) confined in emulsion droplets[31]. The presence of the oil-water interface caused ions to partition into the continuous water phase, which increased the particle screening length in the droplet phase. This increase in the Debye length induced colloidal crystallization[32]. Due to the contribution of hydrogen bonding and its small ionic radii, H^+ ions were preferentially extracted into the aqueous phase. In this case, the BCC assembly was found within the oil phase ~ 50 μm or more from the oil-water interface. A dense monolayer of particles was formed at the oil-water interface and a large depletion zone with no particles (50-100 μm thick) existed between the interface and the BCC crystal. The dense particle monolayer was bound to the interface due to a particle attraction to an opposite image charge that appear in the aqueous phase near the interface. Aside from the particle monolayer, the depletion zone was induced by Coulombic repulsion of the positively charged particles to the like-charged aqueous phase. The aqueous phase adapted a positive charge based on the unequal partitioning of the H^+ ions.

In addition to crystalline structures, colloidal suspension confined in a spherical droplet has been shown to form amorphous liquids with glassy dynamics. These dynamics stemmed from the effects of crowding and of reduced mobility at the interface controlled by the external fluid viscosities; the particle drag coefficient was a function of the distance from the interface and both the internal and external fluid viscosities[33]. Therefore, external fluids with higher viscosities showed reduction in particle mobility within the droplets.

To date, all droplet-based assemblies produced have been either crystalline or dense amorphous glasses. However, the colloidal gel phase is an important class of colloidal matter. The defining features of colloidal gels are the slow dynamics generated by colloidal bonding due to attractive interactions. These gels form sample-spanning networks, which lead to particle localization on short length scales and solid-like elastic rheology on long length scales.

Here, we exploit the oil-water interface at the droplet boundary and the droplet confinement to induce colloidal crystallization and gelation in the oil phase of microfluidically produced droplets of nanoliter volume. The droplets are produced by a capillary-based microfluidic co-flow device; they are oil-in-water droplets with sterically stabilized PMMA colloids, which are initially uniformly dispersed. Under these conditions, both colloidal crystals and gels are formed within a single emulsion droplet system, with a time-dependent transition between the two phases observed. The self-assembled structures are imaged at the single-particle level and their three-dimensional, network structures quantified. Lastly, the effects of droplet size on gelation kinetics are

studied and further extend the droplet-based assembly method to ellipsoidal particles to obtain complex structures.

4.3 Methods

Poly(12-hydroxy-stearic acid) (PHSA) stabilized poly(methyl methacrylate) (PMMA) particles with average diameter of 1.4 μm (5.6% polydispersity, σ/D_{avg}, where σ is the standard deviation of particle diameter and D_{avg} is the average particle diameter)[34] and 1.0 μm (5.6% polydispersity) were used. The function of the PHSA was to sterically stabilize the particles so that they do not aggregate. PMMA colloids were dispersed in a refractive index and density matched solvent of 66 vol.% bromocyclohexane (CHB) and 34 vol.% decahydronaphthalene (decalin). The concentration of the partially dissociating salt, tetrabutylammonium bromide (TBAB), within the solvent was varied from 0 μM to 1 mM. The varying electrolyte concentrations resulted in a Debye layer thickness of the colloids from 95 nm to 1.2 μm. This colloidal system was selected for the following reasons: the colloid/solvent refractive index matching minimized the van der Waals interactions, as well as allowed visualization of the colloids by confocal microscopy. Density matching minimized sedimentation of colloids in the droplets. The initial colloidal volume fraction within the dispersion was 0.05.

For some gelation studies, 1.0 μm (5.6% polydispersity) particles were partially destabilized prior to use. PMMA colloids were destabilized through vigorous mixing in a 1:100 v/v dilution of 0.02 wt.% sodium methoxide in 4:1 v/v hexane/isopropyl alcohol for 1 hour. Sodium methoxide partially degraded the covalently grafted PHSA stabilizers.

Ellipsoidal particles were produced by a procedure developed by Keville et al. and Ho et al. and adapted by Mohraz et al. and Zhang et al.[35–38] The method involved casting PMMA particles into a cross-linked PDMS film. PDMS (average M_w = 110,000 g/mol) was used with methylhydro-dimethyl siloxane copolymer as the cross-linking agent and stannous 2-ethylhexanoate as the catalyst. Films were pre-cured for 24 hours in a Teflon mold and post-cured in the oven at 70°C for 3 hours. After curing, films were cut into strips of uniform dimensions (1 cm x 3 cm) and clamped onto a uniaxial, in-oven stretching apparatus, developed in our laboratory. Then, the oven was heated to 150°C, above the glass transition temperature of PMMA (T_g = 120°C), and held at the temperature for at least 15 minutes. The films were stretched uniaxially to achieve the ellipsoidal shape and desired aspect ratio. After the stretching step, the films were cooled and cut from the stretching apparatus. The synthesized ellipsoids were recovered from the films by chemically degrading the PDMS matrix of the film in a reagent mixture of sodium methoxide in isopropyl alcohol (IPA) and hexane (0.96 wt.% sodium methoxide, 20.63 wt.% IPA, 61.95 wt.% hexane, 2.74 wt.% film) and magnetically stirred at 500 rpm for 2 days. The chemical degradation of the matrix using sodium methoxide, however, caused the degradation of the PHSA stabilizers on the particle surface. Therefore, following the degradation process, a restabilization step was added to reconstitute the PHSA stabilizers to the surface of the particles. The restabilization process involved dispersing the ellipsoidal particles in a mixture of 6.15 wt.% particles, 81.52 wt.% hexane, 0.06 wt.% 2-2'-azo-bis-isobutyronitrile, 0.03 wt.% nile red, and 12.23 wt.% PHSA. The mixture was magnetically stirred and heated at 70°C for 3 days. The SEM

images of the ellipsoids used are shown in Figure 4-1b; the aspect ratio of the ellipsoids was 3.52 ± 0.18 (major axis = 2.77 ± 0.05 μm, minor axis = 0.79 ± 0.05 μm).

200 μm oil-in-water droplets containing the five volume percent colloidal suspension were formed using a coflow microfluidic device[39]. The device contained two coaxially aligned capillaries. The inner capillary tube was cylindrical and had an outer diameter of 0.87 mm with a tapered tip of d_{tip} = 50 μm. The tapered tip was manufactured by first using a micropipette puller (Sutter Instruments, PC-84) to generate micropipettes with thin tapered ends. Then, the tip was cut at a specific, desired diameter using a microforge (Olympus, TPI Model MF-1). The outer square capillary had an inner diameter of 1 mm and was coated with a hydrophilic, 1:5 (w/w) solution of Rain-X Antifog and isopropyl alcohol. As shown in Figure 4-2c, the oil solution containing the particle dispersion flowed through the inner capillary forming the droplets at the tip. An aqueous solution of 10 wt.% polyvinyl alcohol (PVA) was used as the continuous phase flowing through the square capillary. PVA served as the stabilizer for the droplets by forming a surfactant layer at the oil and water interface and preventing droplet coalescence. Droplets were stable for ~ 1 month. The flow rates of the particle dispersion and aqueous phases were held at 0.02 ml/hr and 70 ml/hr, respectively. Under these conditions, monodisperse droplets of size ~ 200 μm were produced at ~ 5 drops/s and collected in a vial for further experiments. In one case, the droplet sizes were varied between 150 μm to 350 μm to study the effect of the droplet size in the self-assembly behavior.

The kinetics of the assembly process were tracked by confocal laser scanning microscope (Nikon A1R). Cross-sections of the droplets at height 10 μm were imaged at increasing times to track the assembly behavior over time. Using a 100X objective (NA = 1.40), 488 nm and 561 nm lasers were used to image the droplet interface and the dispersed fluorescent colloids using the reflection and fluorescence channels, respectively.

For structural characterization, three-dimensional stacks of images (512 x 512 pixels) with spatial resolution of 83 nm/pixel to yield volumes of 42 x 42 x 6 μm^3 were obtained at a height of 2 μm within the droplet from the point in contact with the cover slip. To determine the three-dimensional structure of the assemblies, centroidal coordinates of the particles in the assemblies were determined by image analysis[40].

4.4 Results & Discussion

A suspension of 1.4 μm PHSA-stabilized PMMA colloids confined in oil-in-water droplets of size ~ 175 μm forms a crystalline structure after about 4 days (Figure 4-3). The confocal microscopes images are taken at a height 10 μm above the bottom of the droplet; they show a cross-section of the droplet at that height. At this condition, the colloid is an amorphous liquid for one day (Figure 4-3a,b). On day 2, ordered structures form at the droplet interface (Figure 4-3c). Ordering progresses into the central region of the droplet cross section by day 3 (Figure 4-3d). Colloidal crystallization is complete by day 4 and persists at longer times (Figure 4-3e,f). From the number of colloids confined in the droplets (~ 100,000), the final crystalline structure of the assembly is predicted to be face-centered cubic[42]. The crystals observed show a ring-like pattern with periodic

spacing between each ring. These rings are an interesting consequence of the crystal layers stacking within the curved interface of the droplet.

Differences in the observed structures from the literature originate from the method by which the assemblies are formed. Nijs et al. produced colloidal face centered cubic (FCC) crystals through evaporation of the solvent in the suspended emulsion droplets containing the colloids[42]. The evaporation process increased the packing fraction of the colloids in the droplets, eventually leading to the formation of a FCC crystal. In contrast, crystals formed in this work display large particle-particle spacing (Figure 4-3e), with separations that are ~ 1 μm greater than the particle diameter. Based on the initial salt concentration of initial colloidal dispersion, the Debye length of the particles is estimated to be ~ 90 nm. This distance is much smaller than the separation between the surfaces of colloids in the crystal. The difference suggests that there is an increase in the Debye length of the colloids over time. Indeed, based on the separation between the colloids, we estimate that Debye length in the droplets at long times to be ~ 500 nm. As the Debye length increases, the phase transition boundary shifts to lower volume fractions, until crystallization occurs at the 5 volume percent concentration of colloids in the droplet.

Leunissen et al. [31,32] have reported a comparable crystallization mechanism. In their system, droplets were stabilized by PMMA colloids in the organic phase that had adsorbed as a monolayer at the oil-water interface. A large Debye screening length was observed in the oil phase, up to many particle diameters in dimensions. As previously discussed, a large Debye length was due to ion migration out of the oil phase and into the

aqueous phase. The colloidal system studied in the present work differs only in the presence of PVA as an interfacial stabilizer of the oil droplets.

We find that the time scale for crystallization (~ 4 days) is much larger than what is expected for diffusion of ions out of the droplets, as found by Leunissen et al. Based on the size of the droplets (~ 175 μm in diameter) and the diffusion constant of an ion of radius ~ 0.3 nm (3.3×10^{-10} m^2 s^{-1})[32], the ion diffusion time is no greater than about 10 s; consequently the Debye length between the colloids should increase rapidly; colloidal crystallization should therefore occur rapidly. The discrepancy could stem from the use in our work of a polymeric, surfactant PVA layer for droplet stabilization; the PVA may significantly retard the partition of ions across the interface[43]. Notwithstanding the different kinetics of the process, the crystallization observed is consistent with a time-dependent Debye length. This observation suggests the semi-permeability of the oil-water interface, an effect we now exploit to produce colloidal gels.

Figure 4-4 demonstrates that the crystallization process is complex with competing mechanisms for assembly and sensitive to the degree of clustering of the droplets. The crystallization structure shown here (Figure 4-4, day 10) is not as distinct as in Figure 4-3e,f and the characteristic time scales for crystallization is longer (~ 10 days). Variations in the structure and the time scale for its development are associated with the amount of interfacial area that the droplet presents to the aqueous phase and the overall reservoir volume of the continuous phase. In the sample studied in Figure 4-4, the cluster size is only about 80 droplets per ~ 7.5 ml PVA solution, compared to ~ 250 droplets produced per equivalent amount of PVA solution for the experiment in Figure 4-3. These systems (Figure 4-4) with increased interfacial area with the bulk phase results

in the introduction of a competing assembly behavior: gelation. Clustering of the particles is first observed after 14 days for smaller droplets (150 μm). This clustering develops into a colloidal gel by 16 days. A similar gelation behavior is observed in larger droplets at longer times (~ 16 days). This transition to the colloidal gel structure with increased particle-particle attraction disrupts the colloidal crystal (Figure 4-4, Day 10).

Why does colloidal crystallization occur under some conditions (e.g. Figure 4-3) and not others (e.g. Figure 4-4)? Further investigation is carried out by, first, accelerating the transition to gelation through an initial, partial degrafting of the colloidal surface stabilizers by a degradation treatment, as described in the methods[38]. These partially destabilized colloids – due to a degraded surface stabilizer – still form stable colloidal dispersions in bulk solution for over a month. However, under the same solvent conditions as in the bulk, these colloids assemble into a gel within droplets within only ~ 3 days (Figure 4-5). The droplet interface is also populated with multiple layers of colloids (Figure 4-5b, inset).

The degradation of the steric stabilization of the colloids results in a more rapid formation of gels and the intervening crystal phase is now absent. A confinement-induced mechanism for colloidal gel formation is hypothesized, in which boundary-induced retardation of particle displacements results in increased effective particle attractions. Evaluation of this hypothesis is reported in Figure 4-7.

The network structure of the colloidal gels formed in the droplets is shown in Figure 4-6 at multiple length scales. A low-resolution confocal microscope image (10X objective, NA= 0.3) shows porous cage-like structures spanning the entire droplet (Figure

4-6a). Figure 4-6b is a cross section of the droplet taken at 10 μm above the droplet base. An open, branched structure within the interior of the droplet is observed (Figure 4-6b). A high-resolution region of the gel is shown in Figure 4-6c. This single-particle level structure of the gel shows disordered assembly structures with interstitial voids. From the image volumes taken near the droplet base, image processing results indicate an apparent volume fraction of about 0.25 (~5 times the initial volume fraction). This suggests that there is a possibility for phase separation or sedimentation of the gel structure, resulting in areas of increased volume fractions coexisting with large voids. The radial distribution function (RDF) of the assembly structure plotted in Figure 4-6d displays a peak at ~ 1 particle diameter position (first coordination shell) and a smaller peak at ~ 2.5 particle diameter. At a low particle density, the RDF of a (dispersed) colloidal fluid would be characterized by a small peak at the 1-particle diameter position. The RDF would be nearly flat at large separations. Colloidal gels on the other hand display a much sharper peak at contact; the RDF can also display a power law dependence on separation consistent with fractal microstructure[44]. Additionally, the contact number distribution of the colloidal gel (Figure 4-6e) is calculated based on the first minimum in the g(r) and the mean contact number of the colloidal gels in Figure 4-6 is found to be 4.6 ± 1.3.

Increased gelation times are observed for larger droplet sizes (Figure 4-7). In this experiment, destabilized PMMA particles are encapsulated in droplets of sizes varying from 150 to 350 μm in diameter. Solvent conditions (1 μM TBAB in CHB/decalin) and particle loading (0.05 volume fraction) remain the same in all droplets. The blue line indicates the time of gelation, defined as the time at which complete arrested, network structures are observed. Figure 4-7 shows that the gelation time increases with the size of

the droplet, up to 250 μm. Similar gelation times (~ 3 days) are found for 250 and 350 μm droplets. The gelation time therefore is an increasing, near linear function of droplet diameter for droplet sizes up to 250 μm. Above that dimension, gelation time is independent of the droplet diameter.

One possible mechanism for gelation is confinement-induced attraction of particles. Confinement driven gelation has been found for depletion gel systems[7]. Spannuth et al. reported that confinement in a micro-wedge with thickness ranging from 8.7 to 116 particle diameters resulted in a fluid-gel transition at lower polymer concentrations in depletion gel systems. This effect of confinement persisted to dimensions ~ 35 particle diameter in thickness. For increased confinement, the strength of particle-particle attraction increased, as deduced by larger cluster size distributions and decreased particle displacement probability[7].

Consequently, one explanation of the linear decrease in gelation time as the droplet is made small is that these smaller droplets represent confined systems. Increased confinement, in this case, leads to faster gelation times due to decreased particle displacement within the small droplets (Figure 4-7), or alternatively, due to a lowering of the amount of interparticle attraction required to stabilize a gel. This dependence can be understood in the following way: gelation requires a percolating, sample-spanning structure. The cluster size distribution in an attractive colloidal system shifts toward smaller size clusters as the strength of pair attractions are decreased. If gelation is taken as the attractive strength that generates a system-spanning cluster, then if the system size is decreased the cluster size needed to span the sample will also decrease. Gelation can

then be achieved at lower attractive strengths. The Figure 4-7 data are consistent with this explanation, if the scale ~ 250 μm represents a crossover to bulk behavior, a length scale above which the aforementioned confinement mechanism would no longer dominate. Although this scenario explains the observed size dependence, it is not consistent the additional observation that these particles do not even gel in bulk. Therefore, behavior in the ~ 250 μm and ~ 350 μm droplets is already different than bulk behavior. We require some additional mechanism to explain the qualitative difference between behavior in any droplet and in bulk.

The method to produce colloidal gels in droplets can be extended to anisotropic colloids. For example, we apply the colloidal destabilization principal to create gels of colloidal ellipsoids (Figure 4-8). A dispersion of ellipsoidal colloids is encapsulated within the oil-in-water droplets, with good dispersion of the particles observed on day 1 (Figure 4-8a). By day 3, droplets are either devoid of particles within the 10 μm cross-section (Figure 4-8b), or, have aggregation/adsorption at the droplet interface and large aggregate clusters that span partially into the center of the droplet (Figure 4-8c). Due to the ellipsoidal particle synthesis process – which involves the degradation of the PDMS matrix in sodium methoxide solution – the ellipsoidal particles have less stability, even compared to the deliberately destabilized spherical particles used earlier in this work. These destabilized ellipsoids aggregate more readily onto the droplet interface and into large clusters, rather than space-spanning structures.

4.5 Conclusion

In this work, we induced the assembly of colloidal gels within oil-in-water droplets. We discovered that a phase transition from colloidal crystals to gels takes place within droplets as time progresses. As previously observed by Leunissen et al., for crystalline assemblies, self-assembly in the droplets was driven by the partitioning of ions out of the droplet oil phase, across the semi-permeable interface, and into the aqueous phase. This mass transfer depleted the oil phase of ions, increased the solution Debye length, and increased the range of the pair repulsion between colloids. After the initial crystallization, a transition to a colloidal gel was found as the droplet interfacial area accessible to the outer aqueous phase increased (by decreasing the droplet cluster size). Thus, even though the Debye length of the gels was increasing with time, an attraction was also being generated; at long time this attraction apparently dominated and gelation occurred rather than crystallization. The gelation kinetics was found to depend upon the droplet size and the degree of droplet contact with the aqueous phase. Ellipsoidal particles in droplet confinement similarly formed aggregated structures at the droplet interface.

4.6 Figures

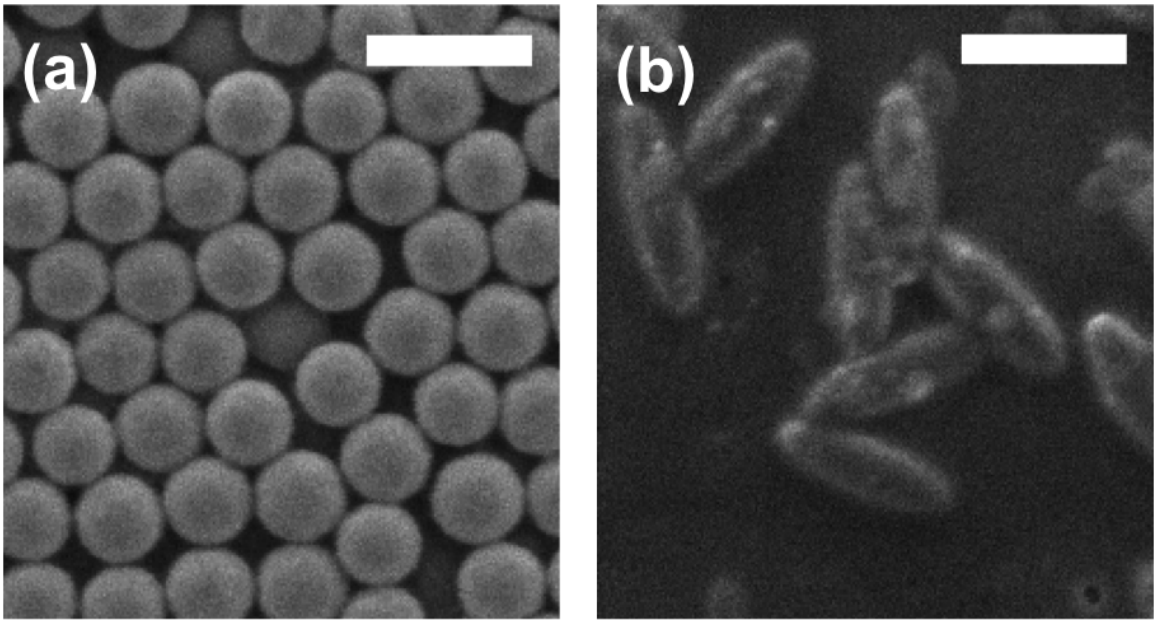

Figure 4-1. SEM images of colloidal spheres and ellipsoids.

(a) Spherical colloids with mean diameter of 1.4 μm (σ_{mean} = 0.57%) are shown. (b) Ellipsoidal colloids with 3.52 ± 0.18 aspect ratio (major axis = 2.77 ± 0.05 μm, minor axis = 0.79 ± 0.05 μm) are shown.

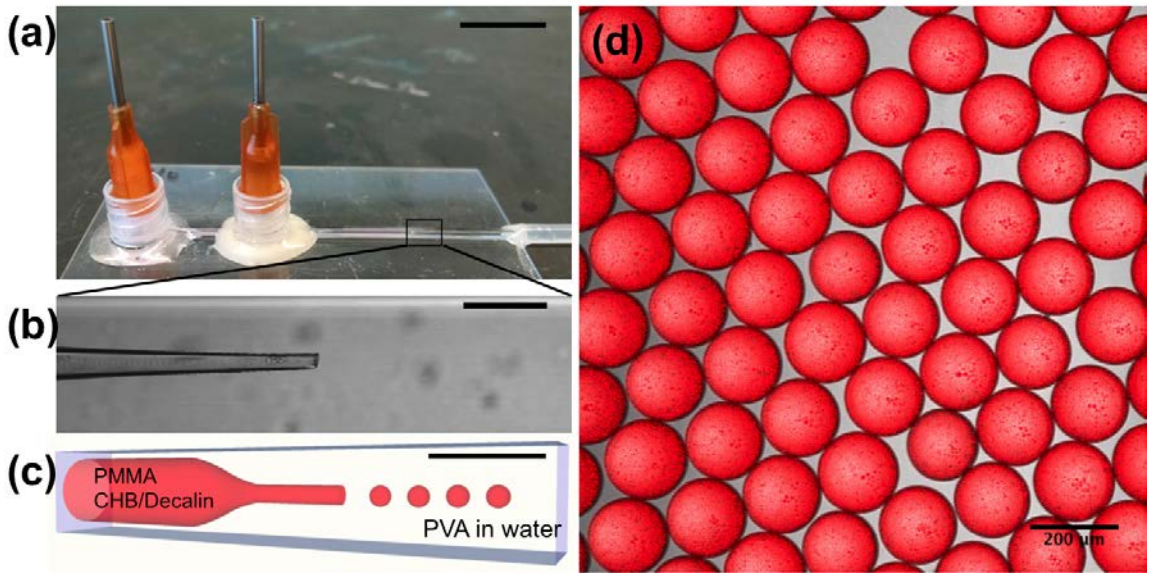

Figure 4-2. Microfluidic device and monodisperse oil-in-water droplets.

(a) Image of the 3D microfluidic device for the production of oil-in-water emulsion droplets. Scale bar is 1.5 cm. (b) Zoomed-in confocal microscope image of the inner capillary tip (~ 50 μm). The inner capillary is aligned coaxially within the outer square capillary. Scale bar is 200 μm. (c) Schematic of the microfluidic device and the production of oil-in-water droplets. The flow of the inner flow through the cylindrical capillary is a poly(methyl methacrylate) colloidal suspension at 0.05 volume fraction in 66:34 volume percent cyclohexyl bromide and decahydronaphthalene. The outer flow through the square capillary is 10 wt.% polyvinyl alcohol in water. Scale bar is 200 μm. (d) Confocal microscope image of monodisperse oil-in-water droplets produced by the microfluidic device. Average droplet diameter, in this case, is 175 ± 5 μm. Scale bar is 200 μm.

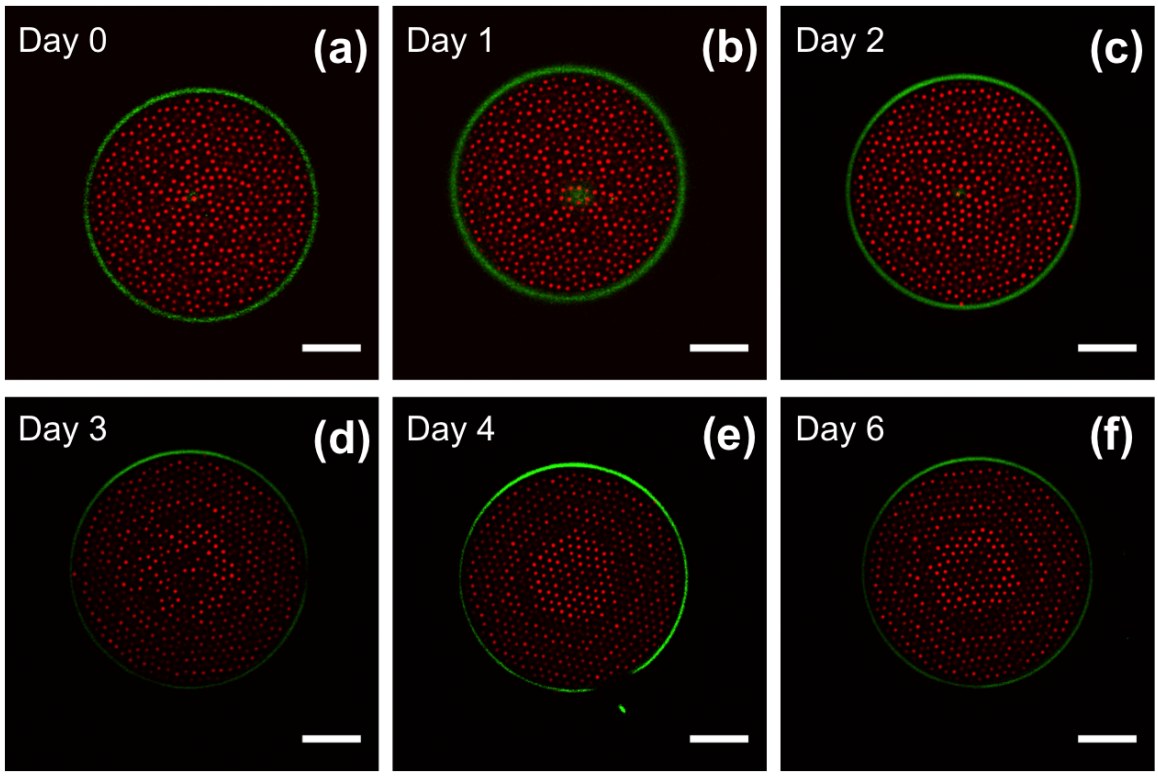

Figure 4-3. Time-lapse confocal microscope images of colloidal crystallization in oil-in-water droplets.

The inner phase is a colloidal suspension of 1.4 μm diameter PMMA colloid prepared at ϕ_0 = 0.05 in CHB/decalin with 1 mM TBAB added. The droplet size is ~ 175 μm. The reflection channel (in green) is used to image the droplet interface. Images of the droplet are taken at 10 μm above the coverslip and the bottom of the droplet. Scale bars are 20 μm. (a-b) The microstructure of the colloidal suspension in the droplet does not show much change in the first 0-1 days. (c) Positional order of colloids is observed near the interfacial boundary of the oil-in-water droplet after three days. (d) Ordering of the colloids is apparent from the concentric rings of colloids, which reflect registry of different layers that are stacked within the droplet. (e-f) In about 4 days, complete crystallization of colloids in the droplet is reached. Ordered ring-like patterns are shown; the separation of colloids at this condition is large (~ 1 μm) relative to the particle size of 1.4 μm.

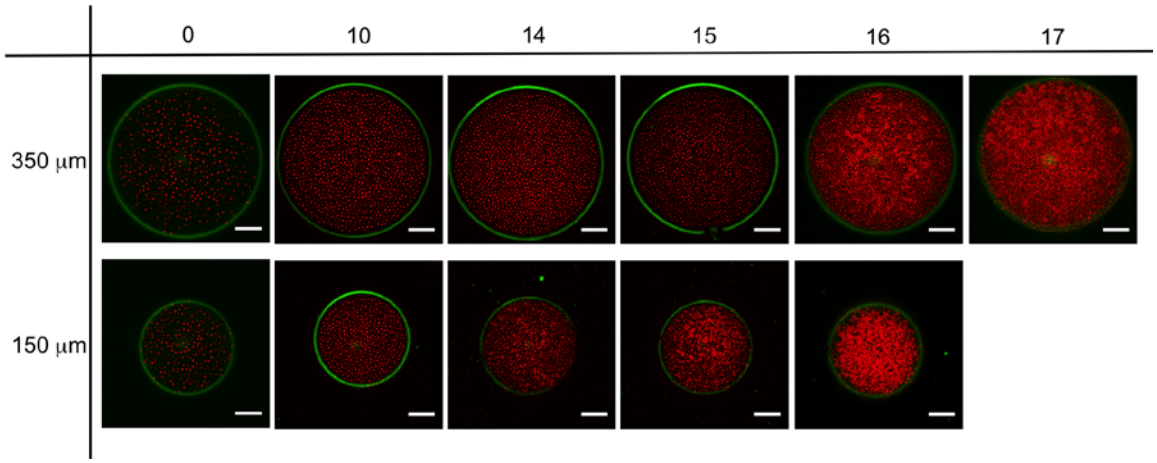

Figure 4-4. Droplet size dependent transition from colloidal crystallization to gelation within oil-in-water droplets.

The inner phase is as in Figure 4-3. The droplet size is ~ 150 and 350 μm. Imaging conditions are as in Figure 3. Scale bars are 20 μm. Columns and rows indicate the time at which the droplet was imaged in units of days and droplet diameters, respectively. Crystallization, such as was observed in Figure 3, transitions to gelation over longer times (over 10 days). The initiation of gelation occurs faster for smaller droplets (150 μm droplets gel in ~ 14 days), than the larger droplets (350 μm droplets gel ~16 days).

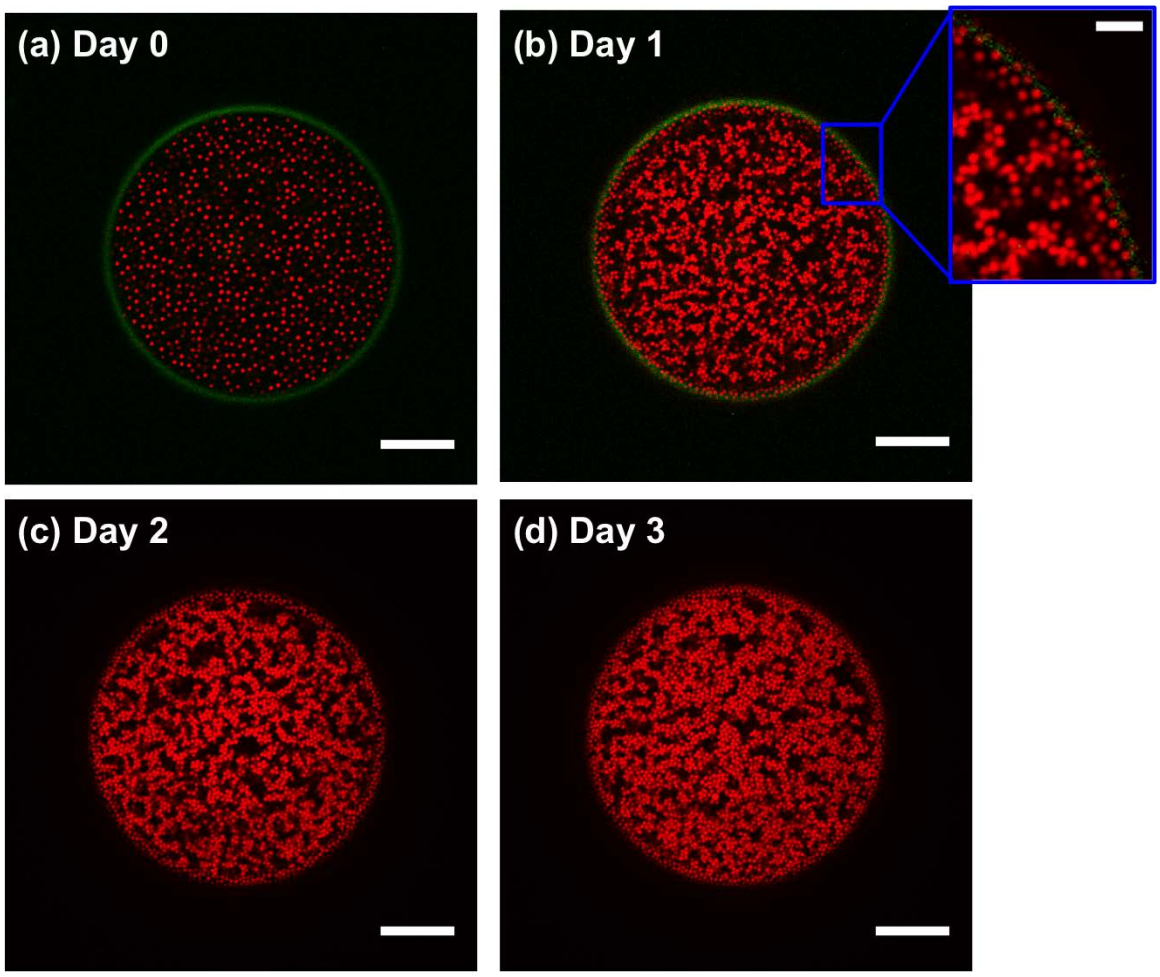

Figure 4-5. Kinetics of PMMA colloidal gelation in oil-in-water droplets.

The inner phase is 1.0 μm colloid suspension prepared at ϕ_0 = 0.05 in CHB/decalin with 1 μM TBAB and 0.01 g/ml of PHSA. The droplet size is ~ 200 μm. Imaging conditions are as in Figure 4-3. Scale bars are 20 μm. (a) Image shows a colloidal dispersion with no apparent aggregates. (b) By day 1, large clusters of colloids are formed. A colloidal monolayer adsorbed at the droplet interface is also apparent. (c) Further aggregation of the clusters is observed by day 2, forming a colloidal gel-like assembly. (d) A fully arrested, space-spanning colloidal gel is formed by day 3.

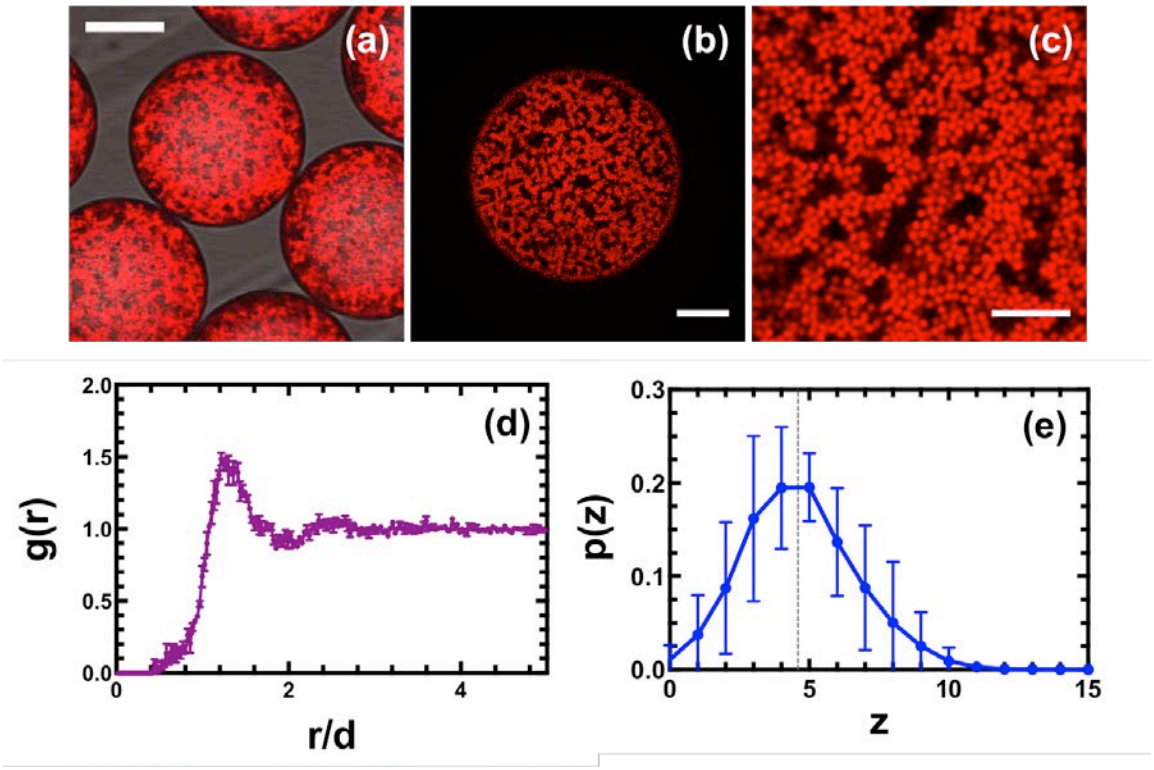

Figure 4-6. Colloidal gel structure in droplets at multiple scales.

The inner phase is 1.0 μm colloid suspension prepared at ϕ_0 = 0.05 in CHB/decalin with 1 μM TBAB and 0.01 g/ml of PHSA. (a) Confocal microscope image at 10x (with zoom 3) shows colloidal gel structure, spanning the entire droplet. Scale bar is 100 μm. (b) Confocal image at intermediate scales shows the droplet spanning gel network. Image is a slice of the colloidal droplet at 10 μm above the cover slip. Scale bar is 20 μm. (c) High resolution image at 100x shows detail of the colloidal gel microstructure. (d) Radial distribution function, g(r), of colloidal gels in droplets. (e) The contact number distribution of colloidal gels in droplets[§§]. g(r) and contact number distribution are calculated and averaged for image volumes acquired in three different droplets. Error bars indicate standard error of the mean.

[§§] The data in Figure 4-6(d-e) was contributed by Megan Szakasits.

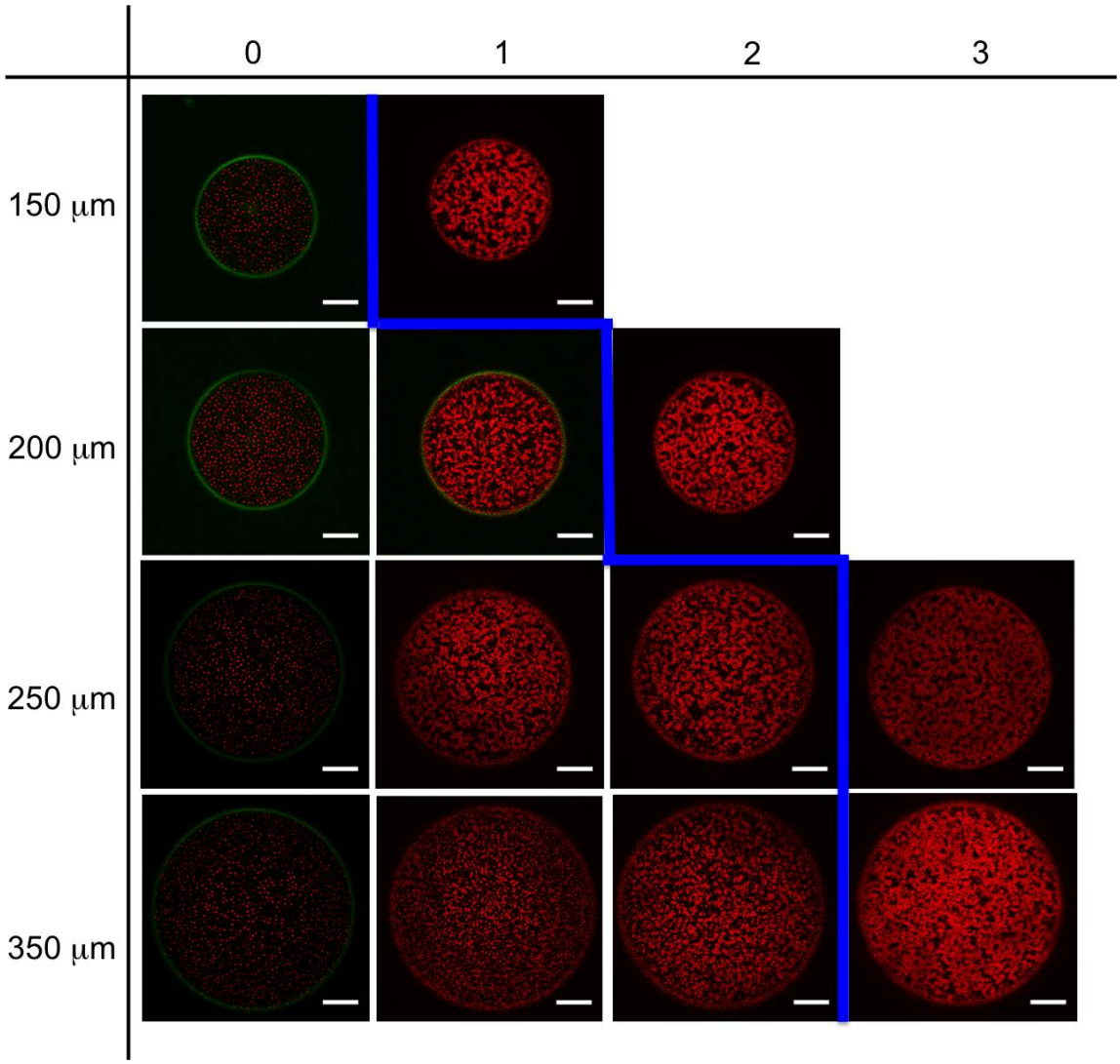

Figure 4-7. Colloidal gelation time dependence on droplet sizes.

The inner phase is 1.0 μm colloid suspension prepared at ϕ_0 = 0.05 in CHB/decalin with 1 μM TBAB and 0.01 g/ml of PHSA. Imaging conditions are as in Figure 3 and 4. Scale bars are 20 μm. Droplets to the right of the line are gels. Gelation time is taken as the point at which a complete arrested state is obtained. Columns denote the time of image (in units of days). Rows show different droplet sizes, ranging from 150 to 350 μm. Gelation time is shown to increase with droplet diameter until 250 μm. The gelation time for both 250 and 350 μm droplets is the same.

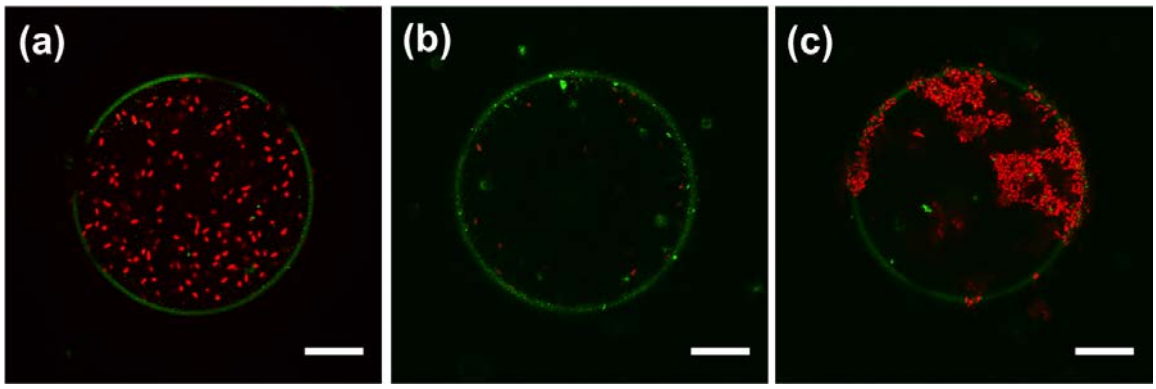

Figure 4-8. Ellipsoidal colloid assembly in oil-in-water droplets. .

The inner phase is ellipsoidal particle suspension prepared in CHB/decalin with 1 μM TBAB and 0.01 g/ml PHSA. The droplet size is ~ 200 μm. Imaging conditions are as in Figure 3. Scale bars are 20 μm. (a) Ellipsoidal particle suspension in droplets at day 1 shows a well-dispersed solution. (b-c) By day 3, droplets show two distinct final structures. (b) Droplet is void of the ellipsoids at the imaging place 10 μm above the bottom of the droplet. (c) Droplet shows aggregation of ellipsoids at the droplet interface. Large clusters of ellipsoids are also observed extending from the interfacial aggregates.

4.7 References

1. Velev, O. D. & Gupta, S. Materials Fabricated by Micro- and Nanoparticle Assembly - The Challenging Path from Science to Engineering. *Adv. Mater.* **21,** 1897–1905 (2009).

2. Anderson, V. J. & Lekkerkerker, H. N. W. Insights into phase transition kinetics from colloid science. *Nature* **416,** 811–5 (2002).

3. Zaccarelli, E. Colloidal gels: equilibrium and non-equilibrium routes. *J. Phys. Condens. Matter* **19,** 323101 (2007).

4. Grzelczak, M., Vermant, J., Furst, E. M. & Liz-Marzán, L. M. Directed self-assembly of nanoparticles. *ACS Nano* **4,** 3591–605 (2010).

5. Brugarolas, T., Tu, F. & Lee, D. Directed assembly of particles using microfluidic droplets and bubbles. *Soft Matter* **9,** 9046 (2013).

6. Wang, W. *et al.* Controllable microfluidic production of multicomponent multiple emulsions. *Lab Chip* **11,** 1587–92 (2011).

7. Spannuth, M. & Conrad, J. C. Confinement-Induced Solidification of Colloid-Polymer Depletion Mixtures. *Phys. Rev. Lett.* **109,** 028301 (2012).

8. Liu, B., Besseling, T. H., van Blaaderen, A. & Imhof, A. Confinement Induced Plastic Crystal-to-Crystal Transitions in Rodlike Particles with Long-Ranged Repulsion. *Phys. Rev. Lett.* **115,** 078301 (2015).

9. Riley, E. K. & Liddell, C. M. Confinement-controlled self assembly of colloids with simultaneous isotropic and anisotropic cross-section. *Langmuir* **26,** 11648–56 (2010).

10. Gong, T. & Marr, D. W. M. Electrically Switchable Colloidal Ordering in Confined Geometries. *Langmuir* **17,** 2301–2304 (2001).

11. Lin, T., Rubinstein, S. M., Korchev, A. & Weitz, D. A. Pattern formation of charged particles in an electric field. *Langmuir* **30,** 12119–23 (2014).

12. Dommersnes, P. *et al.* Active structuring of colloidal armour on liquid drops. *Nat. Commun.* **4,** 2066 (2013).

13. Avendaño, C., Liddell Watson, C. M. & Escobedo, F. A. Directed self-assembly of spherical caps via confinement. *Soft Matter* **9,** 9153 (2013).

14. Theberge, A. B. *et al.* Microdroplets in microfluidics: an evolving platform for discoveries in chemistry and biology. *Angew. Chem. Int. Ed. Engl.* **49,** 5846–68 (2010).

15. Sen, D. *et al.* Probing evaporation induced assembly across a drying colloidal droplet using in situ small-angle X-ray scattering at the synchrotron source. *Soft Matter* **10,** 1621–7 (2014).

16. De Nijs, B. *et al.* Entropy-driven formation of large icosahedral colloidal clusters by spherical confinement. *Nat. Mater.* **14,** 56–60 (2015).

17. Kim, S.-H., Park, J.-G., Choi, T. M., Manoharan, V. N. & Weitz, D. A. Osmotic-pressure-controlled concentration of colloidal particles in thin-shelled capsules. *Nat. Commun.* **5,** 3068 (2014).

18. Shirk, K., Steiner, C., Kim, J. W., Marquez, M. & Martinez, C. J. Assembly of colloidal silica crystals inside double emulsion drops. *Langmuir* **29,** 11849–57 (2013).

19. Kim, S.-H. *et al.* Optofluidic Assembly of Colloidal Photonic Crystals with Controlled Sizes, Shapes, and Structures. *Adv. Mater.* **20,** 1649–1655 (2008).

20. Kim, S.-H., Lee, S. Y., Yi, G.-R., Pine, D. J. & Yang, S.-M. Microwave-assisted self-organization of colloidal particles in confining aqueous droplets. *J. Am. Chem. Soc.* **128,** 10897–904 (2006).

21. Shah, R. K. *et al.* Designer emulsions using microfluidics. *Mater. Today* **11,** 18–27 (2008).

22. Utada, A. S. *et al.* Dripping, Jetting, Drops, and Wetting: The Magic of Microfluidics. *MRS Bull.* **32,** 702–708 (2011).

23. Shih, W.-H. *et al.* Mechanical Properties of Colloidal Gels. *MRS Proc.* **155,** 83 (2011).

24. Hsiao, L. C., Newman, R. S., Glotzer, S. C. & Solomon, M. J. Role of isostaticity and load-bearing microstructure in the elasticity of yielded colloidal gels. *Proc. Natl. Acad. Sci. U. S. A.* **109,** 16029–34 (2012).

25. Velev, O. D. & Gupta, S. Materials Fabricated by Micro- and Nanoparticle Assembly **—** The Challenging Path from Science to Engineering. *Adv. Mater.* **21,** 1897–1905

26. Filip, D., Uricanu, V. I., Duits, M. H. G., Agterof, W. G. M. & Mellema, J. Influence of bulk elasticity and interfacial tension on the deformation of gelled water-in-oil emulsion droplets: an AFM study. *Langmuir* **21,** 115–26 (2005).

27. Gillies, G. & Prestidge, C. A. Interaction forces, deformation and nano-rheology of emulsion droplets as determined by colloid probe AFM. *Adv. Colloid Interface Sci.* **108-109,** 197–205 (2004).

28. Gado, E. Del, Fierro, A., Arcangelis, L. de & Coniglio, A. Slow dynamics in gelation phenomena: From chemical gels to colloidal glasses. *Phys. Rev. E* **69,** 051103 (2004).

29. Solomon, M. J. & Spicer, P. T. Microstructural regimes of colloidal rod suspensions, gels, and glasses. *Soft Matter* **6,** 1391 (2010).

30. Yi, G.-R. *et al.* Colloidal Clusters of Silica or Polymer Microspheres. *Adv. Mater.* **16,** 1204–1208 (2004).

31. Leunissen, M. E., van Blaaderen, A., Hollingsworth, A. D., Sullivan, M. T. & Chaikin, P. M. Electrostatics at the oil-water interface, stability, and order in emulsions and colloids. *Proc. Natl. Acad. Sci. U. S. A.* **104,** 2585–90 (2007).

32. Leunissen, M. E., Zwanikken, J., van Roij, R., Chaikin, P. M. & van Blaaderen, A. Ion partitioning at the oil-water interface as a source of tunable electrostatic effects in emulsions with colloids. *Phys. Chem. Chem. Phys.* **9,** 6405–14 (2007).

33. Hunter, G. L., Edmond, K. V. & Weeks, E. R. Boundary Mobility Controls Glassiness in Confined Colloidal Liquids. *Phys. Rev. Lett.* **112,** 218302 (2014).

34. Xu, S. *et al.* Generation of Monodisperse Particles by Using Microfluidics: Control over Size, Shape, and Composition. *Angew. Chemie* **117,** 734–738 (2005).

35. Keville, K. M., Caruthers, J. M. & Franses, E. I. Characterization of dimensions of ellipsoidal microparticles via electron microscopy. *J. Microsc.* **142,** 327–340 (1986).

36. Ho, C. C., Keller, A., Odell, J. A. & Ottewill, R. H. Preparation of monodisperse ellipsoidal polystyrene particles. *Colloid Polym. Sci.* **271,** 469–479 (1993).

37. Mohraz, A. & Solomon, M. J. Direct visualization of colloidal rod assembly by confocal microscopy. *Langmuir* **21,** 5298–306 (2005).

38. Zhang, Z., Pfleiderer, P., Schofield, A. B., Clasen, C. & Vermant, J. Synthesis and directed self-assembly of patterned anisometric polymeric particles. *J. Am. Chem. Soc.* **133,** 392–5 (2011).

39. Utada, A. S., Fernandez-Nieves, A., Stone, H. A. & Weitz, D. A. Dripping to Jetting Transitions in Coflowing Liquid Streams. *Phys. Rev. Lett.* **99,** 094502 (2007).

40. Crocker, J. C. & Grier, D. G. Methods of Digital Video Microscopy for Colloidal Studies. *J. Colloid Interface Sci.* **179,** 298–310 (1996).

41. Sader, J. E., Chon, J. W. M. & Mulvaney, P. Calibration of rectangular atomic force microscope cantilevers. *Rev. Sci. Instrum.* **70,** 3967 (1999).

42. De Nijs, B. *et al.* Entropy-driven formation of large icosahedral colloidal clusters by spherical confinement. *Nat. Mater.* **14,** 56–60 (2015).

43. Dinsmore, A. D. *et al.* Colloidosomes: selectively permeable capsules composed of colloidal particles. *Science* **298,** 1006–9 (2002).

44. Ohtsuka, T., Royall, C. P. & Tanaka, H. Local structure and dynamics in colloidal fluids and gels. *EPL (Europhysics Lett.* **84,** 46002 (2008).

45. Mason, T. G., Bibette, J. & Weitz, D. A. Elasticity of Compressed Emulsions. *Phys. Rev. Lett.* **75,** 2051–2054 (1995).

Chapter 5 Conclusions and Future work

The overall motivation for this dissertation was to investigate the self-assembly of two different kinds of soft matter – colloids and surfactants – away from bulk equilibrium conditions. We used light, flow, and confinement to induce fast and reversible assemblies of colloidal crystals, to study the behavior of surfactant assemblies under large deformations, and to develop a novel method to produce colloidal gels confined in a single emulsion droplet, respectively.

In Chapter 2, we introduced a simple, directed assembly method that yields 3D colloidal crystals that are simultaneously reconfigurable in space and time. The observed crystals were produced on fast time scales ($t < 60$ s) and in spatially selective regions (scales as small as ~ 10 μm). Our method used commonly available sterically stabilized, charged latex colloids dispersed in low dielectric constant solvents that are nearly refractive index matched with the particles. By illuminating a glass substrate coated with a uniform (unpatterned) layer of indium tin oxide (ITO), we observed convection, accumulation, and assembly of colloids at the illuminated region. The 3D colloidal crystals generated by the optical field were about 5 layers thick, extending 10 microns into the bulk.

Experiments indicated that the mechanism is general to cases of charged colloids in low dielectric constant solvents in contact with metallic or semiconducting substrates. In

these cases, substrate-based chemical reactions induced an ion flow that establishes an electric field, which drives photoinduced electrophoretic motion of the colloids. Simple optical manipulations therefore allowed assembly and depletion regions produced by the light to be switched in time and space, so as to create colloidal crystal arrays whose shape can be easily controlled. For this reason, the method represented a new kind of template-free, reconfigurable photolithography of 3D colloidal crystals. In the future, this work could be extended to generate large-scale assemblies (on the order of a few millimeters) for applications in light-induced color-changing materials. For larger scale materials, the power of the light source needs to be correspondingly increased to achieve similar power densities as reported in Chapter 2.

In Chapter 3, we reported spatiotemporal dynamics of gradient shear bands of wormlike micelle solutions in rectangular channel flow. The velocity profiles within the channel and the transient dynamics of the flow in the near-wall region were observed by means of confocal microscopy and particle image velocimetry. Above the critical wall shear rate conditions, steady-state profiles deviated from a parabolic shape to an introduction of a thin, near-wall region with high velocity and high shear rates. The linear increase in apparent slip velocities in this region with applied wall shear rates suggested that the high shear rate bands are narrow (< 250 nm) and are not observable with the current experimental method.

Within the near-wall region, velocity fluctuations along the vorticity axis of the flow were observed at distances up to 10 μm from the wall in the gradient direction. Space-time plots of the flow in the flow-vorticity plane at 2 μm gradient position from the wall showed four distinct stages of transient dynamics. First, the flow accelerated

simultaneously at all points along the vorticity axis to about one-half of the final, steady-state velocity in the near-wall band. Second, a global deceleration of the flow along the entire vorticity axis slowed down the flow to about one-half the magnitude of the previously accelerated velocity. Third, multiple bands of variable velocities were formed along the vorticity direction. The widths of these bands were found to depend on the shear rate condition studied. Finally, the bands grew and merged over time to form a single, homogeneous flow with a fast, steady velocity at the 2 μm position from the wall.

We furthermore discussed the connection between the transient vorticity fluctuations observed in this work and recent experimental and theoretical studies of wormlike micelles in plane Poiseuille flows. Based on the comparison, we concluded that the transient dynamics reported here could be an interfacial instability that is driven by the difference in the second normal stress difference at the interface of the gradient shear bands. To further probe this hypothesis, several different experiments could be carried out in the future. First, tests at higher shear rate conditions (closer to the high shear rate region) could be performed by manufacturing a new channel flow device using a rectangular microcapillary (100 μm x 1 mm x 50 mm). Under these conditions, a flow rate of ~ 60 ml/hr could produce wall shear rates of ~ 10^4 s^{-1}, our estimate of the high shear rate branch. Additionally, an increase in the observation window along the vorticity axis could reveal fully developed interfacial undulations. To increase the observed image plane, larger probe particles (~ 1 μm) could be used in conjunction with a 10X objective. Permanent periodic fluctuations would be apparent along the vorticity direction on the space-time plot, if the interfacial instability is, indeed, a steady-state phenomenon.

In Chapter 4, we generated colloidal gels by confining PMMA colloidal dispersions in oil-in-water droplets. Under confinement, we observed a phase transition from colloidal crystals to gels over time (~ 2 weeks). The formation of crystalline phases stemmed from the extraction of dissolved ions within the dispersed solvent, which increased the Debye screening length of the particles. We hypothesized that the gelation transition occurs through confined boundary effects, which would reduce particle displacement probabilities. The gelation kinetics were found to depend upon the cluster sizes of the droplets (inhibiting droplet interfacial accessibility to the outer phase), droplet sizes, and the stability of the dispersed particles. We further applied the confined assembly method to ellipsoidal particles and found that they aggregated at the interface and formed large clusters that partially extended into the center of the droplet.

Expanding upon this work, the mechanical properties of the droplets could be measured using atomic force microscopy (AFM). Preliminary experiments were carried out to measure the elastic moduli of the droplets by AFM. Droplet deformability was measured by atomic force microscope (Asylum Research, MFP-3D) using a triangular silicon nitride level (TR400-PSA) as shown in Figure 5-1. The spring constant, calibrated using the Sader method[1], was 28.06 pN/nm. Droplets were loaded with a force of 30 nN. The Hertz model fit was used, assuming a spherical tip of 20 nm radius (the nominal radius of the tip). All fits resulted in R^2 values above 0.95. At small loading forces (about 2-3 nN), the elastic response, in large part, was contributed by the elasticity of the fluid-fluid interface of the stabilized droplets[2]. Therefore, large loading force was used to access the elasticity of the bulk solution within the droplets.

For 200 μm droplets with 5% initial particle loading, elastic modulus of 4.3 ± 0.5 kPa was reported based on 10 independent droplet measurements. In the future, this work could be extended by carrying out a more detailed investigation of the internal assembly contributions to the mechanical integrity of the droplets. Increased colloidal volume fractions[3] or smaller particle sizes[4] within the droplets could lead to formations of colloidal gels with larger elasticity. Also, the droplet elastic modulus is proportional to D^{-2}, where D is the droplet diameter[5]. Therefore, we could increase the droplet size to better probe the elastic effects from the colloidal gels.

5.1 Figures

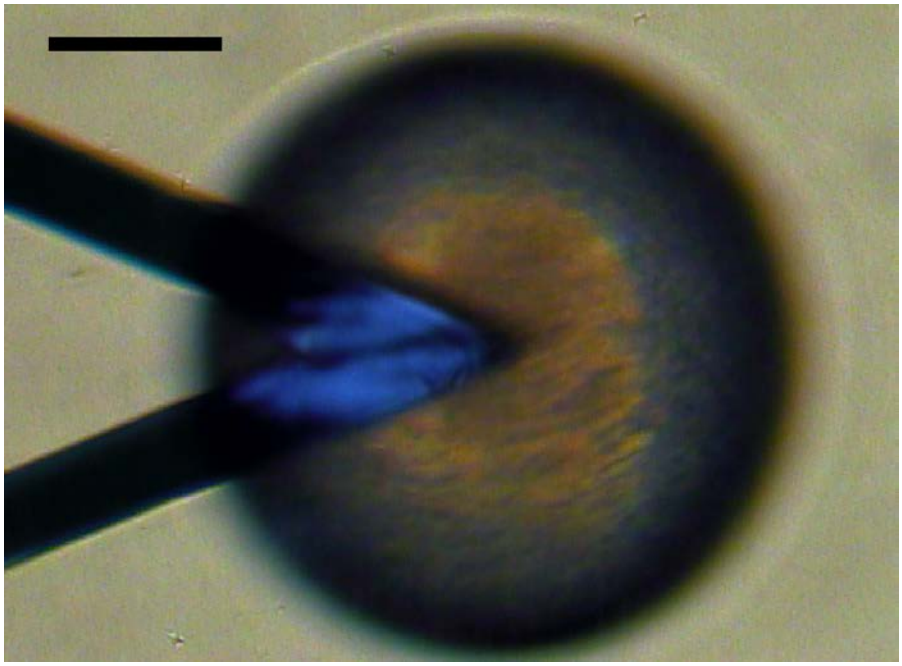

Figure 5-1. Droplet elastic modulus experiment using AFM[⌗].

Image of the AFM cantilever tip centered at the droplet surface. Scale bar is 50 μm.

[⌗] The experimental data appearing in this section was performed by Aaron Tan.

5.2 References

1. Sader, J. E., Chon, J. W. M. & Mulvaney, P. Calibration of rectangular atomic force microscope cantilevers. *Rev. Sci. Instrum.* **70,** 3967 (1999).

2. Filip, D., Uricanu, V. I., Duits, M. H. G., Agterof, W. G. M. & Mellema, J. Influence of bulk elasticity and interfacial tension on the deformation of gelled water-in-oil emulsion droplets: an AFM study. *Langmuir* **21,** 115–26 (2005).

3. Krall, A. H. & Weitz, D. A. Internal Dynamics and Elasticity of Fractal Colloidal Gels. *Phys. Rev. Lett.* **80,** 778–781 (1998).

4. Shih, W. Y., Shih, W.-H. & Aksay, I. A. Elastic and Yield Behavior of Strongly Flocculated Colloids. *J. Am. Ceram. Soc.* **82,** 616–624 (2004).

5. Malkin, A. Y., Masalova, I., Slatter, P. & Wilson, K. Effect of droplet size on the rheological properties of highly-concentrated w/o emulsions. *Rheol. Acta* **43,** 584–591 (2004).

Appendices

Appendix A. Salt curves for both SLE3S/SLS and SLE1S systems

The effect of added salt on the zero-shear viscosity is measured for the two anionic surfactant WLM systems investigated in this study. It is known that, self-assembled microstructures transition from entangled to branched networks with increasing salt concentration. This transition is identified by the maximum in zero shear viscosity as a function of the salt concentration; branching is associated with salt concentrations above the zero shear viscosity maximum. Based on the salt curves, shown below, the 3.5 wt.% NaCl solution of SLE3S/SLS and the 3.15 wt.% NaCl solution of SLE1S systems are at the top of their respective salt curves. The 1.9 wt.% NaCl solution of the SLE3S/SLS system resides to the left of the zero shear viscosity maximum; this condition is associated with a linear entangled WLM system.

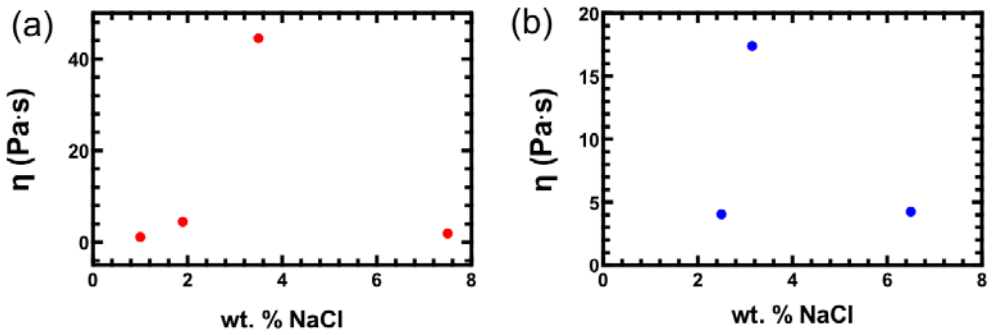

Figure A-1. Salt curves for (a) SLE3S/SLS and (b) SLE1S WLM systems. Salt curves for both SLE3S/SLS system and SLE1S system indicate that the two solutions (3.5 wt.% and 3.15 wt.% NaCl) used in experiments lie at the top of the salt curve. In one case, 1.9 wt.% SLE3S/SLS system is used, which lies to the left of the salt curve peak.

Appendix B. Measured flow rates and transient velocity measurements

As discussed in the main text, the flow apparatus has a slow time constant of about 500 s under low shear rate conditions (below 2.2 s^{-1}) due to the high viscosity of the fluid in this shear rate region. This sluggish response is shown in the transient velocity measurements in Figure 3.5a. In comparison, at high rates of 20.1 s^{-1}, the viscosity of the fluid is an order of magnitude smaller and the time constant of the flow is faster (~ 20 s).

For the case of the low shear rate conditions, the slow time constant can be traced back to the flow apparatus (Figure B-1a). The steady-state development times of the transient velocity measurements coincide with the slow rise times of the flow rate. Therefore, we conclude that the slow time constants of the flow at low shear rates are caused by the time it takes for the flow to fully develop rather than a transient flow behavior at the near-wall region.

At high shear rate conditions, we compare the flow rate measurements to the transient velocity profiles to verify that the transient behavior of the flow is independent of the time constant of the flow. Figure B-1b demonstrates that the abrupt acceleration in the transient velocity measurements occur at ~ 100 s from flow start-up. The flow rate time constant in this case is about 20 s. Therefore, the discrepancy between the two time scales clearly suggests that the transient phenomenon observed is not an effect of the flow apparatus.

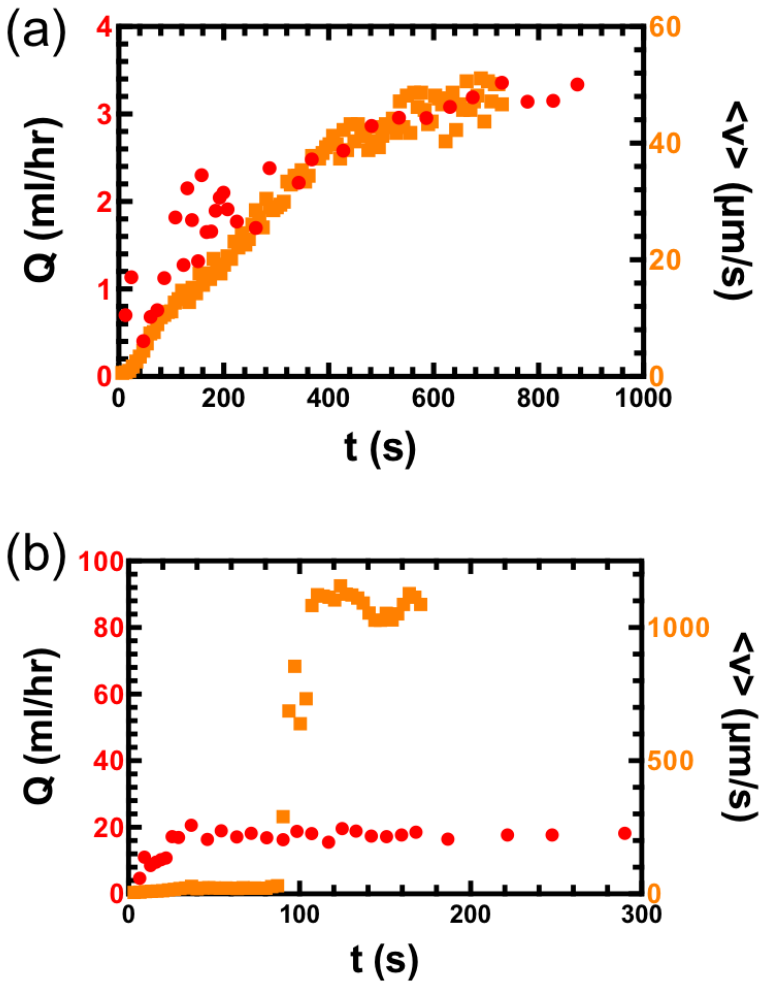

Figure B-1. Comparison of flow rates and average velocity measurements over time. (a) Flow rates and average velocities are plotted as a function of time for the 2.2 s^{-1} flow condition. The two curves overlap and show a characteristic time scale of about 500 s. (b) Flow rate and average velocity measurement are plotted for 11.7 s^{-1} condition over time. The characteristic time constant for the flow rate measurement is about 20 s. The time at which the abrupt acceleration is observed in the velocity measurements is about 100 s. The velocity measurements are taken at 2 μm from the wall.

Appendix C. Particle Image Velocimetry (PIV) Validation

Results of the PIV method are validated by comparing the PIV velocity measurements to the results from the particle tracking method. Particle tracking method identifies and tracks individual particles in a pair of frames to quantify the velocity field. In contrast, the PIV method calculates the velocity distributions from the cross-correlation of multiple small regions of the image pair to obtain the displacement of a group of particles. For comparison, particle velocities are extracted along a line (0.63 mm, in the y direction) at 6 time points (1.1, 1.7, 2.2, 2.8, 3.4, 3.9 minutes) from the PIV data and the velocities are calculated by particle tracking along the same line.

Figure C-1 a-f show the comparisons taken at the time points specified. For the most part, the profiles obtained from both measurements agree well with the largest discrepancies noted in Figures C-1 c,e, where the sharp, thin bands captured by the particle tracking method are not as well identified by the PIV method. This discrepancy is a consequence of the spatial resolution limit of the PIV method (~ 25 μm). Bands smaller than this resolution are not resolved by the PIV analysis. From this comparison, the mean deviations between PIV and particle tracking are found to range from 0.4% to 16% at the highest case. The highest deviation is reported for Figure SI 2e. Across all cases, the mean deviation is 3%.

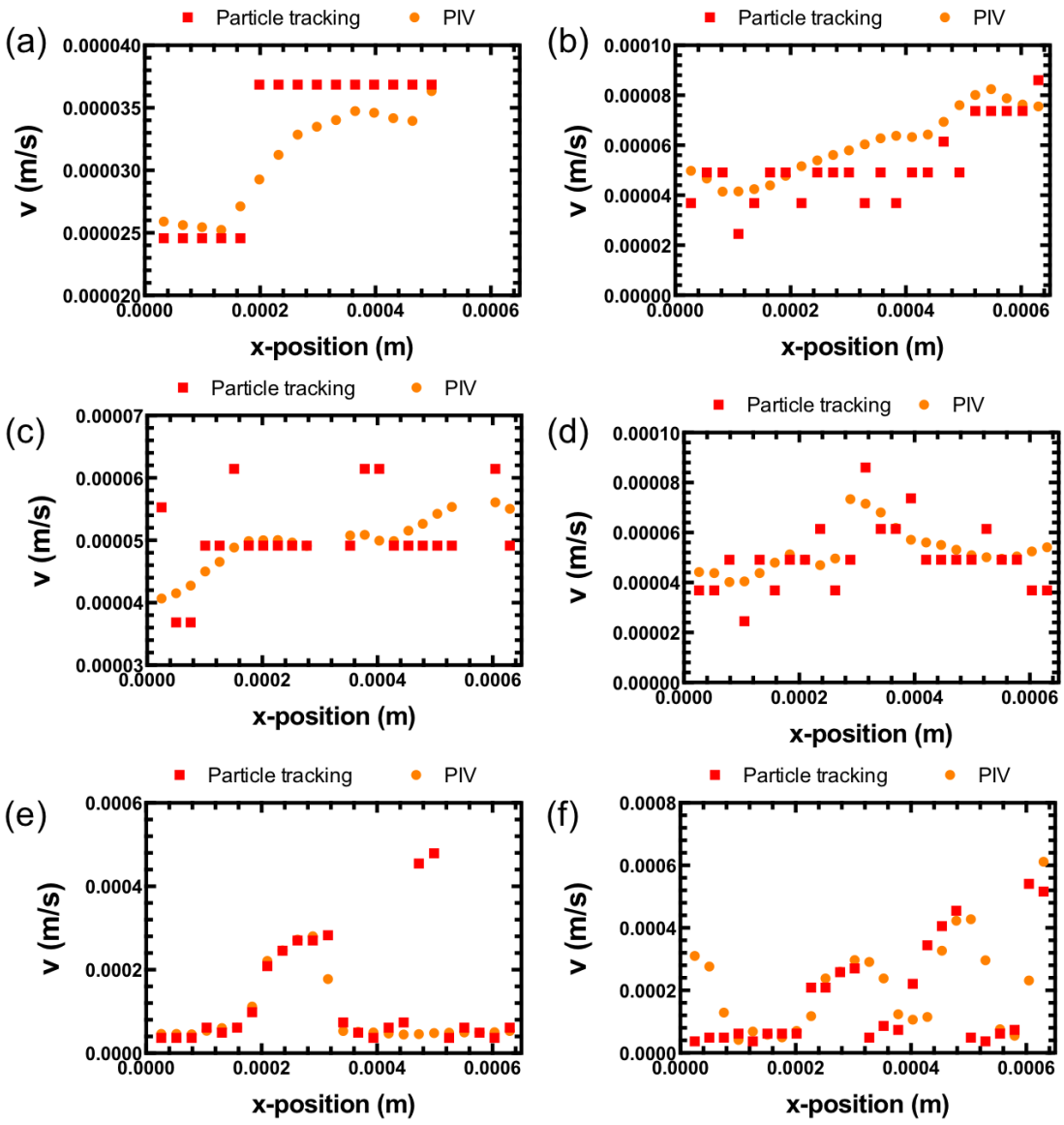

Figure C-1. Validation of the PIV method. The velocity measurements taken from particle tracking are compared to those of the PIV method. Time points for the flows, where the velocity measurements are taken: (a) 1.1 minutes, (b) 1.7 minutes, (c) 2.2 minutes, (d) 2.8 minutes, (e) 3.4 minutes, and (f) 3.8 minutes.

Appendix D. Near-wall velocity measurements for glycerol control

The flow profile of a Newtonian fluid (glycerol) is measured within 4 μm from the wall in 1 μm increments. The plot establishes that the linear velocity profile approaches zero at the wall. Data from this experiment (Figure D-1) shows good agreement between the measured particle velocities and the theoretical velocity expected under the specific flow condition (11.7 s^{-1}).

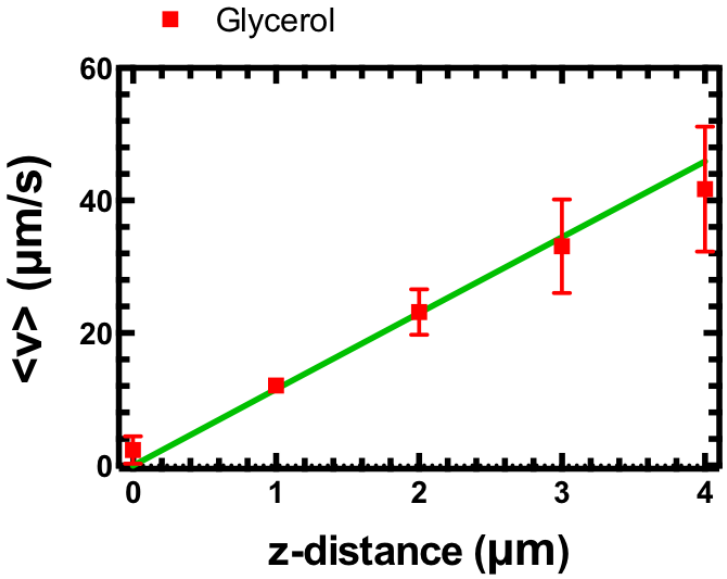

Figure D-1. Near-wall steady-state velocities measured for glycerol control. Glycerol control measurements are reported at 11.7 s^{-1}. The results show good agreement between measurement and theory, as shown by the agreement of the data with the green solid line, which is the expectation for a Newtonian flow of glycerol's viscosity.

Appendix E. Spatiotemporal behavior of other WLM fluids

Similar spatiotemporal behavior is observed for two other WLM systems studied: SLE3S/SLS with 1.9 wt.% NaCl and SLE1S with 3.15 wt.% NaCl. The four-step process described in the main text is also displayed for above shear banding conditions for these fluids (Figure E-1). Wall shear rates of 24 and 14 s^{-1} are used, respectively. However, the deceleration phenomenon is short, and not as apparent in the 1.9 wt.% NaCl system in Figure E-1a. This is consistent with the observations in the original system at certain shear rate conditions (Figure 3.8c,e).

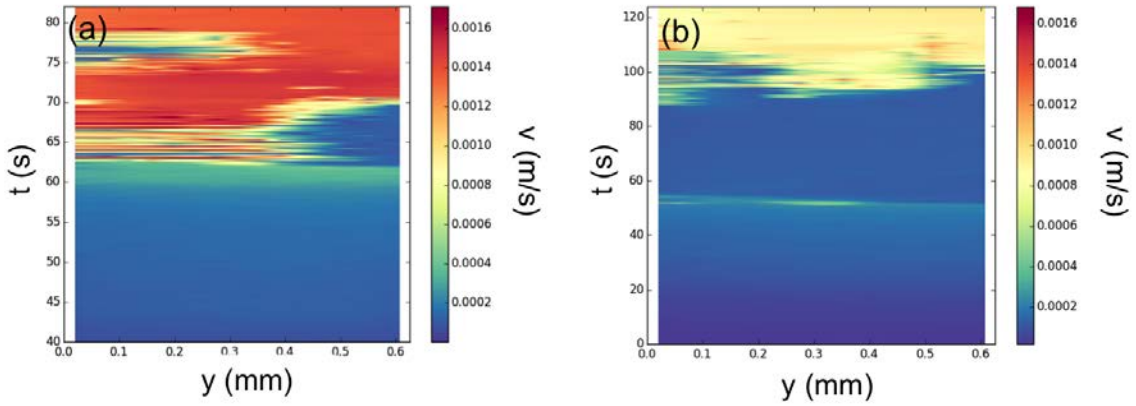

Figure E-1. Space-time plots of other WLM fluids. Similar spatiotemporal behavior is observed for the following: (a) the same WLM system with different salt concentration (1.9 wt. % salt), (b) a different anionic surfactant solution (SLE1S).